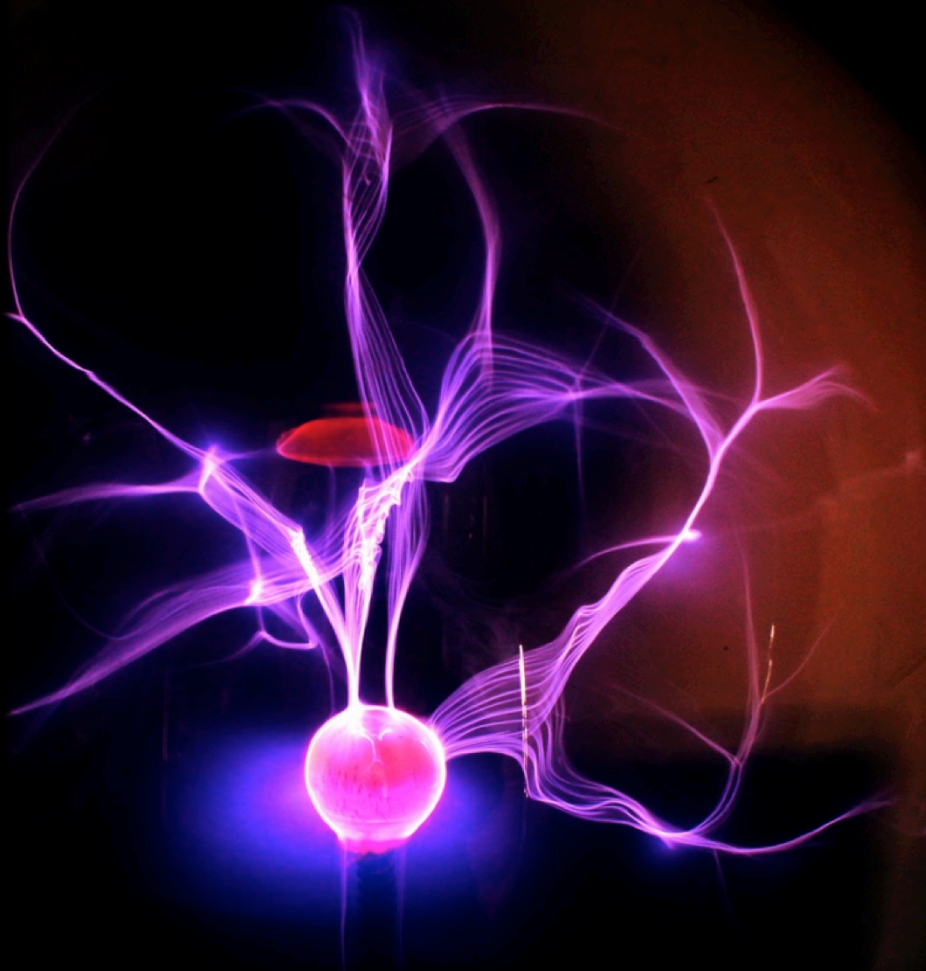


Non-thermal electron populations
in microwave heated plasmas
investigated
with X-ray detectors

Jaydeep Sanjay Belapure





TECHNISCHE UNIVERSITÄT MÜNCHEN
Max-Planck-Institut für Plasma Physik

Non-thermal electron populations in microwave heated plasmas investigated with X-ray detectors

Jaydeep Sanjay Belapure

Vollständiger Abdruck der von der Fakultät für Physik der Technischen Universität München zur Erlangung des akademischen Grades eines

Doktors der Naturwissenschaften (Dr. rer. nat.)

genehmigten Dissertation.

Vorsitzender : Univ.-Prof. Dr. rer. nat. B. Garbrecht
Prüfer der Dissertation 1. : Univ.-Prof. Dr. U. Stroth
2. : Univ.-Prof. Dr. sc. nat. P. Fierlinger

Die Dissertation wurde am 28.03.2013 bei der Technischen Universität München eingereicht und durch die Fakultät für Physik am 15.04.2013 angenommen.

... to my parents

Acknowledgements

Carrying out a research project like this is never possible by a single person alone. People not only from within the project boundary but also from the other side of the fence have contributed to it and I would like to express my gratitude towards all of them, named/unnamed. Before starting a PhD project, one could only *wish for* a nice supervisor to work with, I feel fortunate enough to have, for sure, more than one. I would fall a short of words to express my deepest gratitude to Mara and Bernhard, who I consider my real *gurus*, and to whom I owe so much. I would like to thank Bernhard for those endless brainstorming discussions we had over the several walks around the institute. The numerous tact and tricks I could learn while working with him. The project would not have taken its current shape without his infinite patience and enthusiastic support in all stages of the work. I would like to thank Mara for her most friendly guidance and constant encouragement during the low and high tides along this journey. This project would not have been completed without her being tightly holding all the knots of the ship. I am deeply grateful to my guide Prof. G. Hasinger for his fortitude and optimistic fore-view, and in spite of the confined time allowing me enough space for the research. Special thanks are offered to my supervisors Prof. U. Stroth and Dr. A. Weller for their invaluable support and fruitful scientific discussions.

Experienced advice and help by our engineer Mr. A. Mayer has always been very critical in the experimental work. Along with Mr. A. Mayer I would like to thank Mr. A. Wolf, Mr. Sellmair for the technical support. I am particularly grateful to Dr. O. Maj and Dr. E. Poli for their collaborative support with the Fokker-Planck simulations. Assistance provided by Dr. M. Otte, Dr. D. Schlosser, and Mr. T. Stange during the WEGA campaign is greatly appreciated. I would like to acknowledge ASDEX Upgrade team for all the infrastructure and facilities at Max Planck Institute for Plasma Physics. All this research work is funded by Excellence Cluster Universe, Garching and Technical University of Munich (TUM), Garching. I would like to appreciate the efforts of the thousands of individuals behind the coding projects like \LaTeX and

GNU. A special thank to Google for revolutionizing the method of literature survey underlying any research.

Finally, your *mood* is decided by your *food*. Thanks to the IPP canteen and especially my cook friend Bal, for making delicious cuisines. Thanks to the unlimited coffee in my office with Viola and Sotiria (the owner of the Coffee machine!), which helped regulating the (blood) pressure. The numerous lunch/Tea time discussions with my friends Pintu, Shiva, Sandesh, Satej and Arati on almost any random topic has been a cheerful ingredient in the PhD life.

The online discussions with Bhalchandra whether on a documentary or a Python code or physics or a biological phenomenon, it is always exciting and proved to be pedagogical. How can I forget the thankless support and general guidance by my friend Pintu. I specially thank Mayuresh and Priyanka for their support for keeping me on track especially in the later part of the thesis work. Throughout the PhD period, it is the tacit support by my friends Chinmayee, Mayuresh, Pintu which has kept boosting my morale. The stay in Munich would not have been so exciting without other activities and enthusiastic friends. Thanks to Priyanka, Jyaysi and Sneha for the imperishable joy amid the painting, running, cycling and swimming sessions, and Sandesh and Aarathi for the various photography experiments, and Satej and Arati for delightful food get-together. Also I would like to take this opportunity to thank my friends, who are not just the part of social life but have helped me in shaping my personal career at one or other stage, Abhay, Yugesh, Deepashri, Aditya, Arpan, Sumati, Maithili, Sonali, Harshad, Rohan, Sujit, Shveta and Vivek.

There have been always a significant influence of some of the personalities whom I adored. Prof. Jayant Narlikar whose lectures really inspired me, triggered my decision of taking up science as a career. The curious view towards all the phenomena by Prof. Richard Feynman has really tough how to explore physics without any boundaries. At last, some people in my life have so much importance that without them today I could not have been even acknowledging them; my college teacher Dr. Ms. Dabhade, my parents, my sister Deepali and her husband Sagar.

Abstract

The electron cyclotron resonance heating (ECRH) is one of the promising heating schemes for tokamaks at present and very important for future machines like ITER and Wendelstein 7X. The electron cyclotron current drive (ECCD) is extremely important in tokamaks due to its capability of replacing the induction based current drive in order to achieve steady-state operation. Recent experiments have also demonstrated the ability of simultaneously heating the plasma and driving plasma currents via the so called Fisch-Boozer mechanism, with an efficiency comparable to that of the lower hybrid (LH) current drive. The injection of strong ECRH and ECCD powers is accompanied by the generation of superthermal electron populations, which can have a prominent influence on the current profile shape as well as on plasma MHD processes. The role of the superthermal electrons in ECRH and ECCD physics is not yet being fully understood. In this thesis an investigation of the generation and dynamics of the superthermal electrons is carried out through the measurements of the hard X-ray emission. For this purpose, new (soft and hard) X-Ray pulse height analysis (PHA) diagnostics are constructed. The X-ray diagnostics are based on a current state of the art Silicon Drift type Detector (SDD) at the core. When operating the SDD alone, it is suitable for the soft X-ray energy range, whereas when coupled to a CsI(Tl) scintillator crystal the energy range is increased up to 500 keV. A detailed characterization of the soft and hard X-ray detector is carried out demonstrating both good spectral and timing properties. The suitability of the novel HXR detector in the fusion research is demonstrated for the first time. The interaction of the scintillator material (CsI(Tl)) with X-ray photons in the HXR detector is characterized by a cross-section that complicates the spectral analysis with the increase in photon energy due to only partial energy deposition. In such situations the analysis must incorporate the proper detector response function. The full Response Matrix of the unique HXR setup design and geometry is simulated using the GEANT4 package. In addition, the detector response function is validated through the extended laboratory calibration experiments. A Python based forward modeling

approach is developed by incorporating the detector response function. The complete SDD+CsI(Tl) based HXR diagnostic is recently installed and fully functional at ASDEX Upgrade. The generation and dynamics of the superthermal electrons is observed in many plasma scenarios spanning over a range of ECRH power and density. A bi-Maxwellian model is developed in order to characterize the energy distribution and the density of the superthermal electrons. In selected scenarios, the measurements are compared with the simulated electron distribution function obtained by the ray-tracing and Fokker-Planck code at ASDEX Upgrade. A close agreement between the measured and simulated superthermal tail is found in plasmas with ECRH power below 1 MW, indicating a strong influence of the parallel electric field (E_{\parallel}). During plasma scenarios with ECRH powers higher than 1 MW a clear increase of the tail temperature was observed for increasing ECRH heating powers. This effect could not be reproduced by the Fokker-Planck simulations in which, however, a realistic modeling of the power deposition could not be made as in the case of low ECRH power. The measurements of the superthermal population in diverse plasma parameters are therefore considered to deliver important information for further benchmark studies of Fokker-Planck simulations for ASDEX Upgrade plasmas aiming at clarifying the underlying physical processes.

List of Acronyms

ASDEX Upgrade	Axially Symmetric Divertor Experiment; a divertor tokamak operational since 1991 at the Max Planck Institute for Plasmaphysics, Garching (Germany).	IDA	Integrated Data Analysis; diagnostics data provision at ASDEX Upgrade
BaF₂	Barium fluoride; a scintillating material	ITER	“ <i>The way</i> ” in latin; a tokamak based machine planned to show the fusion ignition.
BGO	Bismuth germanate; a scintillating material	JFET	Junction gate field-effect transistor
CsI(Na)	Caesium iodide scintillator doped with sodium atoms	MCA	Multi-channel Analyzer
CsI(Tl)	Caesium iodide scintillator doped with thallium atoms	MHD	Magneto-hydrodynamics
ECCD	Electron Cyclotron Current Drive	NaI(Tl)	Sodium iodide scintillator doped with thallium atoms
ECRH	Electron Cyclotron Resonance Heating	NBI	Neutral Beam Injection
ECW	Electron cyclotron waves	PHA	Pulse Height Analysis
FWHM	Full Width Half Maximum	PIGE	Particle Induced Gamma Emission
HXR-PHA	Hard X-ray Pulse Height Analysis	PIXE	Particle Induced X-ray Emission
		PMT	Photo-multiplier Tube
		pn-diode	A semiconductor material doped a donor-impurity type on one side and acceptor-impurity type on the other side.
		PSD	Pulse Shape Discriminator
		RMF	Response Matrix Function
		SDD	Silicon Drift Detector
		SXR-PHA	Soft X-ray Pulse Height Analysis
		WEGA	A classical stellarator type machine at Greifswald
		XSPEC	X-ray spectral analysis package

LIST OF ACRONYMS

Contents

List of Acronyms	ix
1 Introduction	1
1.1 Need of fusion energy	1
1.2 Fusion versus fission research	2
1.2.1 Fusion in the stars versus in the laboratory	3
1.3 Fusion basics	4
1.3.1 Fusion device - Tokamak	6
1.4 Plasma heating basics	8
1.4.1 Consequence of induced voltage: runaway electrons	10
1.4.2 The electron cyclotron (EC) wave in plasma	11
1.4.2.1 Near the resonance	12
1.4.3 The wave-particle interaction	12
1.5 Numerical modelling of the electron distribution function	15
1.6 Bremsstrahlung emission	17
1.6.1 Thermal bremsstrahlung	19
1.6.2 Nonthermal bremsstrahlung	20
1.7 Motivations and the goals of the thesis	20
2 Instrumentation for the SX and HX diagnostics	23
2.1 Introduction	23
2.2 Interaction of the radiation with detector material	25
2.3 Working principle of the Silicon Drift type Detector (SDD)	28
2.3.1 Detector active volume	29
2.3.2 Reset preamplifier	31
2.3.3 Power supply	32

CONTENTS

2.3.4	Block diagram	32
2.3.5	Shaping amplifier	34
2.3.5.1	Pole-zero and baseline restoration	35
2.3.6	Gate	35
2.3.7	Multi-Channel Analyser (MCA)	35
2.3.8	Energy calibration	36
2.3.9	Energy resolution and noise	36
2.3.9.1	The inherent Poisson noise	37
2.3.9.2	Dependence on temperature	39
2.3.9.3	Dependence on the electronic noise	39
2.3.9.4	Total resolution	39
2.3.10	Efficiency of the SDD	40
2.4	Working principle of SDD with Scintillator CsI(Tl)	40
2.4.1	The scintillator active volume	40
2.4.2	Coupling with the SDD	41
2.4.3	Physical properties of the scintillator	42
2.4.4	Light yield and temperature dependance	43
2.4.5	Energy calibration	43
2.4.6	Efficiency of the CsI(Tl)	44
3	Setting up the SX and HX diagnostics	47
3.1	Introduction	47
3.2	Setting up the experiments	48
3.2.1	Detector vessel	48
3.2.2	Viewing geometry : Pinholes & filters	52
3.2.3	Detector operating voltages	55
3.2.4	Shaper	55
3.2.5	Improved grounding scheme	56
3.3	Characterization of SXR-PHA	57
3.3.1	Efficiency	57
3.3.2	Energy calibration and resolution	59
3.3.2.1	Effect of radiation damage	61
3.3.3	Detector response function	62
3.4	Characterization of HXR-PHA	63
3.4.1	Setup for the HXR-PHA characterization	64

3.4.2	Energy calibration and resolution	64
3.4.2.1	Zero-point measurement	66
3.5	Data handling software	67
3.6	Experimental setups at different machines	69
3.6.1	Experimental setup at WEGA	69
3.6.2	Experimental setup at PIXE/PIGE	71
3.6.3	Experimental setup at ASDEX Upgrade	74
3.6.4	Future proposed Assembly	75
3.7	Forward modeling technique for HXR: Block diagram	78
3.7.1	Module EventList	78
3.7.2	Module genResp	79
3.7.3	Module genModel	79
3.7.4	Module fitRMF	82
4	Construction of the Detector Response Matrix	87
4.1	Introduction	87
4.2	Geant4 simulation package	88
4.2.1	Implementation	88
4.3	Efficiency	89
4.4	Detector response function	90
4.4.1	Test of eigenvalue ratio	91
4.5	Experiment at PIXE/PIGE	92
4.6	Test measurements for the response matrix	96
5	Measurements of superthermal electrons	101
5.1	Introduction	101
5.2	Initial validation experiments	101
5.2.1	Neutron signal	102
5.2.2	Count rate limit	104
5.2.3	Background measurements	106
5.3	Measurements of superthermal electrons	109
5.3.1	Plasma discharges at ASDEX Upgrade	110
5.4	Evolution of the non-thermal distribution function	112
5.5	Spectral modeling and fraction of superthermal electrons	114
5.5.1	Fokker-Planck code estimates	114

CONTENTS

5.5.2	Bi-Maxwellian model	116
5.5.3	Modeling non-thermal emission at low ECRH power	118
5.5.4	Modeling non-thermal emission at high ECRH power	120
5.5.5	Density and power dependence	123
5.6	Other important observations	125
5.6.1	Extreme hard X-ray emission and runaway electrons	125
5.6.2	The saw-tooth like oscillations in the hard X-rays	128
6	Summary and outlook	133
A	Multi-channel Analyser (MCA)	137
B	Graphical User Interface: Elist	141
C	Spectral analysis of selected shots	143
	References	147
	List of Figures	161
	List of Tables	169

“99 % of the universe is plasma and I’m 99% sure that we don’t understand it fully.”

- Author

1

Introduction

It was in 1939, when Hans Bethe first proposed the explanation for how stars shine. Ever since, man has dreamt of creating the same source of energy shining in the laboratory! It is already 70 years since the energy production in stars was revealed [1]. Stars, in their early stages, bind together hydrogen into helium, a process called *fusion*. The energy released in the fusion reaction powers the stars. Tremendous efforts in technological and conceptual advancements have been made for realizing the ambition of achieving fusion in the laboratory. It would be a big leap towards solving the problem of global energy crisis. It is the aim of the fusion research community to bring the clean energy source, which shines the stars, on Earth. Since the first efforts in 1957 [2] the fusion research is gaining enormous knowledge and understanding of the basic plasma physics and the fusion science.

1.1 Need of fusion energy

With the projected future global population, the gap between the estimated energy demand and extrapolated supply from the current resources is ever increasing. The energy demand is expected to increase by 76% of the current demand just by the year

1. INTRODUCTION

2030. It is also reported that, even today nearly two billion people have no access to electricity. To match the future energy needs as well as to extend the electricity to the population still disconnected, expansion beyond our traditional methods of power generation is needed. The world electricity is currently supported roughly by three categories: (1) coal 40%, oil 5%, natural gas 21%, (2) wind, solar, hydro and other 20% (3) nuclear power 13.5%. [3].

Category one, the fossil fuels, although contributing to most of the power needs, is bound to face the problem of limited reservoir, plus it constantly adds to the environmental contamination. Category two, the renewable, are highly dependent on the environmental conditions and hence face a problem of inconsistent power supply. Besides, there is also a very basic but major technological problem of energy storage and energy transport. Category three, the nuclear power, does show a potential of taking up major percentage of power needs but also creates a medium for political conflicts and social activists and major environmental hazards. Stating the current and projected future situation, the world is in critical need of alternative power sources. In spite of the many innovative power generation techniques (e.g., renewable energy sources) coming forth, currently no single method is a solution to the global energy problem. In fact it is extremely necessary to explore in detail every potential resource to find out a feasible solution. The fusion energy has a potential to provide a sustainable, clean and major part of the global energy needs in the second half of the century.

1.2 Fusion versus fission research

An iron (Fe) nucleus, somewhere in the middle on the atomic mass scale, is the lowest energy and most stable nucleus, and nuclei from the both sides (low and high atomic masses) would want to become like an iron nucleus. The heavier nuclei tend to break into fragments whose masses are nearer to the iron's mass, on the other hand the lighter nuclei tend to fuse together to finally form the iron nucleus. In both of these processes the excess energy (binding energy per nucleon) is released. It is this nuclear source of energy which forms the basis of a power plant.

Let us compare fusion with nuclear fission. In the process of fission, the release of nuclear binding energy goes into the kinetic energy of the two product nuclei. The kinetic energy is then deposited into the container material as a form of *heat*. Hence,

in fission, harvesting the nuclear binding energy boils down to handling the heat energy from the reactor container. However, since the neutrons induce further fission in an avalanche process, the challenge was to have a fine control on the nuclear chain reaction. Due to the concentrated efforts, the first commercial fission power plant was ready just within a decade or two after the introduction of the concept, that breaking of a heavy nucleus is possible.

Similar to the fission power, the electricity supply based on fusion power was initially believed to be available in a moderate time span. Due to the numerous challenges in the fusion research, in spite of six decades of research the first commercial fusion power is believed to come in to action not before 2050 [4]. To appreciate the difficulties in the fusion process, we will compare the naturally occurring conditions in the stars with that in the laboratory. Nonetheless, since the 1960s there is a substantial increase in the understanding of the plasma processes as well as the technological advancements.

1.2.1 Fusion in the stars versus in the laboratory

There are subtle differences in the physical conditions on the stars and the conditions achievable in the laboratory. Hydrogen is the most abundant element in the universe. A primordial massive hydrogen gas cloud contracts and collapses in its own gravitational potential. During the collapse, the gas becomes increasingly hotter and denser. At the same time the gravitational potential-well becomes deeper and deeper and confines the hot gas. When the temperature at the center of the gas cloud reaches a million degree Celsius, the kinetic energy of the hydrogen nuclei become sufficient to tunnel through the natural coulomb repulsion and can fuse together to form helium. This luminous source of energy is what we call, a *star*. It is important to note that the stellar central density is so large that the gravitational potential is strong enough to keep the hot gas confined for several millions of years.

On the contrary, in the laboratory it is extremely challenging to trap the individual charged particles within the plasma. We use strong magnetic fields to curl up the trajectories of the charged particles of very high energy. The process of confinement of the hot plasma by means of magnetic fields is similar to squeezing a blob of jelly within a number of stretched rubber bands. The jelly would always try to escape through every possible gap between the rubber bands. In a similar fashion the plasma

1. INTRODUCTION

particles and energy loss is a major concern for the stability of the plasma. The hotter and denser the plasma is, the more critical it is to keep the plasma confined.

To achieve the fusion reaction it is important to hold in the system a certain number of particles \tilde{n} with the energy (in terms of temperature) \tilde{T} for a sufficiently long time period τ_E . Increase in any of these parameters would increase the probability of achieving the fusion. The product of these three important quantities is called the *Plasma triple product*. The threshold above which the self-sustained plasma starts burning is called the *Lawson criterion* [5]. Above the *Lawson criterion*, the α -particles produced (see Section 1.3) in the fusion reaction further heat the plasma and balance the energy loss. The fusion process is then probable enough to generate more energy than the energy pumped into the system.

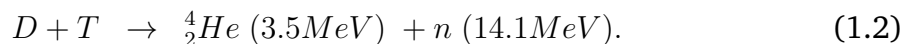
The critical value of the product is given by

$$\tilde{n}\tau_E\tilde{T} > 5 \times 10^{21} \text{ m}^{-3} \cdot \text{s} \cdot \text{keV}. \quad (1.1)$$

The fusion experiments around the world have steadily improved upon the achieved value of the plasma triple product but it still lies at least an order of magnitude below the threshold. The future fusion device (currently being under construction) called *ITER* (meaning in Latin *the way*) [4] is aimed to work close to this threshold value and give us maximum information about the way towards the first commercial Fusion-based power plant.

1.3 Fusion basics

Unlike in the stars, the optimal fusion reaction in the laboratory scale is not the hydrogen-hydrogen reaction because of its very low cross-section. In fact, among the many possible nuclear reactions [1] analyzed, the following is considered to be the most promising for Earth based experiments, in which two light nuclei *deuterium*(D) and *tritium*(T) fuse together to produce a *helium* (He) nucleus with the release of a *neutron* (n)



The kinetic energy of the reaction product is given in the parentheses. In a given thermal distribution of the particles, the distribution decreases exponentially with energy, whereas the cross-section increases as a function of energy. The product of

these two functions peaks only in a narrow energy range, the so called Gamow peak, gives the probability of the nuclei fusing together. Hence, it appears that the total fusion probability is extremely sensitive to the temperature. The D-T reaction gives the maximum cross-section among other reactions and is easily justified from the Figure 1.1 [6].

However, for the D-T reaction it requires one part tritium.

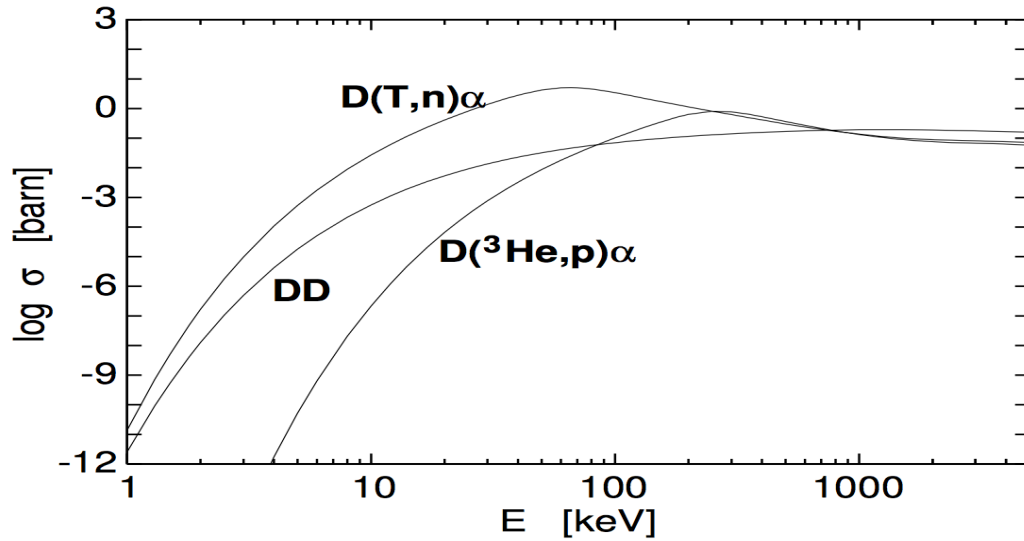
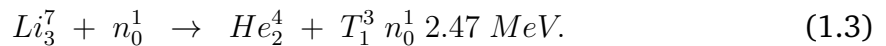


Figure 1.1: Fusion cross sections for three possible reactions. Note the resonance hump for D-T reaction around 100 keV makes the most promising reaction. [5]

Deuterium is abundant in Nature and can be easily obtained from ordinary sea water. Tritium on the other hand, due to its short radioactive half-life (12.3 years) is not readily present in Nature. One of the proposed methods to get tritium is through lithium, since lithium is one of the abundant elements. A D-T based fusion reactor would also produce a huge amount of neutron flux. A lithium based blanket type material surrounding the fusion vessel is expected to serve a dual purpose [7]. Firstly, to stop the neutrons and convert their kinetic energy into thermal energy to produce electricity. Secondly, the neutrons captured by the lithium would undergo fission to produce tritium necessary for the fusion reaction [5]



1. INTRODUCTION

At present to avoid that problem of the tritium most of the current tokamak conduct the D-D experiments



The basic fuel components, deuterium and lithium isotopes dissolved in the sea water can suffice global energy requirement for million years with the current power consumption rate. Hence, fusion has the potential to provide a practically inexhaustible source of clean energy. [6].

Based on the underlying method of fusing the nuclei together, the experimental devices are classified under the two major categories namely, magnetic confinement, and inertial confinement. The magnetic confinement efforts are again subdivided into three main types, *magnetic mirror experiments* [8], classic and modern *stellarator* devices [9; 10; 11] and the most investigated and promising *tokamak* devices.

1.3.1 Fusion device - Tokamak

A tokamak is is a magnetic confinement device to study fusion. As the word suggests (in Russian, *toroidal'naya kamera s magnitnymi katushkami*) it is a toroidal vacuum chamber with magnetic field [12]. The cartoon of a tokamak device is shown in the Figure 1.2.

The typical plasma temperature achieved in the current fusion reactors is of the order of 1-20 keV (i.e., over 100 million degree Celsius), i.e., a factor of 10 higher than the temperature of the core of the Sun. There is no material which can withstand such an extreme temperature. The only option is to suspend the plasma in the middle of the vacuum vessel. At such extreme temperatures any gas is expected to be in a highly ionized state (electrons and ions), called plasma. We know that the charged particles moving in a magnetic field tend to curl around (move along) the field lines like the beads woven on a thread. If the field is strong enough and in the form of a closed loop, it can trap charged particles of several keV energy. In order to contain the extremely hot plasma and to keep it detached from the vessel wall, a specific twisted torus-shape geometry of the magnetic field is implemented. See Figure 1.2. In the description of the tokamak geometry below, the directions are always referred in two terms, the *poloidal*, i.e., towards the pole, and the *toroidal*, i.e., along the torus.

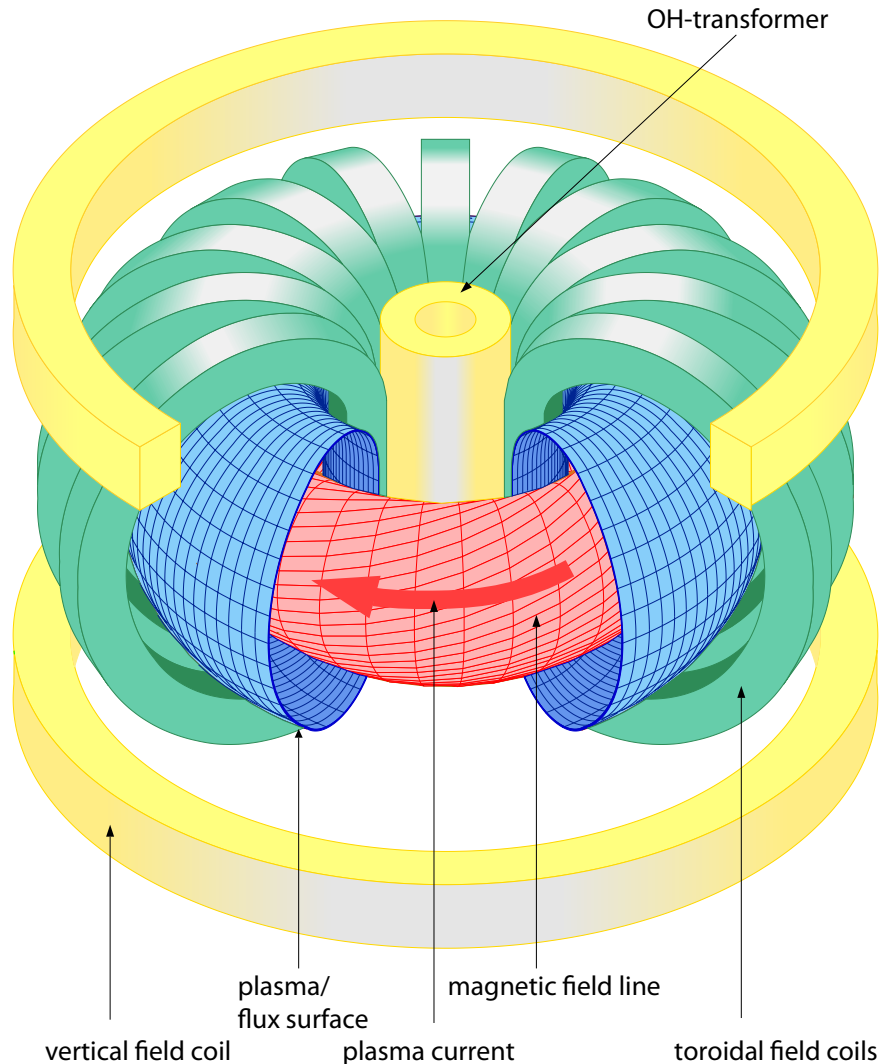


Figure 1.2: Tokamak design cartoon shows the plasma torus at the center and surrounded by the magnetic field coils (*image courtesy of ASDEX Upgrade, Garching*).

The toroidal magnetic field along the torus (\mathbf{B}_{tor}), is generated by the current-coils (in green in Figure 1.2) wound up around the torus. The primary (Ohmic) transformer coils (in yellow, marked as OH-transformer) are placed at the center of the torus. The plasma itself acts as a secondary coil coupled to the transformer. When there is a sudden change in the current in the primary coils an induced voltage is established in the plasma along the torus. This induced voltage accelerates the

1. INTRODUCTION

electrons along the torus and establishes the plasma current (I_p) (thick red arrow). In this process the plasma heats up to a certain temperature. The plasma current (I_p) generates a magnetic field in the poloidal plane, this magnetic field along with the magnetic field produced by the vertical field coils (in yellow) give rise to the poloidal magnetic field (\mathbf{B}_{pol}).

An equilibrium field (\mathbf{B}_{eqm}) is obtained as the vector sum of the \mathbf{B}_{tor} and \mathbf{B}_{pol} at each point in the plasma. The field lines of the \mathbf{B}_{eqm} can be imagined as a spring with its end connected back to its start, placed in the horizontal plane of the torus. The winding of the spring is tighter if the enclosed plasma current is higher. The total plasma volume (solid torus) can be imagined as a set of springs enclosing one another. In principle each spring or the \mathbf{B}_{eqm} field line is embedded in a single (hollow torus shaped) curved surface (e.g., red and blue surfaces in Figure 1.2). On these surfaces the (normalized) poloidal flux (ψ_{pol}) of the poloidal magnetic field \mathbf{B}_{pol} is constant. The tokamak poloidal cross-section plane can also be expressed by a single coordinate - normalized poloidal radius (ρ_{pol}); similar to the radial coordinate in cylindrical coordinates. Both ψ and ρ (for convenience the suffix 'pol' is dropped) can be mapped to one another by $\rho = \sqrt{\psi}$. The surface ψ corresponding to a particular ρ is also denoted as ψ_ρ .

In many modern tokamaks an additional set of current carrying coils (lying in the horizontal plane), generating an extra poloidal field, are used in order to shape the poloidal cross section of the plasma. A detailed description can be found in [13; 14].

The induced plasma current leads to a plasma temperature up to ~ 1 keV (also referred as Ohmic heating). The other most important heating modes consist of heating through resonant electro-magnetic waves and neutral particle beams, raising the plasma temperatures up to few tens of keV.

1.4 Plasma heating basics

Heating of the plasma means increasing the kinetic energy of all the plasma species, i.e., ions and electrons. There exist different methods for heating the plasma. No single method can heat all the plasma species equally and uniformly.

1. Ohmic heating (OH)

In most of the tokamaks, the plasma current is driven by the induction method. In this method the plasma-torus is treated as a secondary current carrying coil.

The plasma-torus carries an induced current as a response to the changing current in the central primary transformer. The induced current density (j) is in turn related to the transformer power (P_{OH}) as

$$P_{OH} = \eta j^2, \quad (1.5)$$

where, η is the plasma resistivity. However, the plasma resistivity drops with the increase in plasma temperature

$$\eta \propto T^{-3/2}. \quad (1.6)$$

By this process alone it becomes insufficient to drive the plasma to reactor relevant temperatures.

2. Neutral beam injection heating (NBI)

In this method, a high energy beam of neutral atoms is injected across the magnetic surfaces right into the plasma. At ASDEX Upgrade both, plasma and beam consists of deuterium. Similar to the concept of Newton's pendulum, the energy transfer between (same masses) the deuterium-beam particles and deuterium plasma-particles is more efficient than other gas beams. Through collision the energetic atoms share their energy with the other particles.

At high beam energies (100 keV), the NBI causes heating of both electrons and ions. The fraction of energy imparted on ions become dominant if the beam energy is slightly smaller than a critical energy (E_c) given by

$$E_c = 14.8 \frac{Z_b}{Z_p^{2/3}} T_e, \quad (1.7)$$

where Z_b , Z_p are the charge states of beam ions and plasma ions respectively, and T_e is the electron temperature.

At ASDEX Upgrade the D-beam energy is 55 keV and the critical energy of 3 keV deuterium plasma is $E_c = 57$ keV [15]. The dominant heating of ions also causes strong emission of neutrons of few MeVs.

1. INTRODUCTION

3. Wave heating (RF)

In this method, high power electromagnetic waves are injected in to the plasma. Depending on the wave-frequency (ω) and plasma density certain plasma species can be heated. The propagation of EM wave through a magnetized multispecies plasma is subjected to a number of resonances.

A charged particle (q) moving in oblique direction in the presence of equilibrium magnetic field (B_{eqm}) performs cyclotron motion at a frequency (and its harmonics) given as

$$\omega_{ce,ci} = \frac{ql}{m_{e,i}}|B(R)| \quad (1.8)$$

where $l = 1, 2, 3 \dots$ is the harmonic integer, q is the electronic charge, $m_{e,i}$ is the mass of electron or ion, and ρ is the normalized plasma radius. As the B_{eqm} is a smooth function of R and falls roughly as $1/R$, the cyclotron frequency also varies along R in a similar manner.

The externally launched EM waves can resonate with the cyclotron motion of a certain plasma species (electron or ion) at a certain radial position (ρ), depending upon the choice of the frequency $\omega_{ce,ci}$.

The RF heating predominantly occurs in these four frequency ranges, (a) Alfvén waves (1-10 MHz), (b) Ion cyclotron frequency (ω_{ci} 1-10 GHz), (c) Electron cyclotron frequencies (ω_{ce} 50-150 GHz), and (d) Lower hybrid ($\omega_{LH} \approx \sqrt{\omega_{ci}\omega_{ce}}$ few GHz).

Here, we will mainly focus on the electron cyclotron (EC) heating among the other mechanisms.

1.4.1 Consequence of induced voltage: runaway electrons

The collisional drag force (F_{co}) on an electron by the bulk plasma increases with increase in its velocity.

The induced parallel electric field (E_{\parallel}) accelerates the electrons with the force qE_{\parallel} until it is balanced by the opposing collisional drag force (F_{co})

$$qE_{\parallel} = F_{co}. \quad (1.9)$$

The collisional drag force, however, is velocity dependent and above a critical velocity (v_c) the drag force decreases with increase in electron velocity. A small population of the electrons in the tail of the thermal distribution can experience lesser collisional drag as compared to the bulk electrons. The force due to E_{\parallel} on these high energy electrons starts becoming dominant and they get further accelerated. For these electrons, the imbalance between the two forces is ever increasing until the electrons finally run away. The critical electron energy above which the runaway would occur is [5]

$$E_c = 6.6 \times 10^{-15} \frac{n_e}{E_{\parallel}} \text{ keV}, \quad (1.10)$$

where n_e is the bulk electron density (in cm^{-3}), the parallel electric field (E_{\parallel}) is expressed in V/cm and the critical electron energy is obtained in keV. For example, at very low density $n_e = 1 \times 10^{13} \text{ cm}^{-3}$ and typical electric field of 10^{-3} V/cm , the $E_c = 66 \text{ keV}$.

1.4.2 The electron cyclotron (EC) wave in plasma

The propagation of an EC wave is characterized by analyzing the dispersion relation (square of the refractive index as a function of wave-frequency) at each point in the plasma.

First we picture an externally launched EC wave inside the plasma. The resonant region in the plasma is essentially very thin and can be approximated as a slab in which the equilibrium magnetic field (B_{eqm}) is taken as the z -axis, the radial direction (and the wave-vector \mathbf{k}) is along the x -axis, and poloidal direction is the y -axis.

For a wave traveling along the radial direction, $\mathbf{k} \perp \mathbf{B}_{eqm}$, there are two possibilities for the orientation of its electric field \mathbf{E}_{wave} . When $\mathbf{E}_{wave} \parallel \mathbf{B}_{eqm}$, it is an ordinary wave (O-mode) and when $\mathbf{E}_{wave} \perp \mathbf{B}_{eqm}$, it is called as an extraordinary¹ wave (X-mode) [16].

At ASDEX Upgrade, the second harmonic of the X-mode EC waves (i.e. 140 GHz at 2.5 T) are utilized in the heating scheme [15].

¹The name extraordinary arises due to the fact that the wave has a slightly higher phase velocity than the ordinary wave.

1. INTRODUCTION

1.4.2.1 Near the resonance

Near the resonance region, for the wave propagating along radial direction, the *square* of the perpendicular refractive index, n_{\perp}^2 , can vary quickly from a positive large number to a negative large number. Before the n_{\perp}^2 changes sign, it will be equal to zero on some equilibrium surface. The surface for which $n_{\perp} \rightarrow \infty$ is a resonant surface, where wave absorption occurs, and for which $n_{\perp} \rightarrow 0$ is a cut-off surface, where wave reflection occurs.

The EM wave can lose its energy in the resonant region by two resonant mechanisms. The first is a wave-particle collisionless resonant interaction as discussed in details in Section 1.4.3. The second is by transferring some of its energy to another plasma wave propagating in the same region, referred to as mode conversion [17].

In the resonance, the wave can be directly absorbed or undergo mode conversion into another wave branch which propagates in the plasma[18]. These mode converted plasma waves are supported by at least one particle species in the plasma and they propagate to a region where the waves satisfy the wave-particle resonance condition. The examples of mode converted plasma waves include Alfvén waves and the family of Bernstein waves.

1.4.3 The wave-particle interaction

As an extraordinary wave approaches closer and closer to the resonance region, the wave no longer remains a pure transverse wave, it develops a strong longitudinal component (E_x). It is this feature of the wave which is then responsible for resonant absorption [19]. The longitudinal polarization can be decomposed into two components, left- and right-hand circular polarization. For that circularly polarized wave, the electric field vector rotates in the same direction as that of the electrons gyrating in the B_{eqm} , the electrons are constantly accelerated, increasing their perpendicular energy [20].

The collisionless wave dissipation is governed by the wave-particle resonance condition [17; 21]

$$\omega - k_{\parallel}v_{\parallel} - \frac{l|\omega_{ce}|}{\gamma} = 0, \quad (1.11)$$

where $l = 0, 1, 2, 3 \dots$ and γ is the relativistic Lorentz factor. The condition when $l = 0$ is known as the Landau resonance in which the electron gains energy in the

direction parallel to the B_{eqm} , known as electron Landau damping process. The lower hybrid (LH) waves use this resonance condition ($l = 0$)

$$\frac{\omega}{k_{\parallel}} - v_{\parallel} = 0, \quad (1.12)$$

since they have parallel phase velocity (ω/k_{\parallel}) ranging from electron thermal velocity to the velocity of light and can couple to both thermal and superthermal electrons, heating them means also driving a current.

For all other values of l , $l > 0$ or $l < 0$,

$$\left[\frac{\omega}{k_{\parallel}} \pm \frac{l|\omega_{ce}|}{k_{\parallel}\gamma} \right] - v_{\parallel} = 0, \quad (1.13)$$

the cyclotron resonance takes place in which the perpendicular energy of the electrons is increased [22]. For positive l only those electrons are resonant with the wave which have their parallel velocity greater than parallel phase velocity of the wave. On the other hand, for negative l only those electrons are resonant with the wave which have their parallel velocity less than parallel phase velocity of the wave. That means it is only a small sub-set of electrons which participate in the resonance.

The interesting property about the EC waves is that – they can undergo a resonance even when propagating exactly perpendicular to the \mathbf{B}_{eqm} , i.e., $k_{\parallel} = 0$. The resonance condition becomes

$$\omega - \frac{l|\omega_{ce}|}{\gamma} = 0. \quad (1.14)$$

Remember, ω_{ce} is a smooth function of R and roughly falls as $1/R$. The above equation also tells that, in the non-relativistic case ($\gamma = 1$) the resonance is independent of the electron velocity

$$\omega - l|\omega_{ce}(R)| = 0 \quad (1.15)$$

and hence all the electrons at a fix radial position $R = R_0$ would undergo resonance with the EC wave of frequency ω . In most of the tokamak operations the electrons with energy in the order of keVs are mildly relativistic. For example, the velocity of an electron of 10 keV energy is $0.2c$. The more realistic condition could be obtained by Taylor expanding the γ -factor

$$\omega - l|\omega_{ce}(\rho)| \left(1 - \frac{v^2}{2c^2} \right) \approx 0. \quad (1.16)$$

1. INTRODUCTION

The second term can be considered as an equivalent electron cyclotron frequency $\omega'_{ce}(R)$, such that, at any given location R , $\omega'_{ce} < \omega_{ce}$.

The frequency (ω) of the EC wave is tuned to resonate with the electrons at a particular location R , but the Equation 1.16 shows that the resonance position is slightly different for different electron energies. The direction of the shift is such that an EC wave launched from the low field side will first undergo resonance with the most energetic electrons than the less energetic ones.

Electrons can be accelerated and decelerated depending on their phase with respect to the wave. Saturation appears when the two cases balance! It is seen as a plateau in the electron distribution function.

Even though EC waves carry little parallel momentum, they can be used for current drive. The EC resonance heating is a very diverse scheme and has already been demonstrated for its capability of – full current drive [23; 24], current profile control [25], and the stabilization of MHD instabilities [26; 27; 28; 29], and obviously bulk heating purpose.

Between a wave launched perpendicular and oblique to the B_{eqm} , the later one is efficiently absorbed by the electrons of high parallel velocity. Moreover, the waves obliquely launched (from either high field or low field side) first undergo resonance with the high energy electrons than the bulk thermal electrons. This makes the EC waves more interesting for efficient ECCD [20]. The ECRH is capable of selectively heating the high energy electrons through the relativistic resonance condition to obtain a local current drive [30; 31].

Even for perpendicular waves, according to Fisch-Boozer method [32], the EC waves used to transfer the energy to the perpendicular (to B_{eqm}) electrons, leads to an asymmetric resistivity, since the high energy electrons experience less drag. This asymmetry generates an effective electron flow in the parallel direction forming a current, with efficiency comparable with that of the LH current drive [33; 34].

The evolution of the plasma depends on the balance between the collision rate and the power input. If the collision rate is high enough then the Maxwellian distribution shape is preserved. As the temperature increases the collisions become infrequent and the Maxwellian shape starts to deform, by forming a tail towards the higher energy, termed as suprathermal tail.

A small suprathermal population has both beneficial and detrimental effects. A superthermal population can lead to the non-confined runaway electrons, which can cause a damage to the plasma vessel, and is a major concern for the future tokamak

device, ITER [35; 36]. For the radio frequency current drive and current profile shaping applications the superthermal tail is advantageous.

The properties of the wave propagation and the energy deposition requires solving kinetic models for the plasma. There exist numerical tools to calculate the wave propagation and the evolution of the plasma [37; 38; 39; 40] as discussed in the next Section 1.5.

1.5 Numerical modelling of the electron distribution function

The electrons in the plasma gain energy while the plasma is heated by means of externally launched electromagnetic fields. The energy is shared among different plasma species dominantly by the collisions. In the process of constant gain and loss of energy by the electrons, the distribution function of the electrons evolve until the equilibrium is attained.

If we consider a small unit volume dV – in the plasma, at location \mathbf{x} (in an arbitrary coordinate system), in order to compute the dynamics of all the electrons inside that volume, we need to know how many of the electrons are there with a certain velocity \mathbf{v} at a given time. The function that describes the probability of how the electrons are distributed over different velocities, is the distribution function $f(\mathbf{x}, \mathbf{v}, t)$.

At any point in time, the distribution function of the electrons is affected by the following factors:

- Wave heating

The electromagnetic waves interact with the resonant electrons and transfer their energy. This is represented by the quasi-linear wave-particle scattering operator $Q(f)$, operating on the distribution function. The quasi-linear term is the lowest-order nonlinear term obtained by averaging the nonlinear terms over a large number of wave periods.

- Inductive electric field

The electrons also experience the inductive electric field (E_{\parallel}), and are constantly accelerated in the toroidal direction. The effect of inductive electric field is represented by the operator $E(f)$ operating on the distribution function.

1. INTRODUCTION

- Collisional relaxation

The collisions allow transfer of energy among the electrons and ions and lead to plasma diffusion and other transport processes. The collisions between the electrons depend on their relative velocities. Once $f(\mathbf{x}, \mathbf{v}, t)$ is known at time t_0 , we can then allow the collisions to reorganize the particle energies, to obtain $f(\mathbf{x}, \mathbf{v}, t)$ at some later time t . The process of collision is represented by the operator $C(f)$ operating on the distribution function.

The evolution of the distribution function is a competition between the energy gain (wave heating) and loss (collisions) by the electrons and can be described by the so called Fokker-Planck equation

$$\underbrace{\left. \frac{\partial f}{\partial t} \right|_{RF}}_{Q(f)} + \underbrace{\left. \frac{\partial f}{\partial t} \right|_{collisions}}_{C(f)} + \underbrace{\left. \frac{\partial f}{\partial t} \right|_{E_{\parallel}}}_{E(f)} = \frac{\partial f}{\partial t}. \quad (1.17)$$

Under the equilibrium condition the time derivative on the right hand side becomes zero

$$\left. \frac{\partial f}{\partial t} \right|_{RF} + \left. \frac{\partial f}{\partial t} \right|_{collisions} + \left. \frac{\partial f}{\partial t} \right|_{E_{\parallel}} = 0. \quad (1.18)$$

resulting in the equilibrium electron distribution function (subscribed 'e' for electrons) $f_e(\mathbf{x}, \mathbf{v})$ [37].

Due to the particular magnetic geometry of the tokamaks, the electrons with higher perpendicular velocity may get reflected at the high field side due to the magnetic mirror effect. This leads some of the electrons to be trapped and getting bounced back. The electrons which are not trapped, keep rotating periodically along the poloidal direction. In both of these cases where the electrons are trapped or pass by, their motion is periodic and generally called as the *bounce* motion. The equation that describes the evolution of the distribution function is averaged over this bounce motion, and termed as the bounce-averaged equation. The distribution function is also averaged over the gyro-phase angle of the electrons gyrating around the magnetic field lines.

The numerical modeling of the electron distribution function for the ASDEX Upgrade discharges has been recently realized [41]. For this purpose, the beam tracing code TORBEAM [38] is coupled to the Fokker-Planck solver RELAX [37]. The beam

tracing code TORBEAM calculates the propagation effects of the electron cyclotron waves inside the plasma. The code RELAX solves the bounce-averaged quasi-linear relativistic Fokker-Planck Equation 1.18 of the description of the effects of collisions, Ohmic electric field and quasi-linear wave-particle interaction.

The code TORBEAM is based on the wave description of the beam, whereas the code RELAX is optimized for the ray-based description of the beam, a novel module has been added to the code TORBEAM for the calculation of the bundle of extended rays [41]. Such ray-based description of the beam is totally equivalent to the standard beam tracing description.

The numerical electron distribution function is a function of electron momentum (\mathbf{p}) normalized to mc , where m is the mass of electron and c is the speed of light, and the pitch angle θ , i.e., the direction of \mathbf{p} with respect to \mathbf{B}_{eqm} . The distribution function is evaluated at every normalized magnetic flux surface (ψ). The electron distribution function, in the end is represented as

$$f_e \equiv f_e(\psi, p, \theta). \quad (1.19)$$

The calculations of the distribution functions f_e were performed for specific plasma scenarios in order to make comparison with the observations, as described in Chapter 5.

1.6 Bremsstrahlung emission

As discussed earlier, the electrons in plasma are subjected to collisions with rest of the plasma particles and emit radiation mainly by bremsstrahlung process. At higher and higher energies the radiation is predominantly in the hard X-ray regime. Measurements of the bremsstrahlung radiation in the X-ray regime gives the direct reflection of the energetics of the underlying electrons. In section below, first we will describe bremsstrahlung radiation cross-section, which is then applied to two cases, thermal and nonthermal electron distributions.

It is well known that any electric charge in the acceleration (or deceleration) motion emit radiation, in the direction perpendicular to its acceleration [42]. The electrons are constantly scattered through the Coulomb field of other plasma species. In the interaction with the Coulomb field of a single ion, the electron with sufficiently high energy essentially remains free even after the interaction, hence the

1. INTRODUCTION

bremsstrahlung radiation is also referred as free-free radiation. The frequency of the radiation emitted can be anything between 0 to maximum value allowed by the electron kinetic energy.

The power radiated per unit frequency bin is given by the Larmor's formula [42]

$$\frac{dW}{d\omega} = \frac{2e^2}{3\pi c^3} |\Delta\mathbf{v}|^2. \quad (1.20)$$

When a fast electron (of charge $-e$) interacts with an ion (of charge $+Ze$) at a distance \mathbf{b} , we can assume the direction of the velocity vector remains roughly the same. The change in velocity ($\Delta\mathbf{v}$) can be then estimated simply by the force (\mathbf{F}_{e-i}) on the electrons by the ion

$$\mathbf{F}_{e-i} = \frac{(Ze).e}{|\mathbf{b}|^2} = m \frac{\Delta\mathbf{v}}{\Delta t} \quad (1.21)$$

where, m is the mass of electron. The energy lost by the electron to overcome the above force on it, is in the form of radiation. The power (W) radiated per radiation frequency bin ($d\omega$) is

$$\frac{dW(b)}{d\omega} = \frac{8Z^2e^6}{3\pi c^3 m^2} \frac{1}{v^2 b^2}. \quad (1.22)$$

Let (n_e) and (n_i) be the electron and ion density respectively. All the electrons with velocity v passing by a single ion will form a flux of $n_e v$. For the radius equal to the (electron-ion separation) distance b , consider a ring of area $2\pi b db$ with an ion at the center. Total number of electrons interacting with the single-ion within the differential area $2\pi b db$ will be $2\pi b db \cdot n_e v$.

The total power radiated per unit volume (dV) by all the single-speed (v) electron interacting with the uniform ions density (n_i) is estimated

$$\frac{dW}{d\omega dV dt} = n_e n_i 2\pi v \int_{b_{min}}^{b_{max}} \frac{dW(b)}{d\omega} b db, \quad (1.23)$$

i.e.,

$$\frac{dW}{d\omega dV dt} = \frac{16e^6}{3c^3 m^2 v} n_e n_i Z^2 \int_{b_{min}}^{b_{max}} \frac{db}{b} = \frac{16e^6}{3c^3 m^2 v} n_e n_i Z^2 \ln \left(\frac{b_{max}}{b_{min}} \right). \quad (1.24)$$

Here b_{max} is the point, roughly when $b_{max} \equiv v/\omega$ after which the Coulomb interaction is too weak to contribute to the integral. The lower limit b_{min} is evaluated from

1.6 Bremsstrahlung emission

the argument of uncertainty principle $\Delta x \Delta p \gtrsim \hbar$, with $\Delta x \sim b$ and $\Delta p \sim mv$ we get $b_{min} = \hbar/mv$. Since the b_{max} and b_{min} are inside the argument of the logarithm, the accurate values are not necessary only the order of magnitude suffices. The exact value is stated in the terms of a correction factor or Gaunt factor $g_{ff}(v, \omega)$ such that the bremsstrahlung emission by the single speed electrons is

$$\frac{dW(v, \omega)}{d\omega dV dt} = \frac{16e^6}{3c^3 m^2 v} n_e n_i Z^2 g_{ff}(v, \omega) \dots \text{ (ergs} \cdot \text{s}^{-1} \cdot \text{cm}^{-3} \cdot \text{Hz}^{-1}\text{)}. \quad (1.25)$$

The Gaunt factor is a function of electron energy and the emission frequency.

If the electron distribution function ($f_e(v)$) is known then the total radiation power is obtained by integrating Equation 1.25 over $f_e(v)$

$$\frac{dW(\omega)}{d\omega dV dt} = \frac{\int_{v_{min}}^{\infty} \frac{dW(v, \omega)}{d\omega dV dt} f_e(v) dv}{\int_0^{\infty} f_e(v) dv} \quad (1.26)$$

1.6.1 Thermal bremsstrahlung

The thermalized electrons are represented by a Maxwellian distribution function, characterized by temperature (T)

$$f_e(v) \propto v^2 \exp\left(-\frac{mv^2}{2kT}\right) dv. \quad (1.27)$$

Substituting above equation in Equation 1.26, and using the lower limit $v_{min} \equiv \sqrt{2\hbar\nu/m}$ and $d\omega = 2\pi d\nu$, the thermal bremsstrahlung emission is obtained [42]

$$\frac{dW}{dV dt d\nu} = \frac{2^5 \pi e^6}{3mc^3} \left(\frac{2\pi}{3km}\right)^{1/2} T^{-1/2} Z^2 n_e n_i e^{-\frac{\hbar\nu}{kT}} \bar{g}_{ff}. \quad (1.28)$$

Evaluating in CGS units (ergs \cdot s $^{-1}$ \cdot cm $^{-3}$ \cdot Hz $^{-1}$ and T in kelvin)

$$\frac{dW}{dV dt d\nu} = 6.8 \times 10^{-38} Z^2 n_e n_i \frac{e^{-\hbar\nu/kT}}{\sqrt{T}} \bar{g}_{ff}. \quad (1.29)$$

For the convenience of our further analysis, the above equation is converted in to the units ($W \cdot \text{cm}^{-3} \cdot \text{eV}^{-1}$ and T in keV) and substituting the photon energy $E = \hbar\nu$

$$\frac{dW}{dV dt dE} = 4.8 \times 10^{-34} Z^2 n_e n_i \frac{e^{-E/T}}{\sqrt{T}} \bar{g}_{ff} \quad (1.30)$$

1. INTRODUCTION

where, $\bar{g}_{ff} \equiv \bar{g}_{ff}(T, \nu)$ is a velocity averaged Gaunt factor.

1.6.2 Nonthermal bremsstrahlung

The radiated power by the nonthermal electron distribution function ($f_e(v)$) is obtained by Equation 1.26. Since usually the nonthermal distribution function is obtained numerically (solution to the Fokker-Planck equation), the radiated power has to be obtained by performing numerical integration over the given $f_e(v)$, described in more details in Section 5.5.1.

Another modeling approach is implemented based on the assumption that the non-thermal tail is approximately represented by another Maxwellian distribution. The total distribution is then of a bi-Maxwellian form where the second temperature characterizes the non-thermal tail, see Section 5.5.2 for more details.

1.7 Motivations and the goals of the thesis

Electron Cyclotron Resonance Heating (ECRH) is one of the major plasma heating schemes in tokamaks. As discussed previously, ECRH has not only a promising heating scheme, but recent demonstrations have also shown that the increased efficiency of the current drive (ECCD) purely by EC waves [43] is almost comparable with that of the LH current drive. ECCD has the potential to replace the induction based current drive in pulse operated tokamak and convert into a steady state tokamak. Due to these important factors the ECRH technique is gaining further importance. Especially for ITER like machines it is very crucial to explore the characteristics of ECRH and ECCD [44; 45].

With high power ECRH and ECCD, generation of a considerable fraction of fast electrons is inevitable [43]. The electrons can carry energies up to a several keV, factor of 10 times higher than the thermal energy. Among many questions related to the non-thermal electrons, the important questions are: (i) What is the form of the energy distribution of the non-thermal electrons? (ii) How much of the total plasma current do they contribute to? (iii) what fraction of electrons fall into the non-thermal population? (iv) what effect do they have on the bulk plasma, and many such interrelated questions. The physics of plasma heating and current drive is crucially linked to the kinematics of the non-thermal electrons, because they strongly affect the total plasma current and the shape of the current density profile. Moreover,

the careful study of the non-thermal electrons is essential in understanding the link between the different populations transiting from thermal to non-thermal to runaway electrons. In this thesis, we attempt to answer some of these questions.

To understand the kinematics of the non-thermal electrons, the most valuable piece of information resides in the hard X-ray region of the electromagnetic spectrum, as the non-thermal electrons emit in this energy range by the processes of collision with the rest of the plasma, making the X-ray diagnostics one of the crucial tools.

At ASDEX Upgrade, currently there exists a soft X-ray diagnostics, bolometric type detectors, consisting of a set of pin-diode, with several lines of sight, which provide key information on core plasma oscillations [46; 47]. Recently, a Pulse Height Analysis based soft X-ray diagnostics has been refurbished [48], which provides additional spectral information on the thermal state of the plasma from the bremsstrahlung emission in the range 1-15 keV. It also allows monitoring the presence of different impurities with their relative concentrations.

Towards more extreme energies, ASDEX Upgrade is equipped with four standard γ -ray (up to few MeVs) detectors. These are liquid scintillator based and fast counter type detectors (no spectral information). They provide information on the γ radiation yield from the fusion plasma or secondary radiation from many plasma vicinity components as well as the presence of runaway electrons. Moreover, a compact neutron spectrometer (CNS) based on liquid scintillator was recently installed and tested [49; 50]. Although CNS is primarily designed to study the neutron energy distribution function, it did show capability of detecting the gamma spectrum up to 1.5 MeV during plasma disruption scenarios.

As a part of this thesis, the diagnostics were developed, for the energy range of 1 - 20 keV (soft X-rays), and an intermediate energy range, i.e., 10-500 keV (hard X-rays), to fill in the observational gap between the soft X-rays and the γ -rays. At the core of the diagnostics is an advanced technology Silicon Drift Detector (SDD) coupled to a CsI(Tl) scintillator crystal.

The SDD+CsI(Tl) combination, till now has not been explored in the extreme environments like tokamaks. One of the goals was to test the compatibility and suitability of such detector in tokamak environment and comment on its potential as an X-ray diagnostic for future machines like ITER, Wendelstein-7X [51; 52].

Recently, SDD based soft X-ray diagnostics have already been implemented in many tokamaks, and have already shown impressive performances. In this thesis, we started with the SDD based soft X-ray diagnostics and extended it to the less explored

1. INTRODUCTION

hard X-ray regime, obtaining a SDD+CsI(Tl) based hard X-ray diagnostics at ASDEX Upgrade tokamak.

Scintillator+photo-multiplier tube (PMT) based hard X-ray diagnostics are standard in almost all tokamaks [53; 54]. Most of these diagnostics avail poor energy and time resolution which affects the quality of the measured spectrum. The suitability of the detector is limited if the quantum efficiency of the detector does not span the energy range of interest. The unknown (or uncharacterized) nature of the detector response forces an incompleteness in the spectral analysis and the true plasma parameters (e.g, electron temperature, fraction of electrons, etc.) are not deducible [55; 56; 57; 58; 59].

For this reason, in this thesis, we carry out an extensive study on the characteristics of the detector response. We also develop the methodology based on forward model fitting, to deduce the plasma parameters from the spectral data, by taking into account the proper detector response function. After having the necessary tools developed, we then performed the experiments in order to explore in more details the physics of ECRH and the generation of superthermal electrons. A systematic experimental case study is performed.

Finally, the experimental measurements in selected scenarios are validated through the numerical Fokker-Planck calculations obtained in collaboration with O. Maj and E. Poli (Max Planck Institute for Plasma Physics, Garching). The Ray-tracing and Fokker-Planck code provides key inputs to the study of the superthermal electrons, as they provide the energy deposition profiles and efficiency [38]. Our measurements are aimed to provide the tool to testify the numerical predictions for the ASDEX Upgrade plasmas and eventually understand the energetics of the non-thermal electrons.

“In order to make an apple pie from scratch, you must first create the universe.”

- Carl Sagan

2

Instrumentation for the SX and HX diagnostics

2.1 Introduction

The nonthermal electrons of several keV of energy, radiate most of their energy in the X-ray range by the *bremsstrahlung* process (i.e. breaking radiation). Hence most of the information of the existence of nonthermal electrons is contained in the X-ray regime.

X-rays, lie towards the extreme high energy end of the electromagnetic spectrum and they can penetrate deeper into a material before they completely disappear. In order to do spectroscopy, the goal is to stop every X-ray photons within a finite detection volume and correctly estimate its energy. A detector is a device which converts the light energy in to a measurable electrical signal. A photon is eventually converted into a bunch of free electrons setting a current in the detector. The number of electrons set free is proportional to the energy of the incident photon.

A good detector is one in which the photons dumps all their energy, and can perceive not only the information about the energy but also the time of the interaction.

2. INSTRUMENTATION FOR THE SX AND HX DIAGNOSTICS

Such an ideal detector is then best suited to comment on the underlying energetic electrons in the plasma. Real detectors (especially in X-ray regime) are far from ideal. It is mainly due the complex processes involved in radiation interaction with matter.

There exists a variety of detectors, each with some advantages and disadvantages, serving certain type of purposes. The choice of the detector is crucial in matching with the goals. One should survey or test different detectors in order to decide on the compromise between advantages and disadvantages. Carrying out such a survey or tests of different detectors was beyond the scope of my thesis.

However, one of the goals was to test the detectors which are already in use in Astronomy (space borne X-ray Telescopes), as potential detectors for the tokamak plasma.

We adopted the detector originally developed for astrophysical studies [60] and brought into the fusion environment by taking necessary steps. In fact, the similar detectors are already implemented on the X-ray satellite telescopes like XMM-Newton [61], eROSITA [62] and some advanced detectors planned to be implemented in near future X-ray telescopes [63]. We will discuss the advantages and disadvantages of the choice of our detector in the Sections 2.3 and 2.4, while discussing the properties of the detector.

First, in this chapter, we describe the basics of the detector properties and the necessary instrumentation and then in the Chapter 3 we discuss how the diagnostics was constructed and the challenges in the detector characterization were resolved by laboratory tests. Before we introduce the detector and the following trail of instruments, we will review how the X-ray radiation interacts with our detector material.

By the word X-rays, we are referring to energies from 1 keV up to 500 keV. Through the text we will be referring to two distinct energy ranges as we call them, *soft* X-rays (SX) from 1-20 keV and *hard* X-rays (HX) from 20-1000 keV. Some time we will refer to 100-500 keV energy range as *extreme* hard X-rays, but its just the matter of convenience for dividing the whole 1-500 keV X-ray energy range, based on the underlying emission mechanism or simply the detector involved. In the nuclear physics sense, the high energy end of the spectrum is simply divided into X-rays or γ -rays, based on whether the emission is of atomic origin (electron's transition) or nuclear origin. In the tokamak plasma studies we will refer to γ -rays not only to the line emission of nuclear origin, but also to the continuum emission from electrons with energies up to tens MeV such as runaway electrons.

2.2 Interaction of the radiation with detector material

Photons, as a function of their energy, offer different cross-sections for different physical processes of interaction with any solid state matter. X-rays interact with matter in many ways. There are three interaction processes which play a major role in the radiation detection [53],[42], [64].

- Photoelectric absorption

In the photoelectric effect, a photon completely disappears by transferring its energy to an electron in an atom. The interaction is only with an atomic electron and cannot take place with free electrons. The electron ejected from the atom, i.e. the photo-electron, carries the energy

$$E_e = E_\gamma - E_b, \quad (2.1)$$

where, E_γ is the energy of incident photon and E_b is the binding energy of the electron to the atom.

The vacancy in the electrons shell is quickly filled by the rearrangement of the electrons from other shells. In this process more than one characteristic X-ray photons can be emitted. Most probably these X-rays are absorbed again within a small volume by photoelectric absorption but this time with a less tightly bound electron. The photoelectric absorption in a material strongly depends on the atomic number. An empirical relation for the photoelectric absorption cross-section [65], is given by

$$p \propto \frac{Z^n}{E_\gamma^{7/2}} \quad (2.2)$$

where, $4 < n < 5$, therefore high-Z materials are good absorbers of hard X-rays and γ -rays; for the same reason they constitute most of the X-ray detectors.

It is possible that, the photoelectron or characteristic X-ray photon created close to the detector boundary can leave the detector volume. Any loss of energy would lead to the shift in the estimate of the photon energy.

- Compton scattering

In Compton scattering, the photon scatters off the electron inelastically, parting some of its energy to the scattered electron. The kinematic analysis gives the

2. INSTRUMENTATION FOR THE SX AND HX DIAGNOSTICS

expression for the energy shared between the photon and the electron and the scattering angle. When the photon scatters off an electron at rest, the scattered energy of the photon is given as

$$E'_\gamma = \frac{E_\gamma}{1 + \frac{E_\gamma}{m_e c^2} (1 - \cos\theta)} \quad (2.3)$$

where

E_γ = the energy of the incident photon,

E'_γ = the energy of the scattered photon,

$m_e c^2$ = the rest mass of the electron (511 keV), and

θ = the scattering angle.

Note that E'_γ is never zero, i.e., the incident photon can never vanish by transferring all of its energy to the Compton-electron, unlike the photoelectric absorption where the photon is completely absorbed. This means, we cannot have the complete information about the photon's energy by a single Compton scattering event. A photon may undergo multiple scattering events within the detector before it completely vanishes. At low incident photon energies the scattering occurs in all directions, whereas at higher photon energies the scattering is more preferred in the forward direction. This means, a photon, after scattering off an electron, can escape out of the detector volume, without revealing information about its complete energy. Hence, the shape and size of the detector volume can play an important role in the detection process.

The scattering angle θ , in individual scattering events, can take any value between 0 to π , so the scattered electron energy E_e tends to have a continuum spectrum between $E_{e,min}$ (for $\theta = 0$) to $E_{e,max}$ (for $\theta = \pi$)

$$E_e = E_\gamma - E'_\gamma. \quad (2.4)$$

The maximum value of the $E_{e,max}$, corresponding to $\theta = \pi$, is referred to as Compton edge.

Towards the higher energies, the Compton scattering process becomes more prominent as compared to the photoelectric absorption and hence becomes important in characterizing the response of the detector.

2.2 Interaction of the radiation with detector material

- Pair production

In the pair production process a high energy photon interacts with a nucleus and is converted into electron-positron pair. Since the rest mass of electrons and positrons is 511 keV, the pair production process can only occur for the photon energy above a threshold of 1.02 MeV. For even higher energy photons the excess energy goes in the form of kinetic energy of the electron and positron. The positron, once thermalized, annihilates with an electron creating two photons, each of 511 keV. These photons (of almost half of the energy of the initial photon) can interact in the surrounding medium either by the photoelectric process or Compton scattering.

The probability (cross-sections) of a photon undergoing any of the above mentioned interaction processes is compared in the Figure 2.1. The cross-section data is obtained from the NIST XCOM database [66].

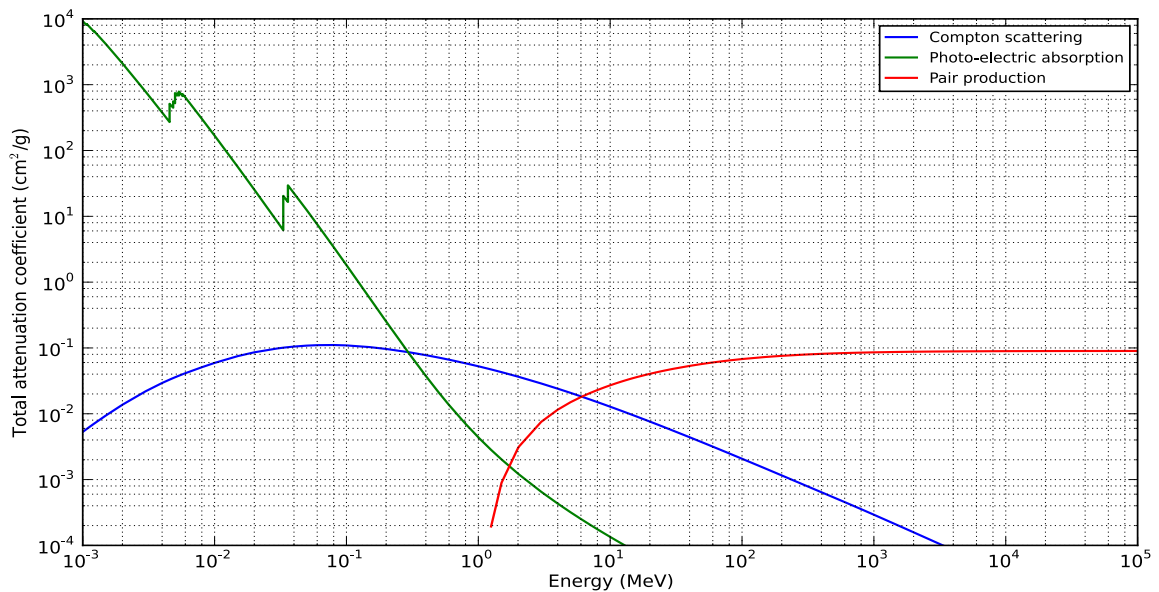


Figure 2.1: Comparison between radiation-matter interaction cross-sections of photo-electric (green), Compton scattering (blue), and pair production (red) respectively [66].

More detailed information on the radiation processes can be found in standard *Electrodynamics* textbook such as by D. Griffiths [67]

2.3 Working principle of the Silicon Drift type Detector (SDD)

The Silicon Drift type Detector (SDD) is at the core of our X-ray PHA diagnostics. In simple words it is a solid state detector, consisting of a thin silicon wafer. The name appears due to its inherently different technique of mobility of the charges inside it, as compared to usual pn-diode type solid state detectors [68].

The Silicon Drift technique, after being introduced in 1983 [69], has set a major leap in the X-ray detection technology. Just in the following year Rehak et. al. optimized the energy resolution and soon SDD became widely popular in the X-ray spectroscopy field [70]. The initial SDD design used to consist of voltage bias-rings on both sides of the detector, until in 1987 Kemmer et. al. from Munich, improved on the capacitance by placing the bias-rings only on one side of the detector. Since then the research and improvements by many different labs around the world, have led to a very mature X-ray detection technology. In fact some of the companies currently claim to have reached the energy resolution already touching the theoretical Fano-limit (discussed later) [71].

The detail review of the Silicon Drift Detector is given in Gatti and Rehak, 2005 [72]. The Silicon Drift Detector shows many advantages over other techniques including other solid state detectors as well as photo-multiplier tubes [73]. The SDD used in this thesis work, was designed at the Max-Planck-Institute's Solid-state Physics Laboratory in collaboration with the company PNsensorm GmbH [74]. The detector has been mainly developed and implemented in the space-based astronomical X-ray telescopes such as XMM-Newton [75] and near future projects [76]. The detector has also found applications in many fields such as, medical imaging, historical/geological sample's elemental analysis, particle accelerators, low temperature plasma, fusion plasma, etc., requiring high spectral, and time resolutions as well as spatial resolution [77; 78; 79].

The Figure 2.2 shows the actual photograph of the detector. The detector has an active area of 30 mm² i.e. a diameter of 6.2 mm and the thickness of 0.5 mm.

Before we go into details about the SDD, first we look at some of the distinct features of SDD as compared to other existing detectors (such as germanium detector, Si-PIN detectors or PMT based detector etc.)

- High energy resolution : ~ 140 eV at 5.9 keV Mn K_α line

2.3 Working principle of the Silicon Drift type Detector (SDD)



(a) Top view of the SDD

(b) Side view of the SDD

Figure 2.2: The Silicon Drift Detector (SDD) manufactured by MPG-HLL in collaboration with PNSensor GmbH.

- High photon handling rate : ~ 500 kcps ($\approx 1 \mu\text{sec}$)
- High peak-to-background ratio : up to 2000:1
- Thermo-electric cooling : less bulky setup
(no liquid helium/nitrogen cooling)
- Compact detector : 30 mm^2 ($\phi=5.2\text{mm}$) $\times 450 \mu\text{m}$
- Low leakage current : due to high purity Silicon
- Broad efficiency range: from 800 eV to 20 keV

2.3.1 Detector active volume

The schematic diagram of the detector is shown in Figure 2.3. The detector is a completely depleted silicon volume. X-ray radiation, along the passage through a detector's depleted volume, deposits energy into the medium and creates free electrons. In contrast to a photon, an electron, being a charged particle, remains readily captured within the medium; while it thermalizes, its energy is shared among many more electrons setting in turn them free. In a detector, the silicon volume is usually depleted by a proper bias voltage. X-ray interaction within this depletion region raises the electrons into the conduction band creating a number of electron-hole pairs. Usually

2. INSTRUMENTATION FOR THE SX AND HX DIAGNOSTICS

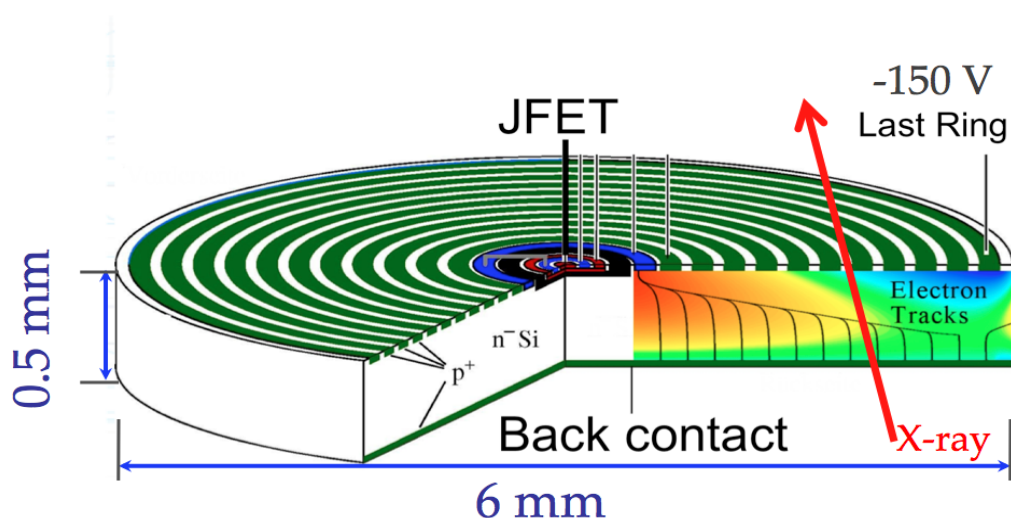


Figure 2.3: Schematic of the Silicon Drift Detector. It is a thin silicon wafer of area 30 mm² and thickness of 0.5 mm. The green rings create a negative voltage gradient, forcing the free electrons to drift towards the center (*image courtesy of B. Huber; IPP, Garching*).

the number of electron-hole pairs is linearly proportional to the energy dissipated by the X-rays.

The silicon volume consists of a specific three dimensional electric potential gradient structure, such that the electron cloud drifts radially inwards to the centrally located anode. The electric potential gradient structure is created by a set of concentric cathode rings (shown in green color in Figure 2.3). The rings are applied an increasingly reverse biased voltage. The rings cover one surface of the detector. The opposite surface, serving as the radiation entrance window, is made up of non-structured homogeneous sensitivity surface, termed as back contact surface. All the electrons created drift to the anode at the center and the holes drift to the nearby cathode ring. Unlike the old detectors, the SDD has an integrated JFET at the anode at the center and the charges are fed to the JFET (marked at the center in Figure 2.3). Having a centrally integrated JFET greatly reduces the capacitance between the central anode and the JFET and results in the reduction of the electronic noise greatly.

The sudden increase in current at the JFET produces a step-like voltage as an output, as well as provides a first stage of amplification. Any reduction of noise in the very first stage of amplification gives a significant improvement in the energy resolu-

2.3 Working principle of the Silicon Drift type Detector (SDD)

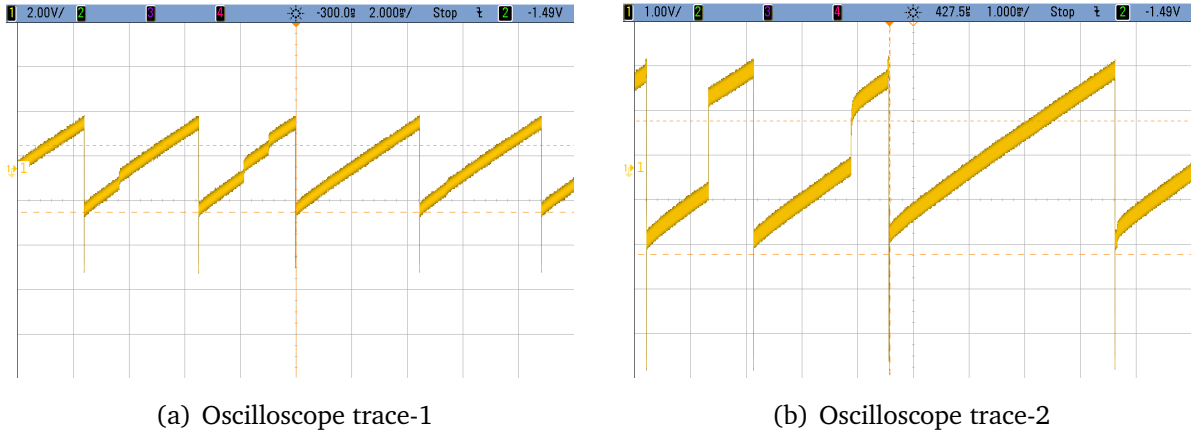


Figure 2.4: Two examples of the reset diode output signal, showing a continuous ramp-up. For every photon event a sudden voltage step appears on top of the ramp-up signal. The reset occurs as soon as the threshold is reached.

tion, and provides higher energy resolution at shorter shaping times. The collection of charges takes a very small but finite time (typically between 10-100 ns), depending upon the size of the detector and where the photon hits. It mainly decides the rise time of the charge-step.

2.3.2 Reset preamplifier

The preamplifier accumulates the charge pulses from every photon event and a staircase of output voltage is obtained as a function of time, see Figure 2.4. When there are no photon events the preamplifier still keeps collecting the charges reaching at the diode (due to thermal noise), and produces simply a steadily increasing voltage signal. When the voltage finally reaches a maximum threshold, the anode is flushed out and the voltage is rapidly reset to zero with the help of an active transistor. During this reset period, the detector calls for a dead-time. The detector output is gated for a short time window ($\sim 10\text{-}20 \mu\text{sec}$), see Figure 2.7

The frequency of the reset depends on the average (1) energy and (2) rate of the incident radiation, and (3) the thermal noise (depends on the temperature of the active volume). When there are no photons incident and the detector is cooled down to $-20 \text{ }^\circ\text{C}$, the reset period for our detector could reach up to 25 msec. The energy information about every incident photon is in the height of the individual steps in the voltage staircase, which is further processed by the shaping amplifier stage or *shaper*.

2. INSTRUMENTATION FOR THE SX AND HX DIAGNOSTICS

The preamplifier circuit is always situated as close to the detector as possible. The preamplifier output then can be transmitted to the later processing units placed at farther distances. The photograph of the preamplifier electronics is shown in the Figure 2.5

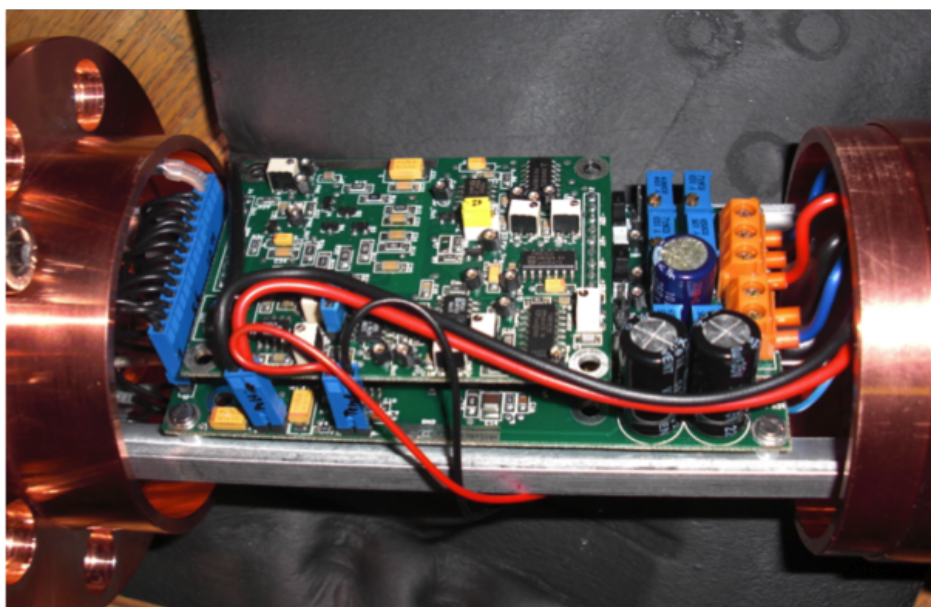


Figure 2.5: The preamplifier circuit board, sitting close to the SDD.

2.3.3 Power supply

The preamplifier electronics board is operated with a ± 24 V power supply. The SDD needs a negative high voltage (-150 V) power supply. With the voltage divider, the concentric cathode rings (shown in green in Figure 2.3) are maintained at -20 V (innermost) to -150 V (outermost). The detector is actively cooled to ~ -20 °C by a thermo-electric Peltier element operated typically at a current of 0.4 A.

2.3.4 Block diagram

Different processing blocks and their schematic electronic functioning is shown in the Figure 2.6. The four main stages in the X-ray detection are, (1) Detector, (2) Preamplifier, (3) Shaper, and (4) Multi-Channel Analyzer (MCA). Finally the MCA produces a pulse height histogram, which is recorded on a PC.

2.3 Working principle of the Silicon Drift type Detector (SDD)

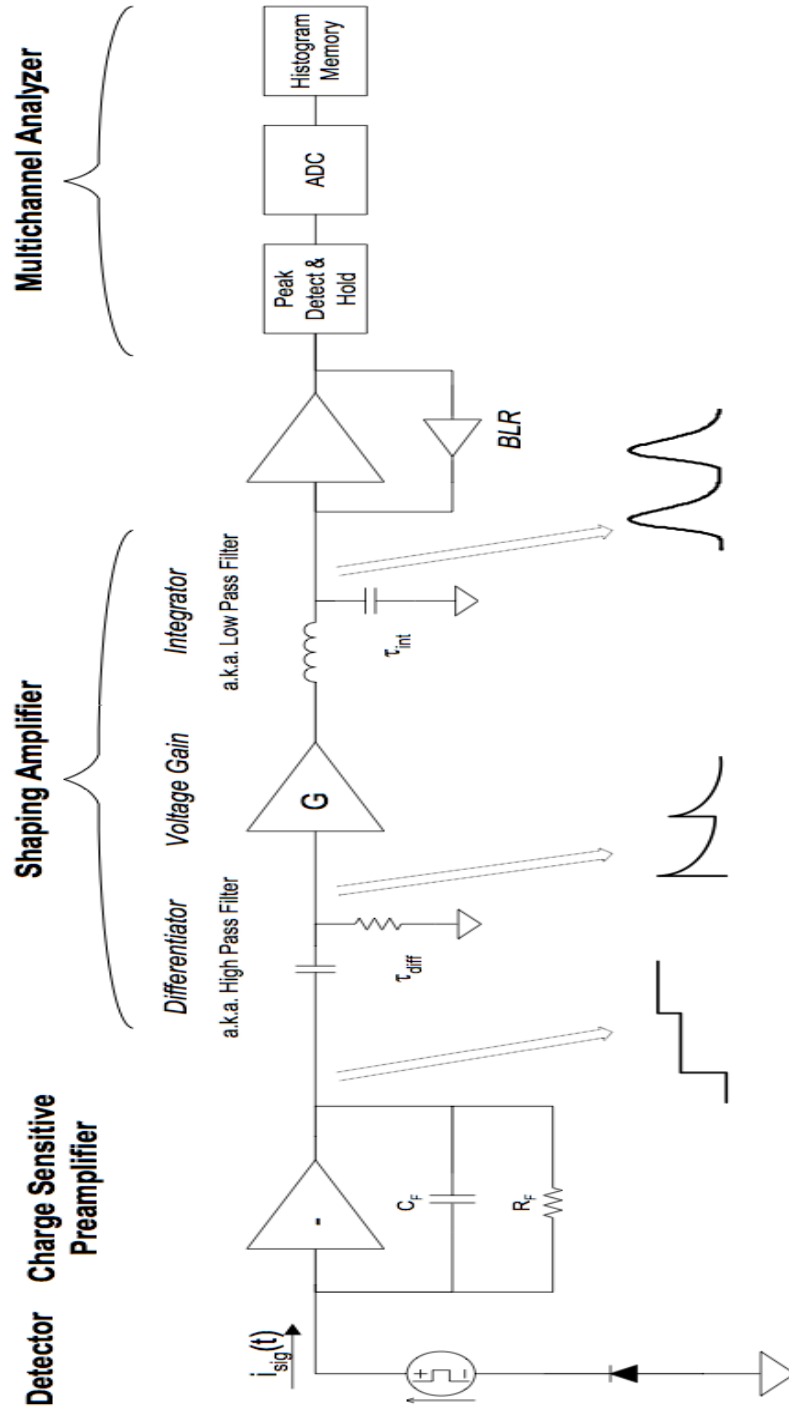


Figure 2.6: Different blocks involved in the X-ray spectroscopy, plus the schematic diagram of the signal processing electronic stages [80]. Four main block are, (i) Detector itself, (2) Preamplifier, (3) Shaper, and (4) MCA.

2. INSTRUMENTATION FOR THE SX AND HX DIAGNOSTICS

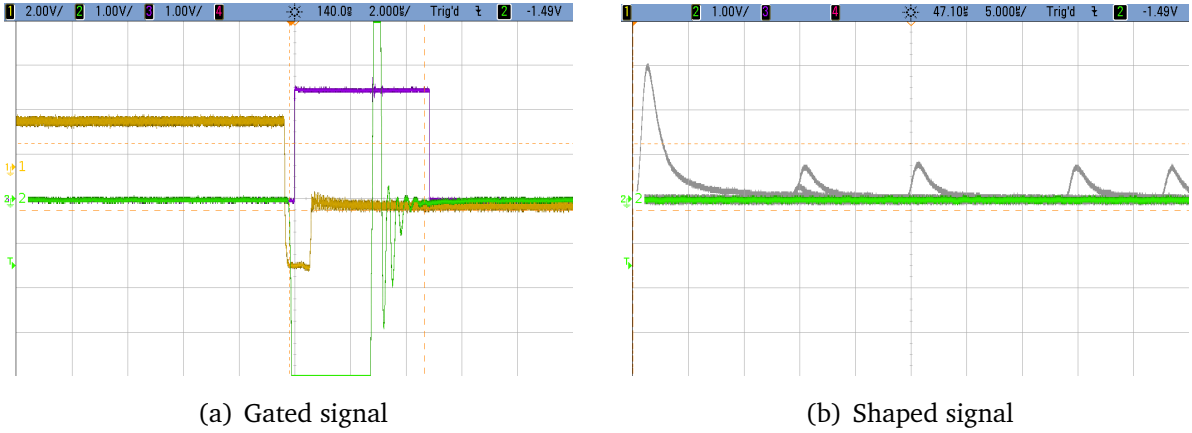


Figure 2.7: (a) A zoomed in oscilloscope trace during the reset (time step = $2\mu s$). The reset diode signal is shown in yellow, the shaped signal in green, and the gate signal in violet. (b) The shaper (i.e., integro-differentiator) output signal is shown in gray and the base line in green (time step = $5\mu s$). The gaussian-like signals (in gray) are obtained from the unshaped step-like signals.

2.3.5 Shaping amplifier

The output of the preamplifier, is fed to the pulse shaping amplifier (shaper). The absolute value of every voltage step is not important, instead only the ‘change in height’ from every step to the next is needed. The change in voltage step is obtained by differentiating the signal. Naively, it can be imagined that the integration of a bell-shaped gaussian function is a smooth step-like function (or error function). In a similar but opposite way, a differentiation of a smooth step-like signal is a bell-shaped gaussian signal. A combination of differentiator and integrator circuits is used to produce a desired pulse shape, which can be easily handled by the further Analog-to-digital convertor. The product of the effective resistor (R) and capacitor (C) values, originating from the effective integro-differentiator circuit, is termed as shaping time ($t = RC$). The width (in time) of the gaussian shaped pulses is controlled by the value of the shaping time (t).

The aim of the shaping amplifier is to create short time-width pulses such that it allows handling of high count rates. If the pulse is shaped before it reaches its maximum amplitude, then it might lead to incomplete charge collection and hence underestimation of the pulse height. At longer shaping times the noise on the base line is suppressed well. Choice of a shaping time is indeed a trade off between the count rate limit and the proper pulse shaping and noise level.

2.3 Working principle of the Silicon Drift type Detector (SDD)

Different shaper modules were tested and appropriate ones were selected for further use. The shaper allows the shaping times 0.25, 0.5, 1, 2, 3 and 6 μs for the purpose of fast as well as slow shaping. The shaper also provides the amplification factors of 5, 10, and 100. The voltage steps are scaled into the dynamic range of 0 - 10 V. Figure 2.7 (in gray) shows the typical shaped pulses seen on the oscilloscope, the base line is seen in green color.

2.3.5.1 Pole-zero and baseline restoration

In reality the preamplifier does not provide a perfect flat-top step function, but a slowly falling tail step-like function. When the step-like signal is passed through the integro-differentiator (or shaper circuit), it is seen that the tail of the shaped pulse is forced to fall below the baseline and rises up again. If a second pulse appears in this time interval, it can appear in this depressed baseline and may lead to a false measurement of its height. It is called as the pole-zero cancellation. The correction for this effect can be achieved by a potentiometer knob provided on the shaper. In effect, it is the fine tuning of the fall time of the differentiator.

2.3.6 Gate

The shaper output voltage, as a response to the reset pulse, jumps drastically from positive to negative extreme before finally settling down at baseline level. A gate circuit, introduced in between the shaper and MCA board, blocks the period every time when the reset occurs (see Figure 2.7), and avoids any spurious signals to be fed to the MCA. The width of the gate signal is set between 10-20 μsec .

2.3.7 Multi-Channel Analyser (MCA)

The shaper circuit converts step-like input signals into gaussian-like individual signals with amplitude ranging between 0 to 10 V. The shaped pulses have to be further sorted out as per their amplitudes. For this purpose, the shaped pulses are fed to the Multi-Channel Analyzer (MCA) board, see Figure A.1 in Appendix A. The MCA circuit discriminates the input pulses according to their heights and puts them into a corresponding digital bin, called as *channel*. Eventually, the energy of the incident photon is converted into a channel number; hence the name *pulse height analysis*. Further technical information can be found in the manual [81] and the Appendix A.

2. INSTRUMENTATION FOR THE SX AND HX DIAGNOSTICS

All incoming pulses are screened by a voltage window. At software level, two voltage levels are defined, (i) lower level discriminator (LLD), and (ii) upper level discriminator (ULD). Only those pulses falling in between the levels are accepted and processed, in order to avoid, (a) spurious small amplitude noise fluctuations sitting on the baseline, or (b) very high amplitude artifacts. The screen-shot of the MCA software control is shown in Figure A.2 in Appendix A.

A differential *pulse height spectrum*, i.e. number of pulses ΔN collected in a height interval ΔH , is obtained in the end,

$$f(H) = \frac{dN}{dH} \quad (2.5)$$

Using proper calibration, the $f(H)$ is then converted into a photon energy spectrum $f(E)$ and passed on for further analysis.

The MCA can be operated in *histogram* or *list* mode. In *histogram* mode, the spectrum can be accumulated over a defined time interval. Whereas in *list* mode, every photon event receives a *channel* as well as a *time* stamp. In this way operating the MCA in *list* mode offers much more freedom for the further analysis.

2.3.8 Energy calibration

The amount of charge generated by a photon interaction is directly proportional to the energy of the photon. The linear dependence of the above two quantities, is very crucial in the detector characterization. Linear performance of the pulse shaper/amplifier as well as MCA board is highly guaranteed. Each photon event in the end is stamped by the MCA channel number. The channel-energy relation is necessary to be obtained prior to the experiment. For this purpose a set of laboratory experiments performed are discussed in the next Chapter 3.

2.3.9 Energy resolution and noise

All the information about the photon interaction is in the total amount of charge collected and the way it is collected. Any fluctuation in the total number of charges collected, can cause a spread in the pulse height around a mean. As a result, the line emission is recorded broader than the intrinsic width of the line incident on the detector.

2.3 Working principle of the Silicon Drift type Detector (SDD)

The electronic transition energy between the inner shell energy levels are well described by Lorentzian function and have a very narrow spread. The width can be estimated by the uncertainty principle, $\Delta E \approx \hbar/\Delta\tau$, where $\Delta\tau$ being the electronic transition time scale i.e. of the order of 10^{-8} sec. Therefore, ΔE is $\sim 10^{-7}$ eV, which is extremely small as compared to 150 eV energy resolution of the typical X-ray spectroscopy using the semiconductor detectors. Hence, we simply neglect any contribution to the width of the line from natural width and collisional broadening etc.

The observed broad line width is a result of many components. Any variations in (a) the operating parameters (operating voltages) of the detector, (b) the electronic random noise (dark current from detector volume, preamp and other circuits) or (c) the statistical Poisson uncertainty inherent in the creation of electron-hole pair, can cause a change in the overall detector response.

2.3.9.1 The inherent Poisson noise

The first two components can be controlled by external means, but the third component, i.e., the Poisson uncertainty is inherent in the process of electron-hole pair creation, and cannot be avoided. In fact it is the dominant component in the total width of the line. We call it noise, because it degrades the resolution in the similar fashion as any other noise source in the system.

Let us estimate the contribution of the noise due to inherent Poisson statistics. Let N be the total amount of charge produced on an average, on every photon interaction. Since the generation of electron-hole pair by a photon interaction is a Poisson process, the inherent statistical fluctuation can be estimated as the standard deviation $\sigma_{Poisson} = \sqrt{N}$.

Let the average pulse amplitude (H_0) be represented in terms of the average total charge as, $H_0 = KN$, where K is a proportionality constant¹. Then, the standard deviation $\sigma_{Poisson}$ on H_0 can be written as, $\sigma_{Poisson} = K\sqrt{N}$. Therefore the resolution (FWHM/ H_0) will be

$$Resolution = 2.35 \times K \frac{\sqrt{N}}{KN} = 2.35 \frac{1}{\sqrt{N}}. \quad (2.6)$$

¹The linear proportionality is a very good assumption, it is also assured from the energy-channel calibration relation

2. INSTRUMENTATION FOR THE SX AND HX DIAGNOSTICS

The energy resolution (is equal to the pulse height resolution) is

$$\frac{\Delta E}{E} = \frac{2.35}{\sqrt{N}}. \quad (2.7)$$

We see that resolution is a very slowly varying function of N , and we, in practice, more or less touch a limiting value of the resolution.

All three quantities in the above equation are measurable (i.e., E , ΔE , and N). It is experimentally observed that the resolution can be a factor of 3 to 4 lower than the above predicted value. A factor, called Fano factor (F), is introduced in order to quantify the deviation of the observed variance in N from the pure Poisson statistics. The Fano energy resolution is given as [82]

$$Resolution = \frac{\Delta E}{E} = 2.35\sqrt{\frac{F}{N}}. \quad (2.8)$$

If ϵ is the energy required to create one electron-hole pair, then the total amount of charge (N) created by absorbing energy (E), is, $N = E/\epsilon$.

The above equation can be rearranged to obtain the energy resolution as a function of photon energy

$$\Delta E = 2.35\sqrt{F\epsilon E} \quad (2.9)$$

or the standard deviation

$$\sigma_{Poisson} = \sqrt{F\epsilon E} \quad (2.10)$$

The ϵ for Si is 3.65 eV/e-h pair, and for Ge it is 2.9 eV/e-h pair. note that ϵ is not the band gap, the band gap energy is much smaller than the ϵ . It is mainly due to the fact that, out of the photon energy deposited in the crystal, $\sim 2/3$ of the energy is used up in crystal lattice excitation ($\sim 2/3$) and the $\sim 1/3$ is utilized in generation of electron-hole charge pairs. The ratio is almost same for many semiconductor materials [83]. The Fano factor (F) is ≈ 0.11 for silicon at soft X-ray energies, but F is not a constant [84]. Using the value of $\epsilon=3.65$ eV/e-h pair and $F=0.11$ for Si, the Fano limited energy resolution at 5.9 keV is calculated to be equal to 115 eV. In most of the experiments the resolution is obtained in the range of 130-150 eV.

2.3 Working principle of the Silicon Drift type Detector (SDD)

2.3.9.2 Dependence on temperature

A detector made up of a lower band gap material (e.g., germanium) can offer better resolution due to the better Fano statistics (i.e. lower band gap means higher electron-hole pairs per given energy). However, low band gap material must be cooled to a lower temperature to suppress the thermal charge generation $\sim \exp(-\epsilon/kT)$.

Larger band gap also increases the thermally excited number of electrons in the conduction band at a given temperature (T) by a factor $\sim \exp(-\epsilon/kT)$. The low band gap material is required to be cooled down to lower temperatures, since the thermally excited electrons generate a current in the detector called as *dark current*. For a given temperature the creation of thermal charge is again a Poisson process and characterizes corresponding standard deviation $\sigma_{darkcurrent}$.

Due to the negative exponential dependence on the temperature, a slight decrease in temperature lowers the probability of the thermal excitation of the electrons. Moreover, silicon has a relatively higher band gap energy as compared to germanium. Hence, for the Silicon Drift Detector (SDD), Peltier cooling of up to -20 to -30 °C is sufficient. In fact, unlike the germanium detector, the SDD can also be operated at room temperature with relatively low dark current.

2.3.9.3 Dependence on the electronic noise

While handling of the detector signal at every electronic stage, some noise is added up in the signal. The noise added in the signal during the most early stages keeps on amplified during all later stages. For this purpose, the SDD has a JFET integrated within the detector which also gives a first stage amplification (even prior to the preamplifier stage), as already discussed in Section 2.3.1. The cumulative contribution to the noise from all electronic components, is again a random process and can be denoted as standard deviation $\sigma_{electronics}$.

2.3.9.4 Total resolution

Since all the processes described above are independent processes, the total noise standard deviation (σ) can be written as a quadrature sum of all these components.

$$\sigma_{total}^2 = \sigma_{Poisson}^2 + \sigma_{dark\ current}^2 + \sigma_{electronic}^2 + \dots \quad (2.11)$$

2. INSTRUMENTATION FOR THE SX AND HX DIAGNOSTICS

The resolution (δE) scales as the square root of the energy. However, if the electronic noise is dominant, the resolution-energy relation can deviate from the square-root shape to a straight line shape. See Section 3.4.2 for the experimental calibration of the resolution. In detectors having a large energy range, a n^{th} -degree polynomial is also used to best represent the resolution-energy relation [53]. It is very crucial to know how the energy resolution changes with temperature. For this purpose the experiments were carried out in the test laboratory, discussed in the next Chapter 3.

2.3.10 Efficiency of the SDD

The SDD, being just a thin silicon wafer, starts becoming transparent to more and more energetic X-rays. Typically up to 20 keV photons are detected with 30% probability. A thin Be-filter foil associated with the SDD, cuts all the photons below ~ 800 eV. More discussion is carried out in next Chapter 3 on setting up the diagnostics.

2.4 Working principle of SDD with Scintillator CsI(Tl)

In this section we will discuss the detector used for detection of the hard X-rays (i.e., photons beyond 20 keV). For this purpose, the SDD was used in combination with the scintillator CsI(Tl) i.e. a Caesium iodide crystal doped with the activator material thallium (effective atomic number 54).

Scintillator(s) + photo-multiplier tube (PMT) combination had been the standard detectors in the field of γ -ray spectroscopy for many decades [53], until the promising semiconductor detectors started replacing the cumbersome and inconvenient PMT technology. Since the SDD, a 450 μm thin silicon wafer, is essentially transparent to the high energies, it requires to be coupled with a dense scintillator material which is capable of stopping high energy photons. As a result the question that arises is, which scintillators would suit in combination with the silicon based semiconductor detectors? Among all scintillators, CsI(Tl) is currently the best scintillator coupled with a silicon based detector for the reasons discussed in the next two Sections.

2.4.1 The scintillator active volume

As discussed earlier in Section 2.3, on SDD, the concept that the X-rays, on interaction with the detector material, lose their energy by creating a number of electron-hole

2.4 Working principle of SDD with Scintillator CsI(Tl)

pairs and the detector then collects the electrons to produce a signal. The detection process using the scintillator is also similar to that of solid state detectors. As discussed in the Section 2.2, on Photoelectric effect, the stopping power of the material is strongly proportional to the density of the material. Usually scintillator materials are high density materials designed in such a way that they can stop photons with energy up to several keV or MeV.

The CsI crystal possesses conduction band and valance band separated by roughly the energy equivalent to an optical or UV photon. An activator atom, a fraction of 1 in 1000, creates a defect lattice site and gives rise to extra energy levels between the conduction and valance band, closer to the conduction band. A photon may interact with the scintillator material in various different ways mentioned in the Section 2.2 on matter radiation interaction. The energy deposited by the photon is shared among a number of electron-holes set free in the conduction and valance band of the scintillator crystal. The holes readily move to the activator sites and the electrons in the processes of de-excitation produce optical photons.

2.4.2 Coupling with the SDD

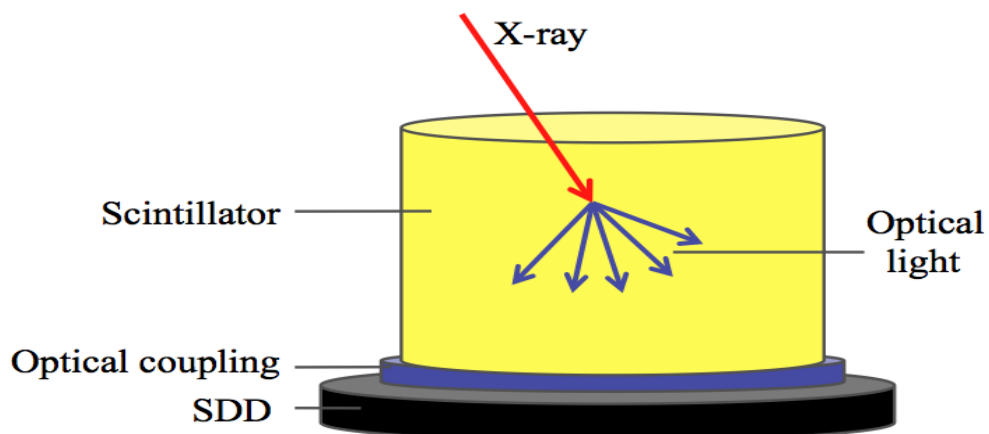


Figure 2.8: The scintillator shown in yellow color is kept on top of the SDD (in gray), with a silicon pad in between them.

2. INSTRUMENTATION FOR THE SX AND HX DIAGNOSTICS

Usually the scintillator is coupled to a device which can then detect this optical light and produce an electrical signal. A photo-multiplier tube (PMT) is a most common choice in the γ -ray spectroscopy. In our studies, we coupled the scintillator to the SDD similar to the one mentioned in the previous sections. A cartoon is shown in Figure 2.8. Every optical photon emitted by the scintillator is then intercepted inside the SDD depleted volume, and creates a number of electron-hole pairs forming the electric signal. The later process is exactly similar to the pure SDD operation previously discussed.

The use of SDD is advantageous over the photo-multiplier tube (PMT) in many respects. Usually, a PMT needs a very high voltage power supply, and is also very sensitive to the magnetic field. This requires careful shielding and the setup can be bulky. A SDD technique on the other hand solves most of these problems. The CsI(Tl) scintillator emits the optical light spectrum which matches optimally with the quantum efficiency of the SDD. It should be noted that the choice of the scintillator material (CsI(Tl)) is not made by comparing or studying the performance of various scintillators; this is completely beyond the scope of this thesis. Instead, the CsI(Tl) was chosen, since it is the only scintillator with its emission spectra matching with the quantum efficiency of the SDD [60]. Figure 2.9 shows emission spectrum of CsI(Tl) and the quantum efficiency of the SDD [85; 86; 87]. A comparison between the properties of CsI(Tl) and some selected popular scintillators can be seen in Table 2.1 adopted from two classic books, one by Knoll [53], and second by Gilmore & Hemingway [64].

It can be seen that there are some advantages as well as some disadvantages in selecting the CsI(Tl) crystal among other. For example, CsI(Tl) does not scintillate not fast enough as compared to just the CsI crystal or NaI(Tl) crystal, but it has not only the maximum light yield per γ -ray but also the peak wavelength is such that it exactly matches with the efficiency of the SDD [85].

2.4.3 Physical properties of the scintillator

The CsI is slightly denser than the NaI and hence has a greater absorption coefficient. It is less hygroscopic (i.e., less able to adhere water molecules to it), it is less brittle and hence more resistant to mechanical shocks. This makes it more compatible for the space based instruments as well as harsh environments such as in tokamaks.

2.4 Working principle of SDD with Scintillator CsI(Tl)

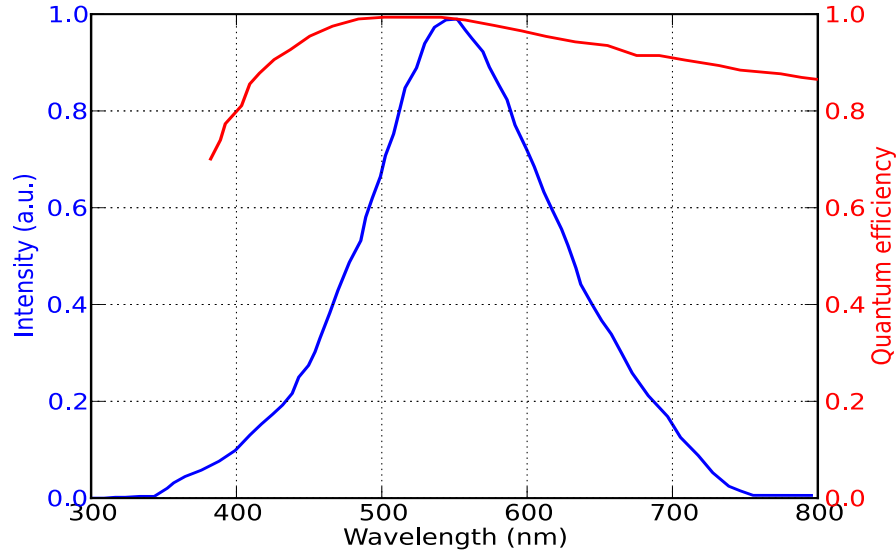


Figure 2.9: The gaussian-like optical emission spectrum (blue curve) of CsI(Tl) matches very well with the SDD quantum efficiency (red curve) for the optical light [85].

The CsI(Tl) crystal is very small cylindrical in size, with the height of 5 mm and the diameter of 5 mm, matching with the SDD diameter (6.2 mm).

2.4.4 Light yield and temperature dependence

Figure 2.10 shows the temperature characteristics of the CsI(Tl) by Saint-Gobain crystals [88]. The optical light emitted by the scintillator depends on the initial occupancy of the electrons in the raised energy level. The light output of the scintillator is hence easily altered by the temperature of the crystal. In fact it is seen that the light output is maximum near the room temperature and decreases on either sides. The detailed temperature dependence using the scintillation model is studied by Valentine et. al. [89].

2.4.5 Energy calibration

The total number of optical photons emitted by the scintillator is eventually translated into the deposited photon energy. One more parameter is now added in the energy calibration vis., which is the temperature of the CsI(Tl) crystal. It is important to note that the thermo-electric cooling is applied to the SDD and not to the

2. INSTRUMENTATION FOR THE SX AND HX DIAGNOSTICS

Table 2.1: Comparison of the properties of various scintillators [53; 64].

Scintillator	Activ.	Abbrev.	Density (g.cm ⁻³)	peak λ (nm)	Decay T. (ns)	Yield ph./MeV
Caesium iodide	Tl	CsI(Tl)	4.51	550	1000	65000
	Na	CsI(Na)	4.51	420	630	39000
	-	CsI	4.51	315	16	2000
Sodium iodide	Tl	NaI(Tl)	3.67	415	230	38000
Barium fluoride	-	BaF2	4.88	310	630	1400
Bismuth germanate	-	BGO	7.13	480	300	8200

scintillator crystal. Since the crystal is a relatively huge volume (100 mm³) with respect to the SDD (13 mm³), and the crystal is coupled to the SDD through an optically transparent silicon-pad (with bad thermal conductivity), controlling the temperature of the crystal is practically difficult. This is systematically circumvented in the measurements, since the detector-crystal configuration is kept under fixed conditions, similar to those used in the calibration tests.

2.4.6 Efficiency of the CsI(Tl)

The efficiency of the scintillator crystal is the probability of stopping a photon of certain energy E . The CsI(Tl) crystal, with the effective atomic number 54, is dense enough to stop photons from 1 keV up to 1 MeV, with the probability smoothly decreasing from 100% to 10% respectively. Usually the lower limit is set by an absorption-filter installed in front of the scintillator. More details are discussed in the Chapter 3.

In the next chapter we will discuss the actual establishment and constant improvement of the diagnostics, through the process of trial and error experimentation

2.4 Working principle of SDD with Scintillator CsI(Tl)

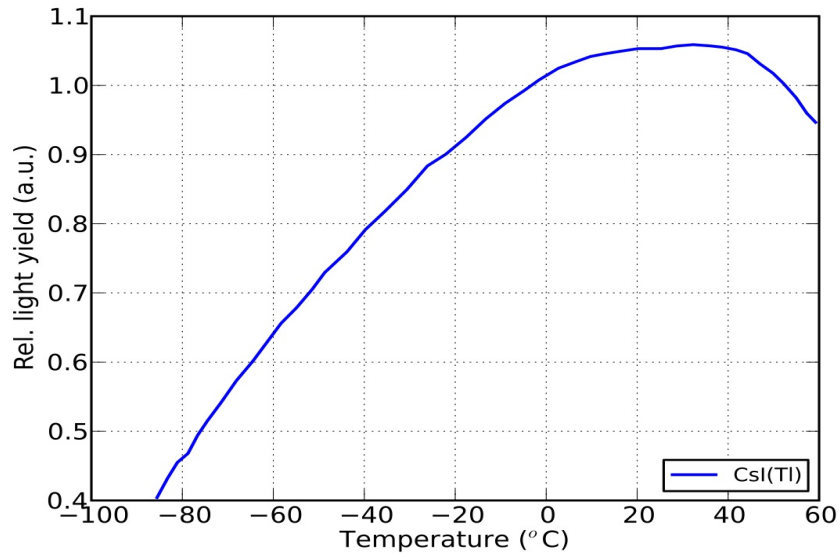


Figure 2.10: The CsI(Tl) shows maximum light yield around room temperature. [88]

and a numerous practical issues, finally leading us to the state of the art hard X-ray measurement diagnostics.

2. INSTRUMENTATION FOR THE SX AND HX DIAGNOSTICS

“Do not look into laser with remaining good eye.”

- My lab engineer^a

^aOriginal reference - [90]

3

Setting up the SX and HX diagnostics

3.1 Introduction

In this chapter we will discuss the characteristics of the diagnostics as a whole, and preparation for the actual plasma emission measurements and experiments. Before the plasma measurements were carried out, we performed several laboratory tests and characterization measurements. This chapter covers the detailed characterization studies relating to the SDD and SDD+CsI(Tl). Even though the SDD and the further processing underlying both soft and hard X-ray detectors is exactly the same, the presence of the scintillator in hard X-ray detector changes the overall response of the detector completely.

From here on, whenever we mention about hard X-ray detector or diagnostics or hard X-ray pulse height analysis (HXR-PHA), we are referring to the SDD+CsI(Tl) combination. Similarly, when we are mentioning about soft X-ray detector or diagnostics or soft X-ray pulse height analysis (SXR-PHA), we are referring only to the SDD detector.

3.2 Setting up the experiments

In the previous Chapter 2 we saw the different blocks involved in the diagnostics, such as, detector, preamplifier, shaper, MCA and a PC interface (see Figure 2.6). Here we will elaborate the first block, the *detector surrounding*. The detector is usually mounted in a vessel which is maintained at moderate vacuum. Also the view of the detector is controlled with the help of metallic pinholes. Along with the pinholes, various metallic foils are installed in front of the detector to filter out some of the lower energies. All these components together make up the diagnostics. We carried out several experiments for different aims, such as, (i) the usual calibration experiments in the laboratory, (ii) experiment on the WEGA stellarator, (iii) experiment on the Particle Induced Gamma Emission (PIGE) or Particle Induced X-ray Emission (PIXE), and finally to achieve the main goal of the thesis, (iv) the experiment on the tokamak plasma at ASDEX Upgrade.

The diagnostics setup was modified a little bit depending on which experiment was done.

We performed the upgrades in the setup via trial and error. Although this way is time consuming, we did not have any alternative as this type of detectors were not previously used in tokamak environment.

It is also worthwhile to mention that we spent lot of time in designing the diagnostics because, from both hardware and software point of view, it was started from scratch! The detectors specially ordered from the MPI-HLL and PNSensor GmbH, were not always available on stock every time we needed to replace them when they were damaged during the experiments. Moreover, the special Be-filters and windows (also an essential part of the setup) had to be ordered from USA. Since the parts were specifically designed for our setup and standards at ASDEX Upgrade, it took almost 1 year to receive these parts.

We will first discuss the basic setup constructed and then later we will describe the necessary changes made for each experiment done.

3.2.1 Detector vessel

The SDD, when cooled below 0°C, has to be protected from water vapor condensation on the surface. The water vapors can also cause rusting of the extremely tiny bridging wires on the surface of the detector. For this reason the detector vessel is always

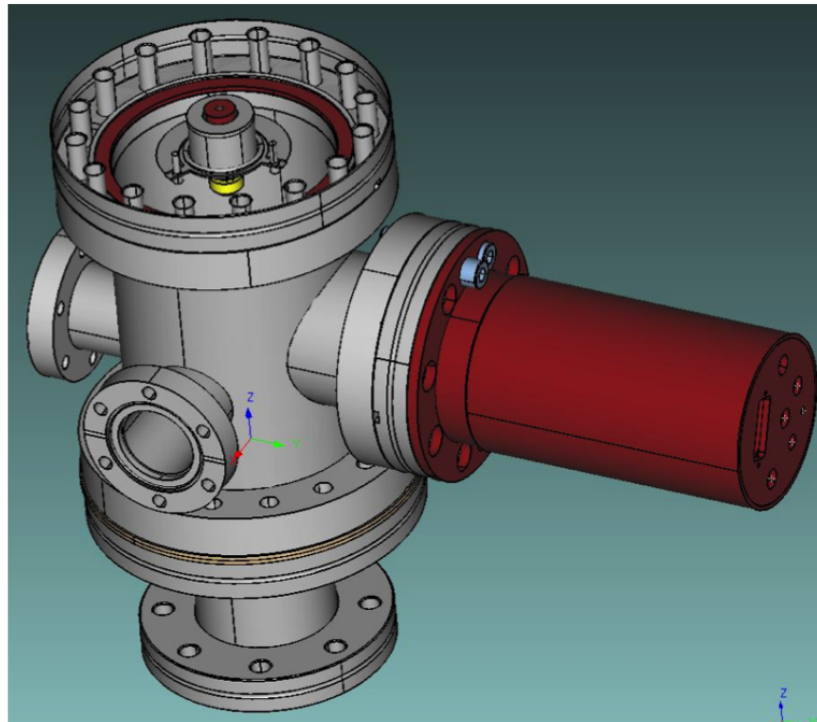


Figure 3.1: The schematic of the steel vessel containing the detector. The detector (yellow) looks vertically downward towards the plasma. The flange at the bottom is mounted on the (tokamak) plasma vessel through a shutter in between. The red cylinder at the right is the copper container to shield the preamplifier electronics mounted inside it. The port on the left is for mounting the vacuum pump. Each port - for the electronics, vacuum, plasma side, and the detector flange, is electrically disconnected with each other with the insertion of ceramic disks and washers.

vented with nitrogen after every vessel opening and to keep the air within the vessel dry enough. The SDD is operated at pre-vacuum conditions, usually less than 1 mbar is sufficient. The detector vessel also serves many other purposes as described below.

The vessel was designed and constructed in the workshop at ASDEX Upgrade. The steel vessel is cylindrical in shape, approximately 30 cm in height and is easily movable from test laboratory to the tokamak hall. A schematic diagram of the detector vessel is shown in Figure 3.1 and 3.2.

The actual photograph of the detector vessel is shown in Figure 3.3.

The vessel has three ports. A vacuum pump is mounted on one port, and the detector electronics is mounted on the second port. The third port, initially designed for vacuum monitoring, is kept sealed. The vacuum is monitored electronically by the inbuilt gauge on the pump itself. A special flange is used, having a D-sub connector

3. SETTING UP THE SX AND HX DIAGNOSTICS

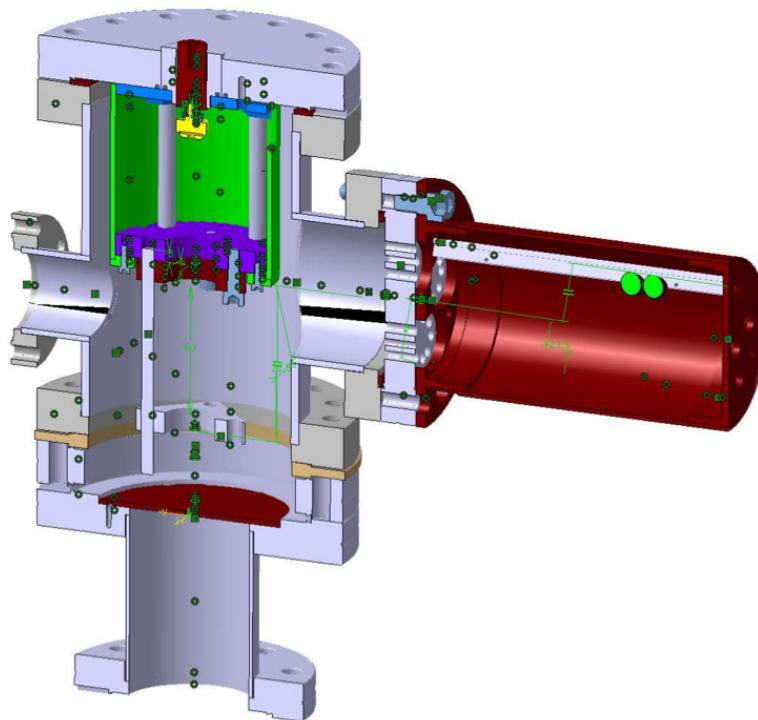


Figure 3.2: The schematic cross-section of the detector vessel. On the top, the detector (in yellow) mounted on the small heat carrying copper holder (red), sealed on a steel flange. The optical light-proof detector housing is shown in green. The detector view is controlled by the pinholes and filters to be mounted on the downward side of the housing.

soldered into it for the wires to feed through the atmosphere side into the vacuum side. The electronics is covered by a copper cylinder, to serve the purpose of shielding from the spurious electro-magnetic fields inside the noisy tokamak hall.

The detector is mounted on the steel flange CF-100. The flange has a small hole at the center and a small copper cylinder was welded through it (yellow block at the top in Figure 3.2). The the SDD is screwed on this copper cylinder, in order to conduct away the detector body heat, i.e. the heat from the Peltier cooler element.

During the experimentation it was noticed that there was some optical light leaking in the vessel especially from the ceramic adaptors, detector base etc. Too much optical light leaking in the vessel and reaching the detector from the rear side

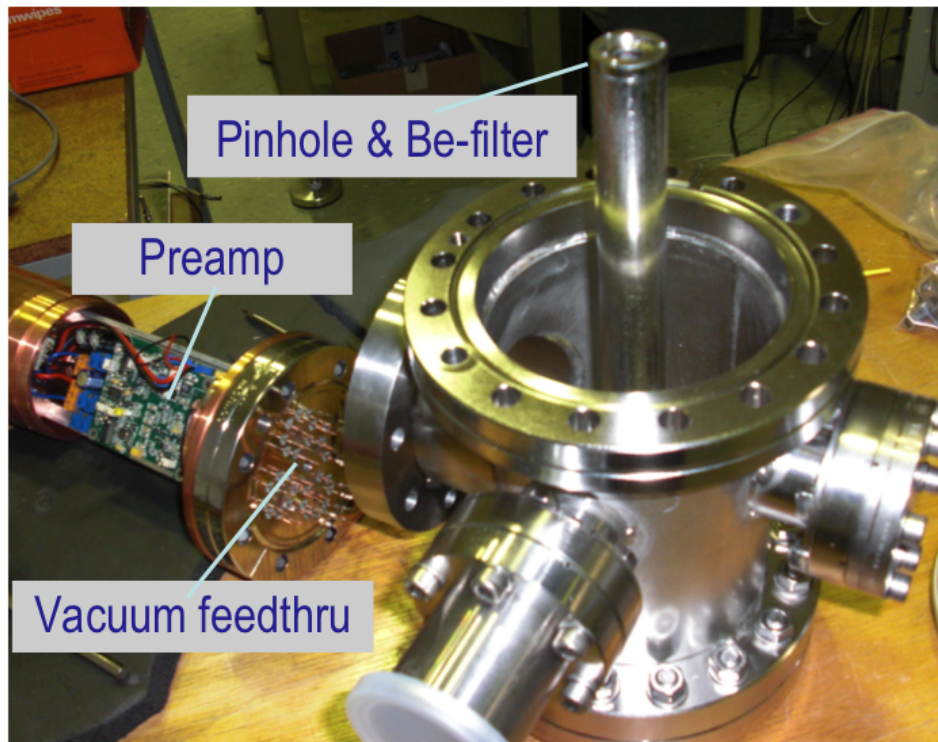


Figure 3.3: The actual photograph of the detector vessel (rotated 180° sideways as compared to the schematic view in Figure 3.1). On the left side is the preamplifier electronics connected via vacuum feed-through cables.

(i.e. through the detector pin-connections), can flood the detector with background events and seriously affect the total count rate handled. From the front side it is not a problem since there exists a protective layer of Beryllium. To avoid that problem a special aluminum housing was later designed, fixed on top of the detector, on the same flange, shown in Figure 3.5.

The housing was specially designed in such a way that the volume inside the housing still gets pumped while no light can leak inside. Every component of the housing was colored black such that it absorbs an optical photon incident if any. The coloring was also done such that neither does it start losing any pigments under vacuum conditions nor while cleaning with isopropanol or other recommended cleansing. It was then tested to make sure that absolutely no optical light leaked in the vessel and reached the detector. Later it was experienced that the housing needed to be grounded properly avoiding any capacitive contact with the flange, since it is mounted on the same flange as that of the detector. Necessary modifications were done.

3. SETTING UP THE SX AND HX DIAGNOSTICS

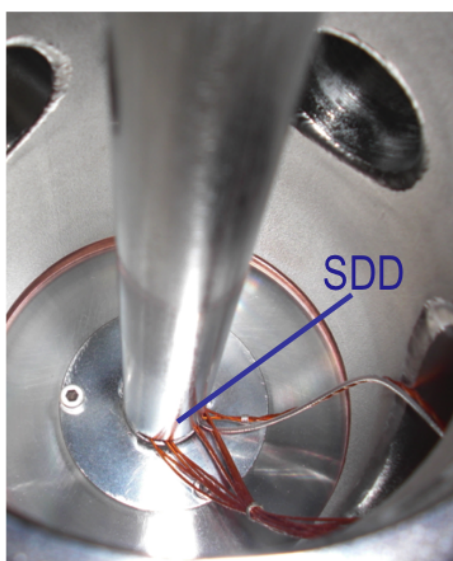


Figure 3.4: The old concept of housing the detector. The steel pipe act as a collimator as well as a holder for the pinhole and Be-filter. It was also implemented during the initial experiments on WEGA.

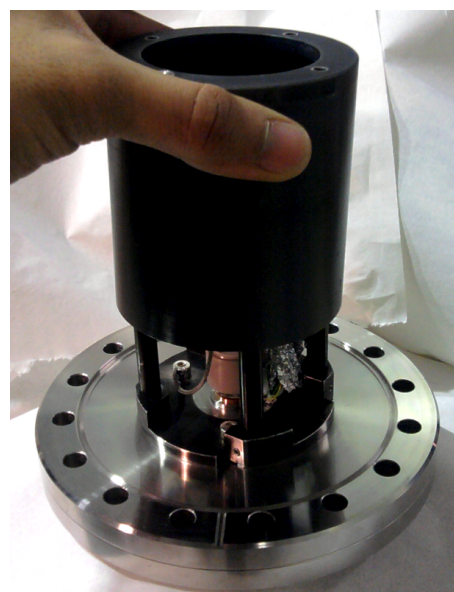


Figure 3.5: The new housing is completely light proof and more robust. It was implemented during the late 2011 and whole 2012 ASDEX Upgrade campaign.

The vessel is then mounted on the plasma torus vessel port with suitable adaptor or reduction flange. The adaptor flange is coupled to the detector vessel through a 2 mm thick ceramic disk, in order to electrically insulate it from the vessel on the other side. In similar way the vacuum pump is connected through a ceramic connector in between.

3.2.2 Viewing geometry : Pinholes & filters

In principle the detector, being a single pixel, can view the whole front hemisphere of a solid angle π . The viewing cone is restricted by installing one (or more) metallic pinhole in front of it at a distance d , as shown in Figure 3.6, defining the viewing cone. The pinhole helps in controlling the flux of photons incident on the detector from the plasma and at the same time defining the line of sight.

It can be shown that the viewing solid angle effectively depends only on three factors, (i) the area of the detector, (ii) the area of the pinhole, and (iii) the distance between the two; it does *not* depend on the distance of the detector itself from the plasma center.

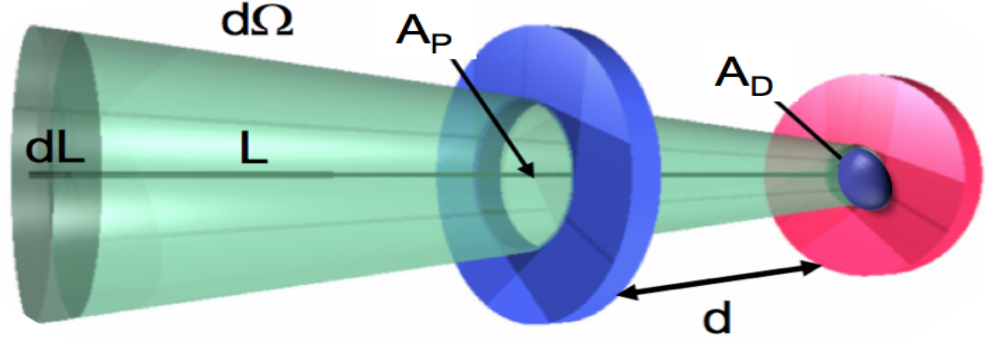


Figure 3.6: The etendue represents the effective solid angle the detector is looking through (image courtesy of A. Weller, IPP, Garching).

Under these conditions, the radiation power radiated by the plasma within the viewing geometry on to the detector can be estimated by evaluating the geometric factor called etendue (ϵ) and is given by

$$etendue = \frac{A_D \cdot A_P}{d^2} \dots (cm^2 \cdot sr.) \quad (3.1)$$

This relation is perfectly valid in all our setups. The detectors (e.g. bolometric detectors) sitting close to the plasma do not follow above simplified relation and a more rigorous derivation is required. A general treatment of the calculation of the etendue is shown by the authors in [91] and a numerical estimation is obtained by the author in [92] (*Appendix-E* in it).

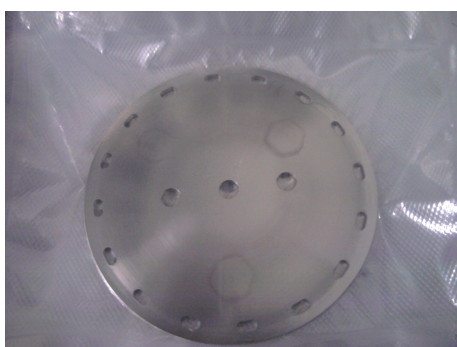
Different metal foils (Al, Be) of different thicknesses were used in order to create a proper low energy cut out. The exact pinholes and filters used in different experiments are mentioned in the respective descriptions. The pinholes and filters constructed and implemented are listed in Table 3.1.

For the soft X-ray, the filters were demanded such that the lower energy cut off can be up to 1 keV. On the base of the transmission curves presented in Section 3.3.1, we adopted a very thin ($\sim 15 \mu m$) Be-filter. It is extremely challenging to obtain a filter foil of thickness below $20 \mu m$ mainly due to three reasons, (a) the filter foil should be

3. SETTING UP THE SX AND HX DIAGNOSTICS

Table 3.1: Pinholes and filters obtained for the specific experiments.

Measurement	type	Material	Diameter	thickness
Soft X-ray	pinhole	Steel	5 mm	2 mm
		Steel	10 μm	1 mm
	Filters	Be	10 mm	30 μm
		Be	10 mm	50 μm
Hard X-ray	pinhole	Lead	2 mm	5 mm
		Lead	4 mm	5 mm
	filters	Be	10 mm	20 μm
		Al	10 mm	0.3 mm



(a) Be window



(b) filter holders

Figure 3.7: (a) The vacuum window with 3 allowed lines of sight, (b) the customized filter holders.

completely free of any micro-pinholes (which leaks optical light), (b) being very thin the foil should still withstand the pressure difference between air and vacuum side, (c) the glue holding the metallic foil on to the steel holder should be stable under vacuum conditions as well as moderately high temperatures.

In order to achieve this, we decided to have two structures,

- a steel window (100 mm diameter) with a hole (of 10mm diameter) covered with Be-foil, which solves the purpose of separating the vacuum side (tokamak) from the pre-vacuum side (detector vessel), see Figure 3.7a,
- the actual filter holder plates (10 mm diameter) holding foils of different thick-

ness, see Figure 3.7b.

In fact going one step further, the window is designed with three holes allowing three different viewing sights, for a 3-detector assembly planned in the future.

The window and filters, customized for our demands were manufactured and provided by the company Lebow Inc., USA [93]. A very sophisticated test setup was constructed in order to ensure the vacuum tightness of the window. The window was again tested in the IPP helium leak test facility, before it was installed at the given port on ASDEX Upgrade tokamak. It took one year to completely obtain the parts.

3.2.3 Detector operating voltages

The preamplifier circuit board also controls the voltage supply to the detector. The operating voltages are very crucial in optimizing the performance of the detector. The detector electronics is operated at settings shown in Table 3.2.

Table 3.2: SDD operating voltages

	Voltage (V)
Ring-1	-10
Ring-X	-125
Back contact	-75
Inner guard	-12
Reset diode	-15
Back guard	-
Drain	12
Temp. diode	-
Peltier (+ive)	7
Peltier (-ive)	-7
Peltier current	0.4A

3.2.4 Shaper

For the soft X-ray measurement a fast shaping time is required, whereas for the hard X-ray measurement a slow shaping time is necessary to match the scintillation time.

3. SETTING UP THE SX AND HX DIAGNOSTICS

Different shaper modules were tested and appropriate ones were selected for further use. The shaper used was ORTEC, model 452. The shaper allows the shaping times 0.25, 0.5, 1, 2, 3 and 6 μs for the purpose of fast as well as slow shaping. The shaper also provides the amplification gain factors of 5, 10, and 100. The shaping time of 1 μs and amplification gain of 10 was chosen for most of the hard X-ray measurements, such that the energy range of roughly 1 - 1000 keV was spanned over 8192 channels of the MCA. It was also confirmed by test measurements in the lab. The shaping time of 0.25 μs and amplification gain of 100 was chosen for most of the soft X-ray measurements. The MCA channel gain was kept fixed at 8192 channels during all the experiments.

3.2.5 Improved grounding scheme

Every unit in the detector assembly was connected in a fashion such that no common grounding was established between any two unwanted sources. For example, the detector vessel mounted on the tokamak port, was kept completely isolated from any other neighboring metallic components. The detector vessel was isolated from its own vacuum pump connectors with the help of ceramic flanges. The detector housing was properly grounded. The detector ground itself was kept separate and clean from the rest of the assembly.

A special 50 Ω LEMO co-axial signal cable and proper connectors were carefully chosen such that they do not pick up any spurious noise. Also throughout the signal line, from preamp to the PC-input, it was made sure that the impedance was 50 Ω , same as the impedance of the signal cable, such that no unwanted signal reflections could occur.

The signal cable was connected through a special LEMO adapter on the preamp side in order to suppress the noise picked up by the cable. But during later experimentation it was found that the adapter itself was responsible for picking up some noise. The connector is shown in Figure 3.8. It took a long time to realize this behavior since the adapter used perfectly solved the purpose in laboratory experiments, but as soon as the setup was taken to the tokamak environment, suddenly a change in noise behavior was noticed (see Figure 3.9). As the tokamak environment is always humongously noisy, it is extremely difficult to pin point the source or cause of noise.

The adapter works in a way that it separates out the grounding-shield of the cable from the preamp housing. It was then understood that the grounding-shield of the



Figure 3.8: The noise proof LEMO adapter found to be responsible for picking up noise in tokamak environment.

cable being disconnected, would act as a long antenna and would pick up noise even strongly in tokamak environments. A drastic improvement was noticed by removing the adapter.

3.3 Characterization of SXR-PHA

In this section, we will describe the characterization of the detector efficiency, the necessary calibration relations, the resolution and resolution dependence on various factors, and construction of the response function of the detector. The characterization experiments were usually carried out in the test laboratory, with the help of artificial X-ray radiation sources, as radio-active sources having a transition line in the range of 1-20 keV. The SDD used for all the soft X-ray measurements was of 10 mm² area, unlike the SDD used in hard X-ray measurements which was 30 mm² area. The thickness of both the detectors is same, i.e., 450 μm. Both the detectors are exactly the same in every respect except the area.

3.3.1 Efficiency

The absolute quantum efficiency is the ratio of the amount of radiation energy collected by the detector volume over the energy incident. It is quite obvious that

3. SETTING UP THE SX AND HX DIAGNOSTICS

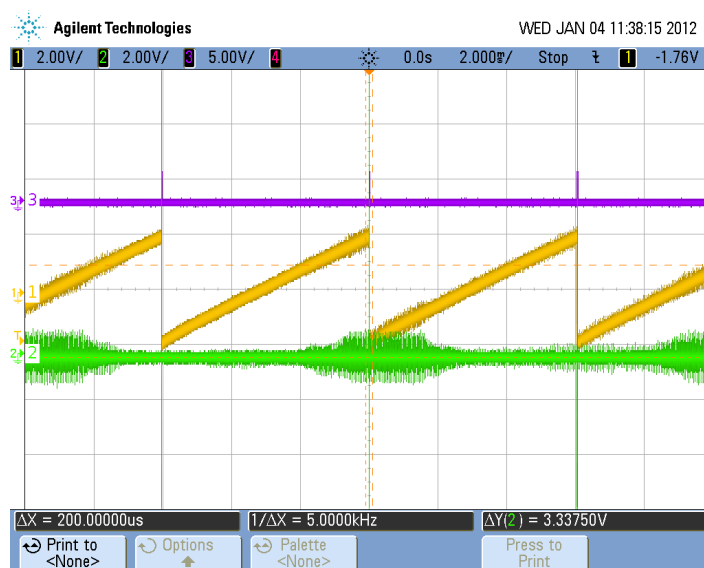


Figure 3.9: The oscilloscope trace showing the noise behavior caused by the LEMO adapter. The preamp (unshaped) signal is shown in yellow and the shaper output signal is shown in green. Both yellow and green curve shows the high frequency noise component sitting on top of the signal.

the quantum efficiency is a function of energy. In order to measure the exact efficiency curve of the detector, one should have a monochromatic radiation source with varying energy over the whole energy range of interest. This can be done at a synchrotron facility or a particle accelerator facility, such as Particle Induced X-ray Emission (PIXE). Alternatively, there exist well tested and robust numerical estimation techniques, providing a close estimate of the efficiency by computing the cross-section for different radiation-matter interaction processes (discussed in Chapter 2) within the type of detector material and its size. We obtained the efficiency estimate by using the tool provided by NIST, X-ray matter interaction cross-section data [66].

Figure 3.10 shows the efficiency of the silicon volume with thickness of 300, 450, 600 and 900 μm of silicon. Similar to the SDD efficiency estimate, the transmission curves for different filters were also obtained as shown in Figure 3.11. It is evident that the Al-filters offer a much harsher lower cutoff than the equal thickness Be-filters. The Al transmission curve corresponding to 10 μm shows a distinct spike feature at lower energy, it is due to the discrete inner-shell electrons photo-absorption processes.

The combination of the silicon absorption efficiency and the filter transmissions defines the total effective efficiency, shown in the Figure 3.12. The SDD has inher-

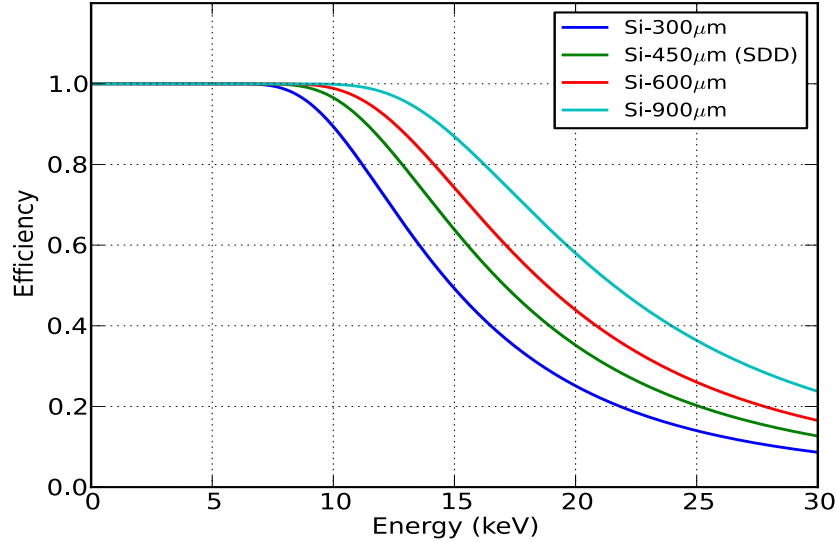


Figure 3.10: The X-ray absorption efficiency for different Silicon thicknesses. The SDD is 450 μm thick (shown in green).

ently, a 30 nm protective layer of Aluminum and a Beryllium filter of 11 μm on top of it, causing the low energy cut of near 1 keV. The blue curve in the Figure 3.12 shows the corresponding actual efficiency curve.

3.3.2 Energy calibration and resolution

The channel-energy calibration depends on various factors like (a) temperature of the diode, (b) amplification gain, (c) shaping time, (d) shaper module used and so on. In the end, the final experimental results have to be free of any such dependence. Hence it is made sure that these parameters are kept constant (or less fluctuate) over the course of the whole experimental campaign.

To obtain a proper channel-energy relation, we used two radioactive sources, Fe-55 and Am-241. The X-ray lines emitted are shown in the Table 3.3. The Fe-55 decays into Mn-55 via electron capture, in the process two characteristic X-rays Mn K_α and K_β are emitted.

The SDD shows quite a remarkable linear relationship between the incident photon energy and corresponding pulse height amplitude (or channel) measured. Figure 3.13 shows the channel-energy relation characterized for the SDD at a temperature

3. SETTING UP THE SX AND HX DIAGNOSTICS

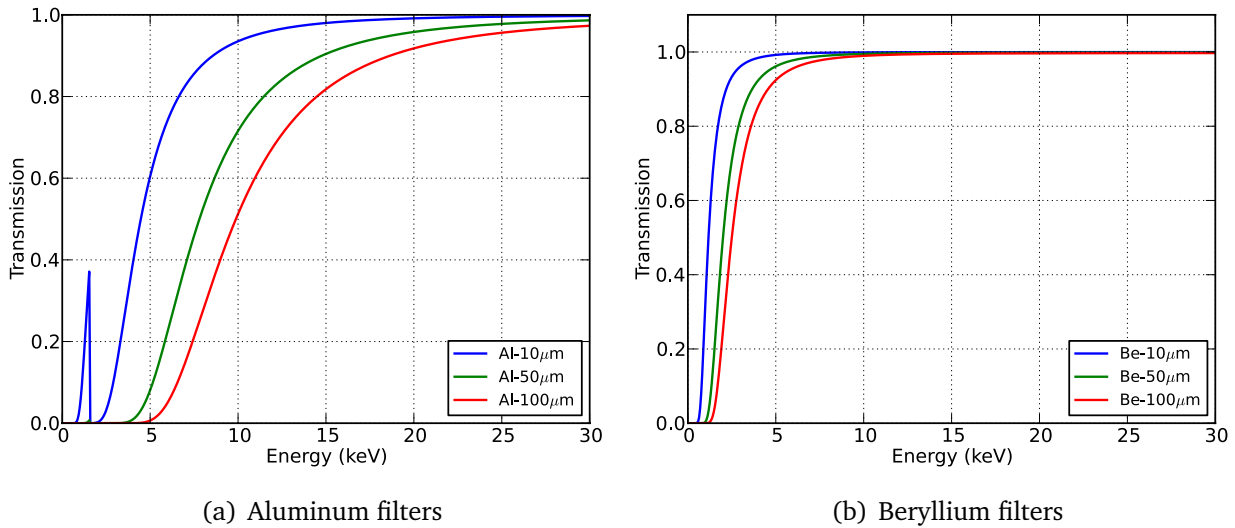


Figure 3.11: Transmission curves for different metallic filters

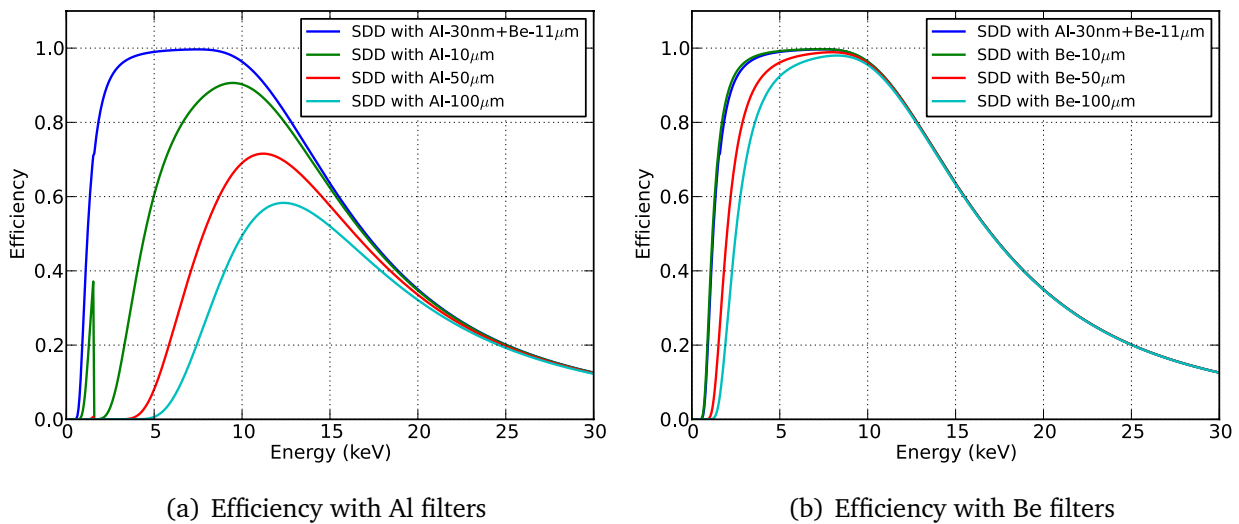


Figure 3.12: Combined efficiency curves for the SDD with different Al and Be filters.

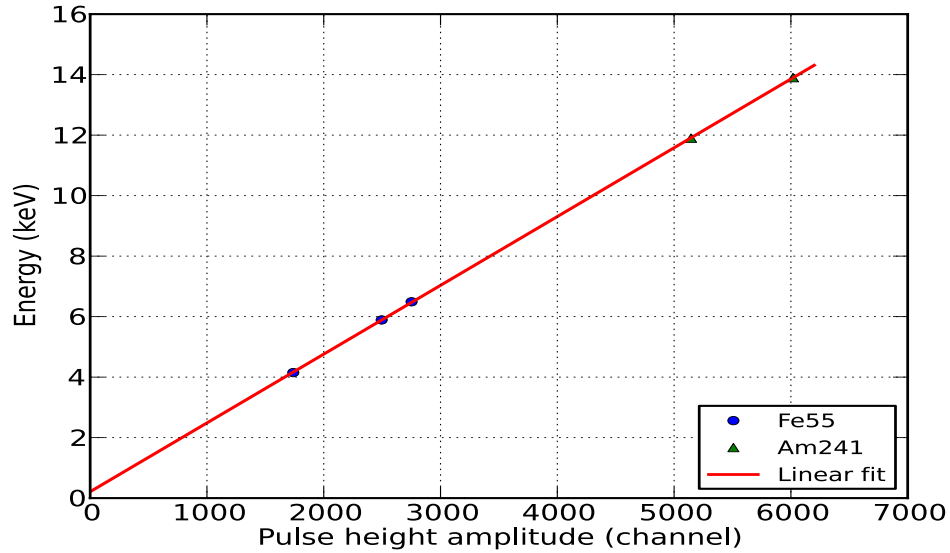


Figure 3.13: Photon energy to pulse height amplitude (channel) relation.

-25 C, corresponding to a temperature-diode voltage 5.89 V, with shaping time of 250 ns, and shaper coarse gain (cg) 20.

Similar calibration relation is obtained before every experiment and it was observed that the relation remains constant over the experimental time.

The SDD provides the energy resolution of $\sim 2\%$ at 5.9 keV energy. The energy resolution is shown in the Figure 3.14

3.3.2.1 Effect of radiation damage

The SDD is known for its high purity and quality of the silicon wafer. But in the harsh environments like in tokamaks, the SDD volume is constantly exposed to very high energy radiation doses as well as to neutron fluxes. This can cause dislocations or fractures in the crystal structure. Any such damage reflects local modification in the band structure, that can result into enhanced leakage current, in the end degrading the energy resolution and overall performance.

Since it is a slow cumulative processes of degradation over a year or so, there are not really quantitative data marking the degradation. Over a long term it can be noted that the frequency of the reset increases, indicating that the leakage current has increased. It is usually a sign of radiation damage to the detector.

3. SETTING UP THE SX AND HX DIAGNOSTICS

Table 3.3: Prominent X-ray lines emitted by two radioactive sources Fe-55 and Am-241 used for the energy calibration of the SDD.

Element	Line energy (keV)	Half life (years)
Mn K_α	5.89	2.737
Mn K_β	6.49	2.737
Mn K_α - escape peak	4.15	-
Am-241	11.9	432.2
Am-241	13.9	432.2

Usually a little regain in the reset period is observed when the detector is kept switched off, i.e., at room temperature, allowing self-healing processes. It is not clear whether a crystal re-arrangement occurs at room temperature, explaining the observed regain in the reset period.

3.3.3 Detector response function

In a general sense, a photon might interact in various ways inside the detector, depicting the amount of energy deposited. The photon with a fix incident energy may end up eventually in any of the MCA channels. The probability distribution that the photon of energy E , will be detected in a channel k , is called as *detector response function*. A set of distribution functions corresponding to every incident energy E_i forms a *response matrix*.

The form of the detector response strongly depends on the matter-radiation interaction processes involved, refer to Chapter 2. At 1-20 keV energy range it is seen that the dominant process is photo-electric absorption rather than the Compton scattering (see Figure 2.1). It is re-assured from our measurements of Fe-55 radioactive source, that the photo-peak to background ratio is almost 2000:1 (see Figure 3.14). This is already a quite high ratio. As a result, the observed energy and incident photon energy almost map one-to-one on each other, within a narrow width (i.e., the resolution).

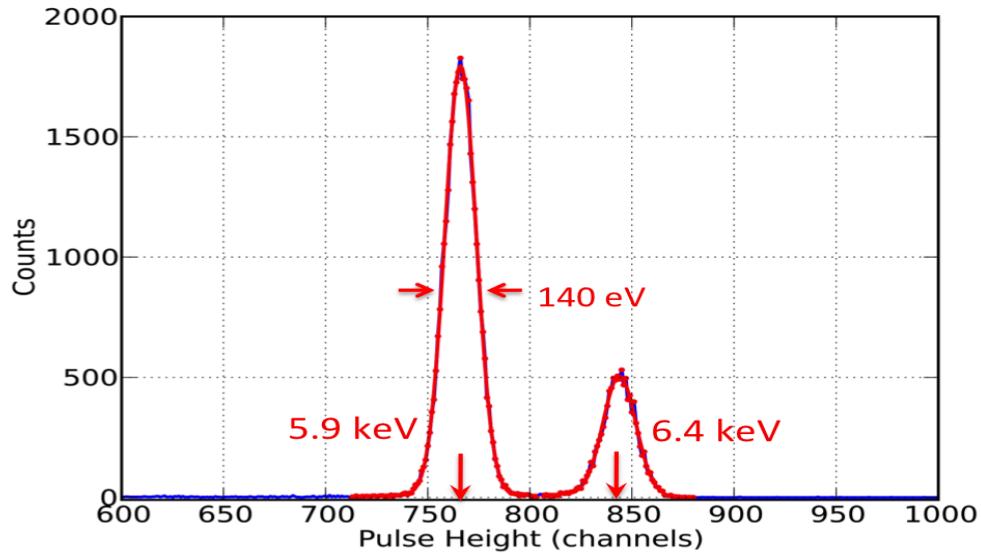


Figure 3.14: Energy resolution of SDD. The two X-ray lines emitted by Fe-55, Mn- K_{α} and Mn- K_{β} , separated by just 0.5 keV are nicely resolved.

Hence, for the soft X-ray detector, the detector efficiency along with the proper channel-energy calibration relation and the energy resolution relation simply comprises the total *response function* of the detector. For such a high peak-to-continuum ratio, the response matrix is essentially a diagonal matrix, with a definite channel-energy relation and a finite width relation.

3.4 Characterization of HXR-PHA

For the purpose of hard X-ray detection, the Silicon Drift Detector (SDD) is coupled to a scintillator CsI(Tl) (together called as HXR-SDD). We have already discussed the properties of the scintillator in Chapter 2. In scintillators the probability of interaction processes other than just the photo-absorption also become non-negligible. This makes the characterization quite complex and not so straight forward as in the case of soft X-ray detector. We will discuss the necessary steps taken in order to finally construct the detector response.

3. SETTING UP THE SX AND HX DIAGNOSTICS

3.4.1 Setup for the HXR-PHA characterization

During the initial experimentation the scintillator crystal was coupled to the SDD by means of silicon grease. Unfortunately, later we realized that the crystal causes direct strain on to the SDD surface and damage it. For all later purposes we inserted a thin silicon pad (disk) in between the SDD surface and the crystal. This combination remained very stable throughout the later experiments on tokamak.

A scintillator holder cap was designed in order to place the scintillator properly on top of the SDD, but not stressing it. The holder cap, shown in Figure 3.15, is made of steel, later replaced by ceramic, since steel increases the Compton scattered events close to the detector volume (for more details see Section 4.6). The scintillator crystal is kept in place by placing a thin plastic plate screwed on the top. The steel holder itself is screwed inside a ceramic cap. The ceramic cap holds both SDD and the scintillator holder precisely in place.



Figure 3.15: The scintillator holder cap. The steel part holds the scintillator crystal. The outer ceramic part holds both the SDD and the steel cap together rigidly.

3.4.2 Energy calibration and resolution

The number of optical photons produced by the scintillator is directly proportional to the energy of the γ -ray incident. Fortunately, the linearity of the scintillator makes

the analysis a little simpler. The linear performance is guaranteed in every further stage, i.e., conversion of the optical photons \rightarrow the electron-hole pairs \rightarrow the shaped pulse height \rightarrow the MCA channel.

We chose two radioactive sources Cs-137 and Ba-133, based on the γ -ray lines they emit, such that it spans incident photon energy over a range from 10 to 1000 keV. The various radioactive sources used and their line energies are listed in the Table 3.4. The radioactive sources, Co-57 and Co-60, available at our institute were already 30 years old (42 times and 6 times the half-life respectively), so they were not any more strong enough to be usable for calibration experiments.

Table 3.4: Prominent lines emitted by two radioactive sources Cs-137 and Ba-133 used for the energy calibration of the HXR-PHA [64].

Element	Line energy (keV)	half life (years)
Cs-137	32	30.17
Cs-137	662	30.17
Ba-133	31	10.51
Ba-133	81	10.51
Ba-133	276	10.51
Ba-133	302	10.51
Ba-133	356	10.51
Co-57	122	0.742
Co-60	1173	5.27
Co-60	1332	5.27

The laboratory measurements of the radioactive sources were performed. Since the Ba-133 was also a relatively weak source, the spectrum was accumulated over 4-5 days to get best statistics. The Energy-Channel and Energy-Width relations were then obtained. Figure 3.16 shows the linear curve for the channel-energy relation over the broad hard X-ray energy range.

Similarly, the widths of the lines were also measured in order to calculate the relation of resolution as a function of incident energy, see Figure 3.17

3. SETTING UP THE SX AND HX DIAGNOSTICS

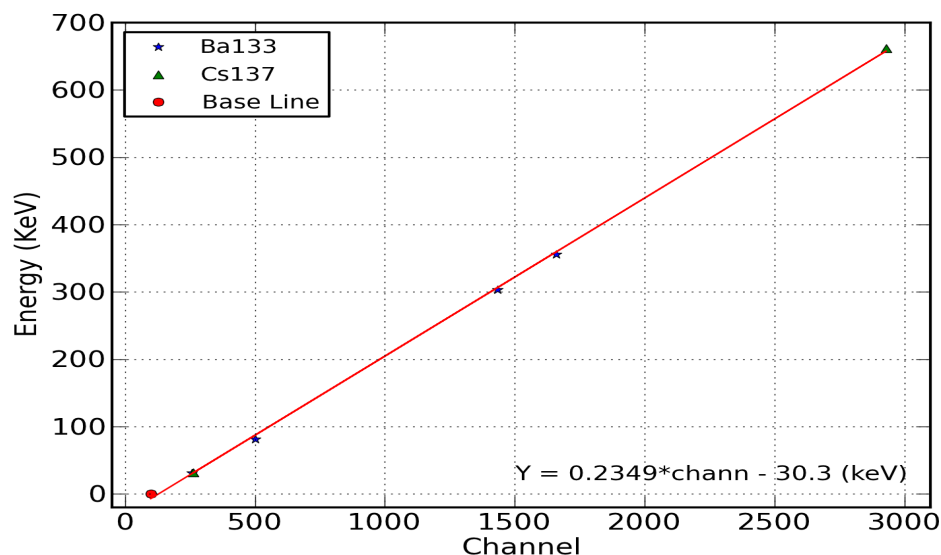


Figure 3.16: The channel-energy linear relation for the HXR-PHA setup.

3.4.2.1 Zero-point measurement

In general the 0^{th} channel does not coincide with 0 keV energy. Such an assumption can lead to a wrong calibration relation. A set of experiments were performed to pin point the (0,0) point for the calibration. An external signal generator was used to create artificial pulses of customized shape to mimic the real photon events. The pulse amplitude is equivalent to the photon energy. External pulse was given as an input to the Ring-1 of the detector through a coupling capacitor of 100 pF. This pulse is then treated in similar way as a real photon event and is measured in the end by the MCA.

We measured the pulses of 3-5 known amplitudes, and a corresponding voltage-to-channel relation is obtained. The voltage corresponding to channel-zero was measured (see Figure 3.18). The baseline voltage level of the shaper was then adjusted slowly until the voltage corresponding to channel-zero was below 0 volt. In this way it was clear that the 0 volt point will be somewhere at non-zero channel. Later the lower level voltage threshold of the MCA was set to a positive value such that it will cut down all the fluctuations on the baseline level.

The efficiency and the response of the detector is discussed in the next chapter.

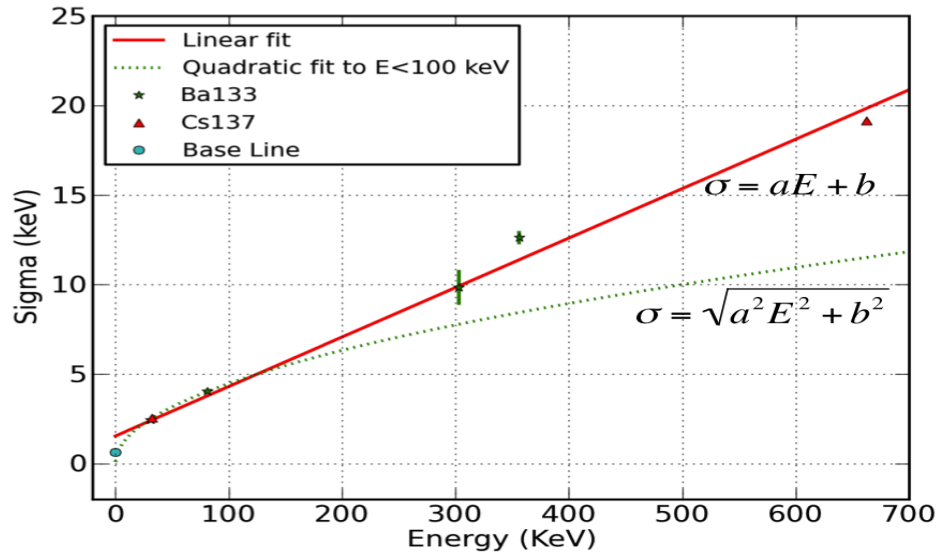


Figure 3.17: The line width-energy relation for the HXR-PHA setup.

3.5 Data handling software

The spectral data recorded in almost all the purposes mentioned in this work are done in the so-called *list* mode offered by the MCA. In list mode, the MCA creates a data entry for each photon event with its energy and time information.

To manipulate and to make maximum use of the *list* mode format data, a more sophisticated code is needed. A Python based code, called as *EventList*, first developed by B. Huber (Max Planck Institute for Plasma Physics, Garching) was used and extended it further to have more control of the analysis. A Graphical User Interface (GUI) was designed in Python to allow quick analysis of the plasma discharges.

The code *EventList* allows the following key tasks-

- Plot interactive 2D histogram of individual photon energy and time (rebinning possible).
- Slice out any specified time window and get the photon rate.
- Slice out the photon spectrum for any specified time window.
- Allow correction for - time offset, MCA live time/ real time and calibration.

3. SETTING UP THE SX AND HX DIAGNOSTICS

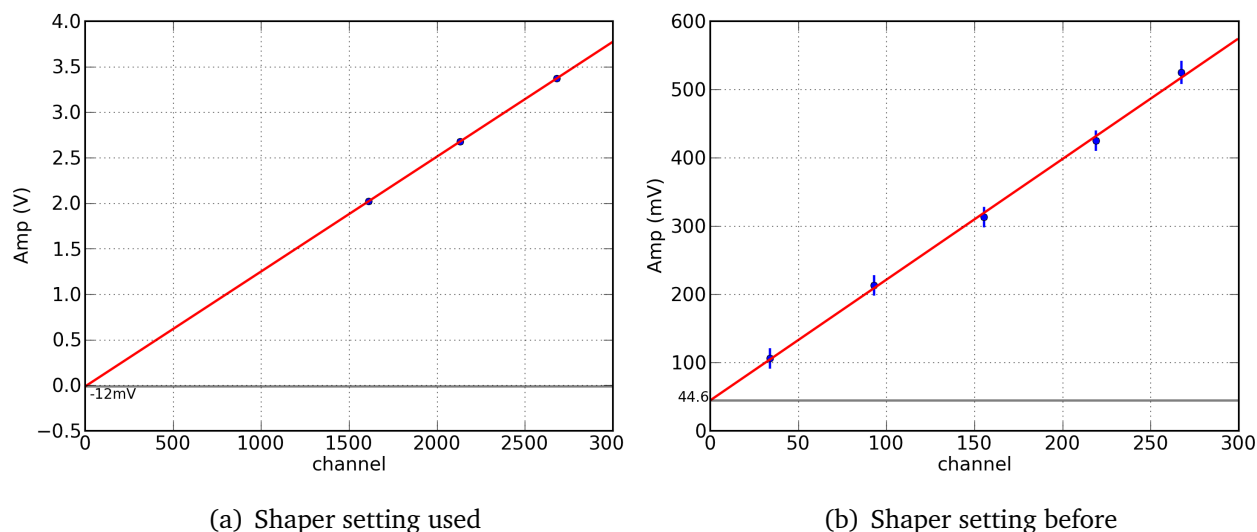


Figure 3.18: The offset of the shaper was set such that the 0 keV energy (0 volt amplitude) would appear at a positive channel value of the MCA. **(a)** 0 volt corresponds to positive channel, **(b)** 0 volt corresponds to negative channel.

- Not only rebin the spectral channels (the *rebin* feature), but also group together the channels until the photon counts are above a minimum threshold, called as *mincts* feature.
- Similar to above, *rebin* and *mincts* feature for the photon count rate.
- Export the spectrum in *.pha* file format to be used in XSPEC spectral analysis package.
- Export the spectrum for later implementation of the detector response.

For further analysis several other Python based modules were developed, such as Peak-detection algorithm, model fitting, sequential format of the background spectra, etc.

Moreover a Python based Graphical User Interface (GUI), called *EList* was also developed in this thesis work in order to allow faster data manipulation and browsing through loads of data. For more detailed description see Appendix B.

3.6 Experimental setups at different machines

An experiment was carried out WEGA stellarator facility at Max Planck Institute for Plasma Physics, Greifswald. The typical plasma temperature achieved in WEGA device is 15-30 eV, however, it emits a significant amount of radiation in X-ray regime. An experiment is carried out with our soft X-ray detector system to characterize the X-ray emission and to understand the cause of it.

3.6.1 Experimental setup at WEGA

WEGA is a small stellarator type machine. It is mainly for educational purpose and test facility for Wendelstein 7x. More details about the machine parameters can be found in the Table 3.5. A schematic of the machine is shown in Figure 3.19.

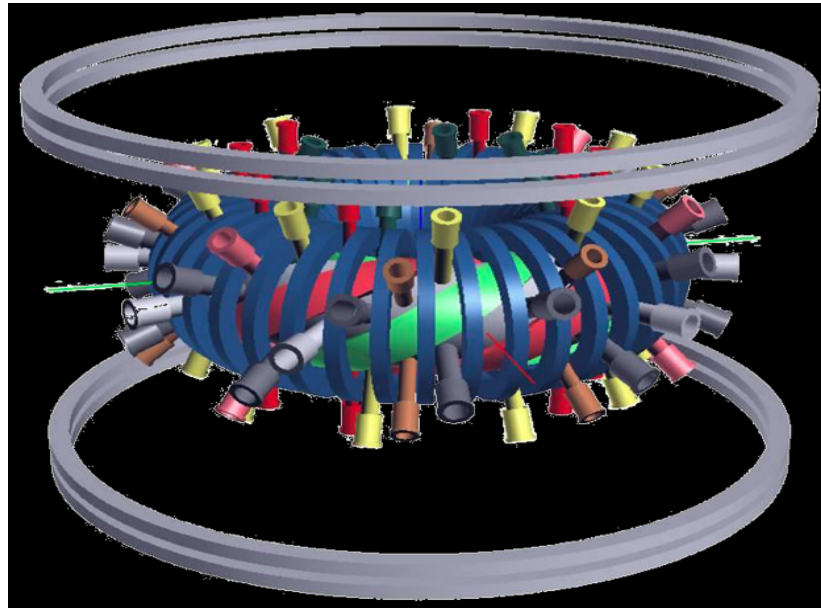


Figure 3.19: The WEGA stellarator type machine for experimental testing purposes, is located in IPP Greifswald.

We carried out a set of experiments at WEGA, with the SXR and HXR detector. The SXR detector vessel was mounted on one of the ports, looking radially into the plasma, see Figure 3.20. The SXR detector setup is as shown in Figure 3.21. A 230 mm long steel collimator cylinder was mounted on the detector, with a 5 mm steel pinhole fixed on the top of the collimator, see Figure 3.21a.

3. SETTING UP THE SX AND HX DIAGNOSTICS

Table 3.5: WEGA stellarator machine specifications

Parameter	Value
Major radius	0.72 m
Plasma gas	He/Ar
Density	order 10^{19} m^{-3}
Magnetic field	0.5 T
Heating power	Up to 20 kW (2.8 GHz)

The HXR detector was installed, however, on a first hand trial basis. The HXR detector was simply mounted inside a aluminum box, pumped to 10^{-2} mbar. The box was fixed on a rack kept facing the whole WEGA plasma vessel. The viewing solid angle was really very broad and undefined. The photograph of the assembly is shown in Figure 3.22, marked with the yellow box is the position of the HXR detector. The detector is receiving the hard X-rays emitted by the plasma, passing through the vessel wall and surroundings.

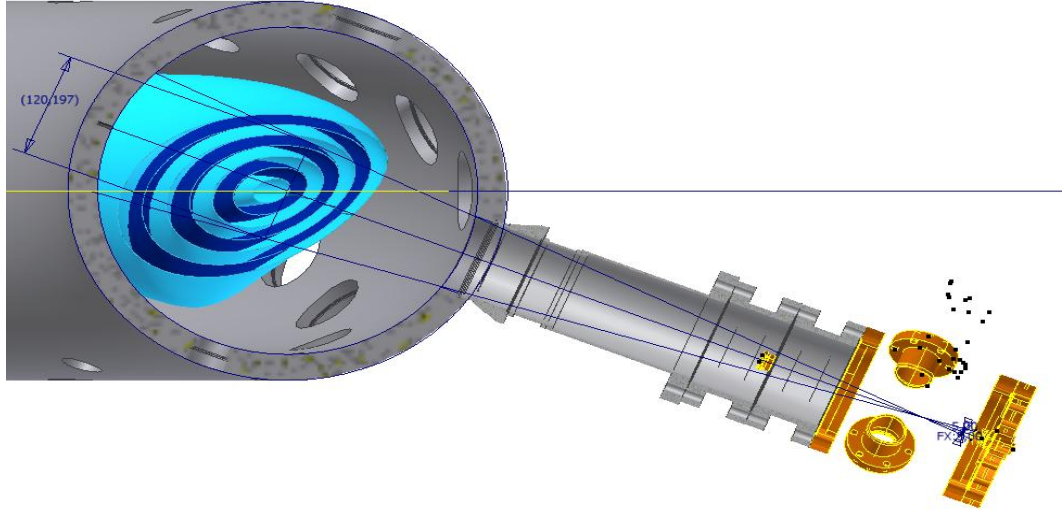


Figure 3.20: The SXR detector vessel (yellow color) mounted on one of the ports on WEGA, with the line of sight intersecting the plasma center.

3.6.2 Experimental setup at PIXE/PIGE

PIXE/PIGE stands for *Particle Induced X-ray (Gamma-ray) Emission*. It is a particle tandem accelerator facility situated at Max Planck Institute for Plasma Physics (IPP), Garching. In order to obtain the proper detector response for different incident energies, a set of strong monochromatic X-ray line sources are necessary. At PIXE/PIGE, we carried out a set of experiments in order to construct the detector response function.

A narrow (5 mm wide) beam of particles (usually protons) is accelerated to a very high energy (up to 3 MeV). The beam is then made incident on a target plate (material under study). The protons can excite atoms in which case characteristic X-rays are emitted, or at very high proton energies they can excite the nucleus in which case a set of characteristic γ -rays are emitted [94; 95], see Figure 3.23.

It is a unique facility where a discrete set of γ -ray lines can be produced, spanning over the energy range of our interest. A very interesting experiment was carried out at this facility in order to characterize the response function of the HXR detector. More details are discussed in the next chapter.

The HXR detector vessel was mounted on one of the ports on the horizontal plane, viewing the target plate, at a distance of roughly 50 cm. Since the expected pho-

3. SETTING UP THE SX AND HX DIAGNOSTICS

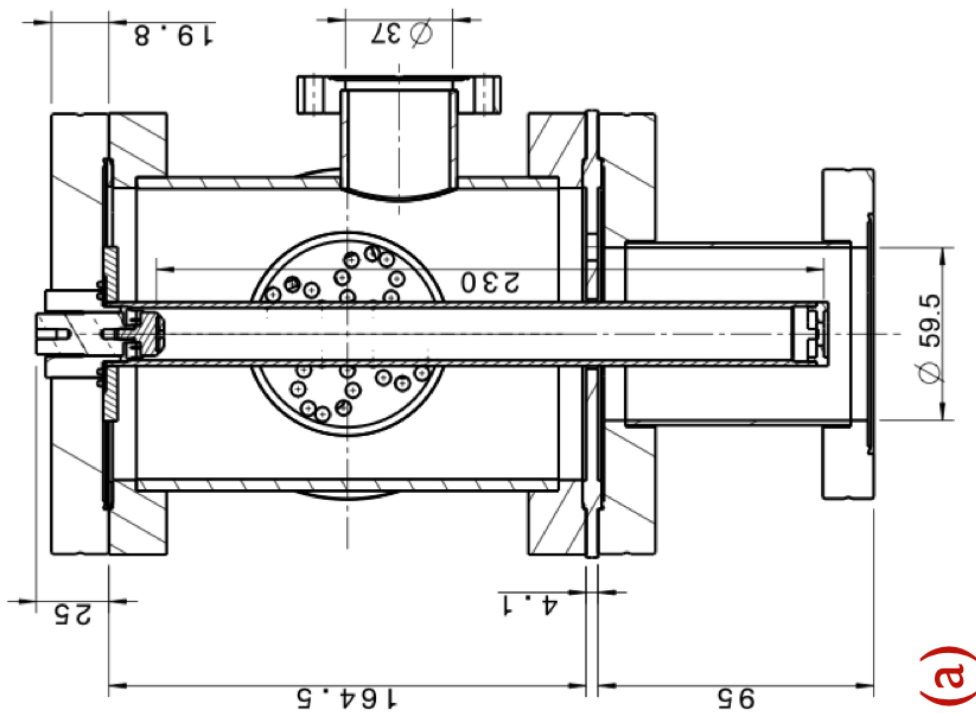
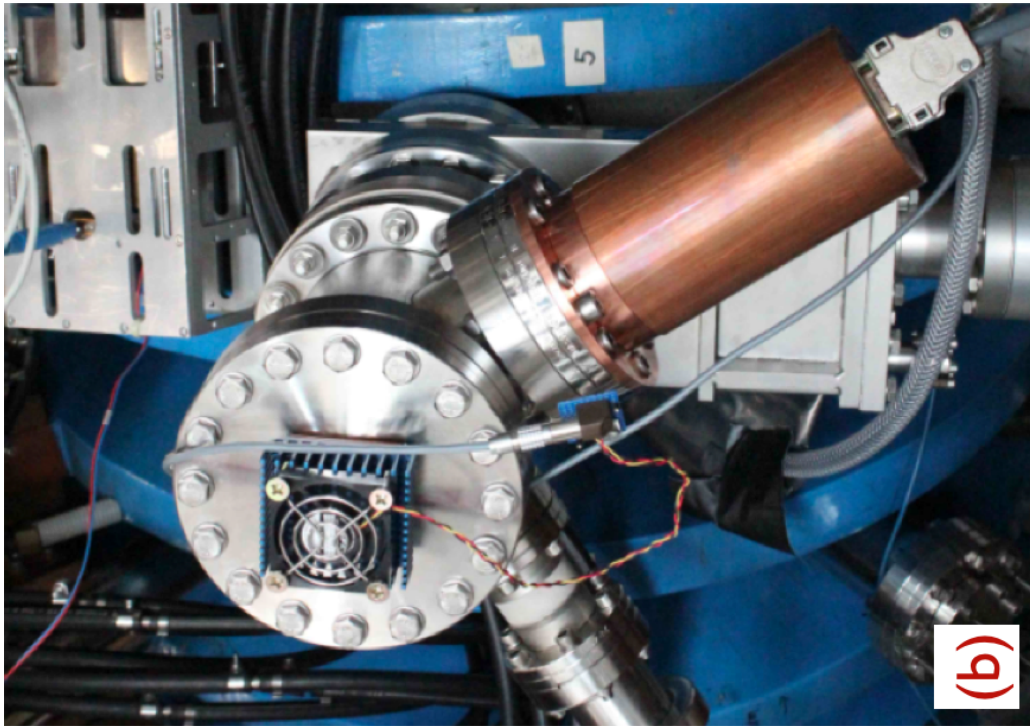


Figure 3.21: (a) Modified design of the detector vessel, shows the 23 cm long collimator with a 5 mm wide pinhole in the end. (b) Detector vessel installed on the horizontal plane of the WEGA stellarator.

3.6 Experimental setups at different machines

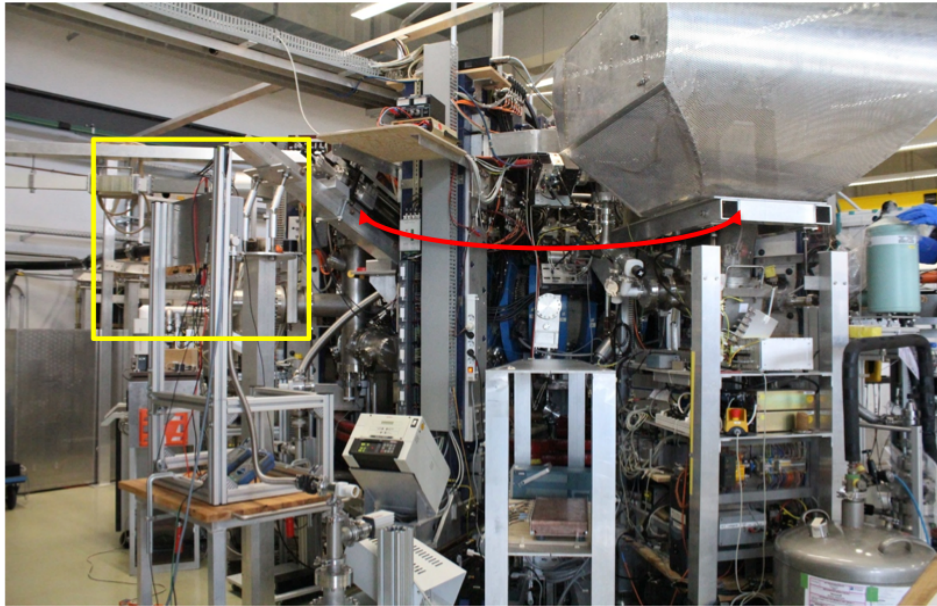


Figure 3.22: The HXR detector (marked by yellow box) placed facing the WEGA plasma vessel. The direction of the plasma vessel is marked by the red curve.

ton flux was too low, no pinhole was installed along the line of sight. A thin (0.3 mm) Aluminum filter was installed in order to cut down the unwanted soft X-ray bremsstrahlung radiation.

3. SETTING UP THE SX AND HX DIAGNOSTICS

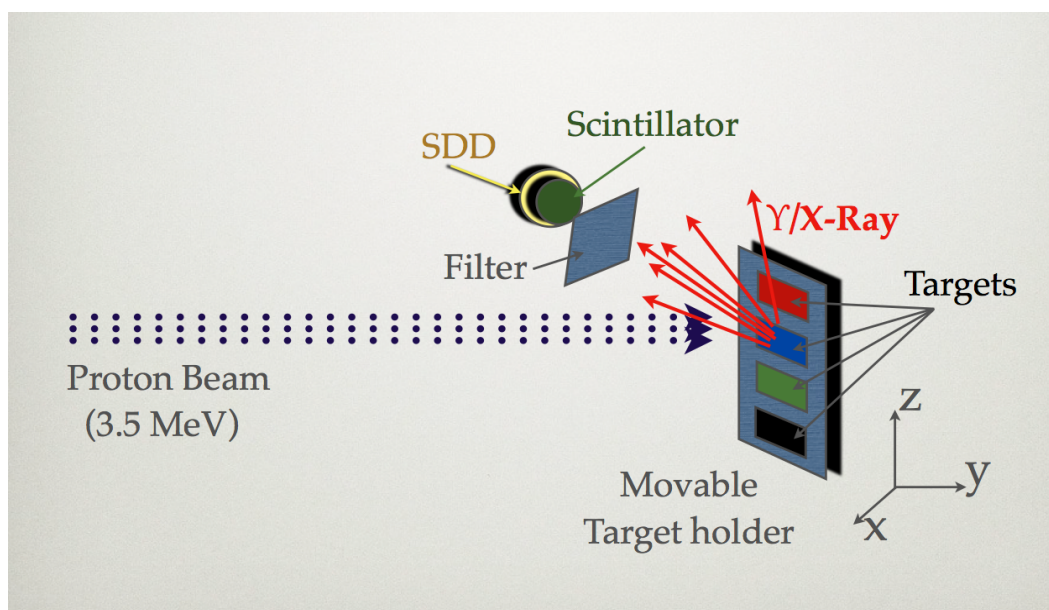


Figure 3.23: The cartoon of the experimental assembly at PIGE/PIXE facility at IPP. The HXR detector, mounted on one of the ports is directly receiving the X-ray emission.

3.6.3 Experimental setup at ASDEX Upgrade

ASDEX Upgrade is a tokamak type device situated in Max Planck Institute for Plasma Physics, Garching [13; 15]. The machine main specifications are mentioned in Table 3.6.

The experiments at ASDEX Upgrade were carried out in three campaigns. In the (first) 2009-campaign the aim was to learn the typical first hand problems arises in the tokamak environment and learn about the proper requirements of the future setup. The SXR detector vessel was installed on the port on top of the tokamak, in the poloidal plane, looking vertically downward into the plasma, close to the plasma center, shown in Figure 3.24. A primitive HXR detector setup, similar to the one used at WEGA experiments, was also installed for same learning purpose. In the later campaigns 2011 and 2012, the focus was on establishing the proper HXR diagnostics.

In the later campaigns 2011 and 2012, (unlike the primitive HXR setup) the proper HXR setup was constructed and installed on the port 16Bo in a toroidal (horizontal) plane, looking radially into the plasma, close to the plasma center, as shown in Figure 3.25.

The detector vessel was shielded with 2 layers, (a) lead bricks (inner layer) and (b) paraffin wax bricks (outer layer), see Figure 3.26 and 3.27. The high-Z material

3.6 Experimental setups at different machines

Table 3.6: The main specifications of ASDEX Upgrade tokamak machine [15].

Parameter	Value
Major radius	1.65 m
Minor horizontal radius	0.5 m
Minor vertical radius	0.8 m
Plasma gas	D, H, He
Density	order 10^{20} m^{-3}
Magnetic field	3 T
Plasma current	0.4 - 1.6 MA
Pulse duration	< 10 sec.
Heating power	Up to 27 MW
Ohmic	1 MW
NBI	20 MW
ICRH	6 MW (30 - 120 MHz)
ECRH	4 MW (120 MHz)

lead stops the γ -rays, preventing the detector being hit by them. The paraffin wax bricks have a lot of hydrogen dissolved in it. Hydrogen, having the same mass as that of neutrons, offers maximum energy transfer with the energetic neutrons and helps stopping them after multiple interactions within the paraffin brick. It was also confirmed that the line of sight is not blocked by any other component and where exactly the line of sight intersects inside the plasma. Figure 3.28 shows the photograph of the line of sight taken from the plasma side.

3.6.4 Future proposed Assembly

A new detector vessel is proposed to avail all three types of measurements - soft X-ray, hard X-ray and background/neutron signal properties. The schematic of the three-detector system is shown in the Figure 3.29. Due to time constraint it will be the part of a future development. It is proposed to have the three detectors mounted on the same flange, with three lines of sight into the plasma for the simultaneous study of the plasma properties over the extended X-ray energy range.

A special steel window, having three holes each of 1 cm diameter covered with Be-

3. SETTING UP THE SX AND HX DIAGNOSTICS

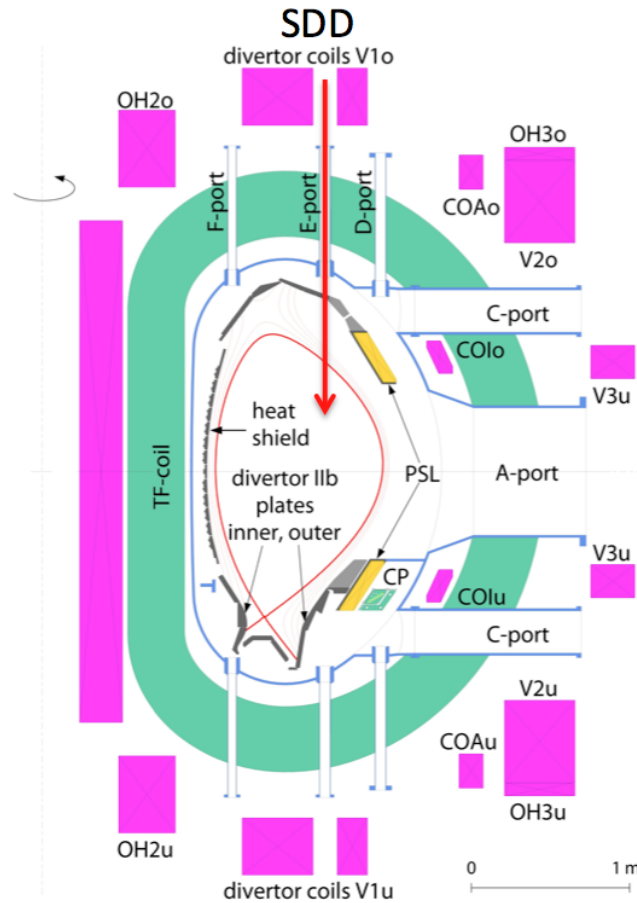


Figure 3.24: The SXR detector installed on port 14Eo at ASDEX Upgrade.

foil ($20 \mu\text{m}$ thick) is fixed on one side of the vessel, which separates the vacuum side from the detector vessel side. The two detectors (SX and HX) each can see through a set of filters and pinholes mounted on a rotating wheel remotely controlled, according to the plasma scenario. Rotating/moving parts are usually tricky to handle in the presence of strong magnetic field, and need a reliable solution. All three detectors, each separated by 2 cm, will be mounted on a single flange. The flange will also have four guiding rods which can aid the proper orientation of the flange with respect to the individual lines of sight of the three detectors. For the test and calibration purposes, it is necessary to take the detectors to the test laboratory frequently. It is very cumbersome for such bulky setups to frequently transport from between different places. A similar outer container vessel is planned to be placed permanently in the test laboratory. In this way detaching only the detector flange will be sufficient and

3.6 Experimental setups at different machines

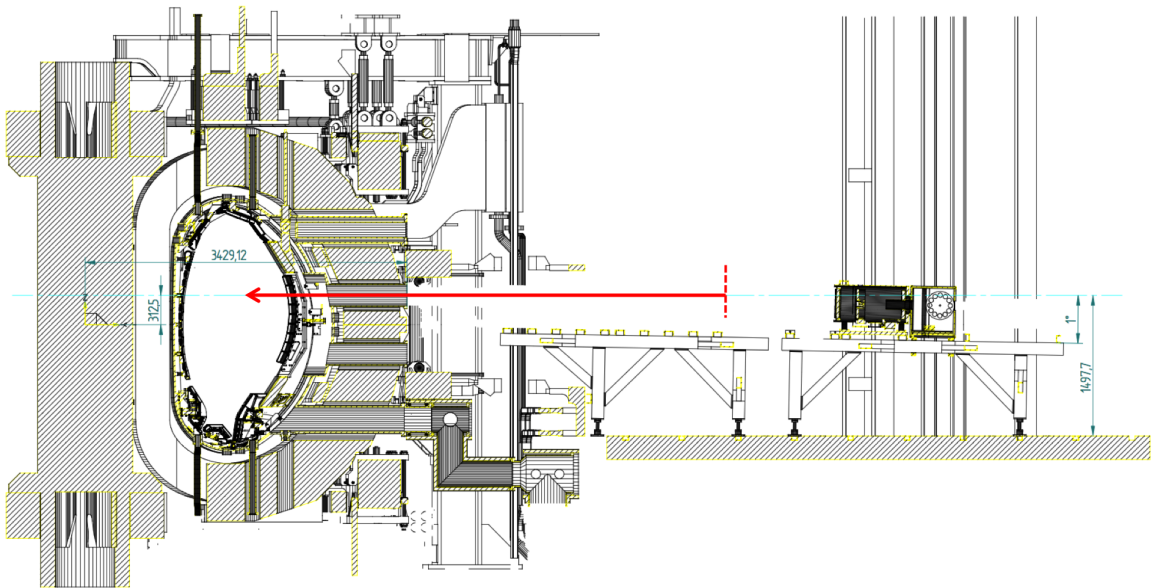


Figure 3.25: The cross-section of the port 16Bo at ASDEX Upgrade, the red line shows the line of sight of the HXR detector.

easy to transport from the laboratory to the tokamak and so on.

3. SETTING UP THE SX AND HX DIAGNOSTICS



Figure 3.26: The HXR detector vessel is properly shielded against the neutrons and stray γ -rays in the ASDEX hall, by the lead bricks (inner-wall) and paraffin wax bricks (outer-wall).

3.7 Forward modeling technique for HXR: Block diagram

The hard X-ray detector produces non-standard spectral data which depend particularly on our detector type and the assembly. To aid the analysis of this spectral data produced by the hard X-ray detector, a pipe-line is developed. The analysis pipe-line consists of a number of Python-based modules, as shown in the block diagram Figure 3.30. These modules have been developed in this work, inspired by the well known astronomical soft X-ray analysis package called XSPEC [96]. The function of each of these module is described briefly in the following sections.

3.7.1 Module EventList

The module EventList is already discussed in the Section 3.5. The key feature of the module EventList is that it allows analysis of both spectral and timing information for each incident photon. Depending on the needs during the analysis, the data can be sliced in time and energy as per interest. This approach also provides a great flexibility in rebinning the data in constant or variable size bins of both time and

3.7 Forward modeling technique for HXR: Block diagram

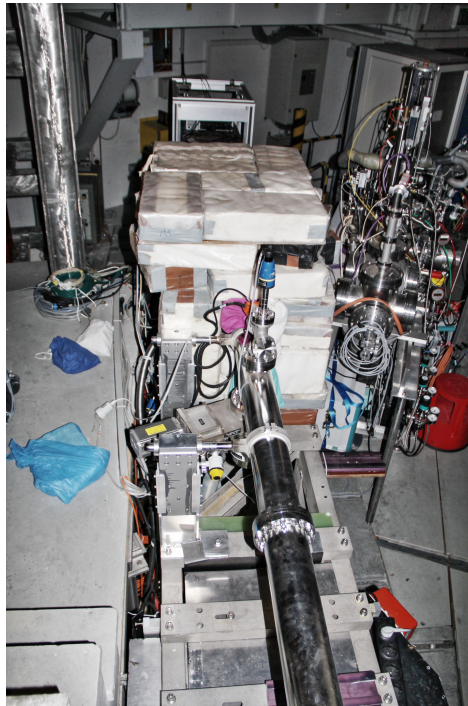


Figure 3.27: The HXR setup installed at ASDEX Upgrade hall on 16Bo port. Downward is the direction of plasma. The white bricks cover the HXR detector vessel completely.

energy. The EventList also provides an easy data visualization and manipulation tool, see Appendix B.

3.7.2 Module `genResp`

The module `genResp` (stands for *generate response*) uses the instrument response matrix, simulated using the Geant4 package (described in Section 4.2), and obtains the response matrix function (RMF) (described in Section 4.4). The RMF is then reshaped to match the observed spectral energy range. If a specific filter is used in the detector setup then the appropriate filter absorption function is incorporated and the user ready response matrix is uploaded.

3.7.3 Module `genModel`

The module `genModel` (stands for *generate model*) generates a thermal plasma emission model. The main process responsible for the continuum emission in hard X-ray range is the bremsstrahlung process, see Section 1.6.1.

3. SETTING UP THE SX AND HX DIAGNOSTICS

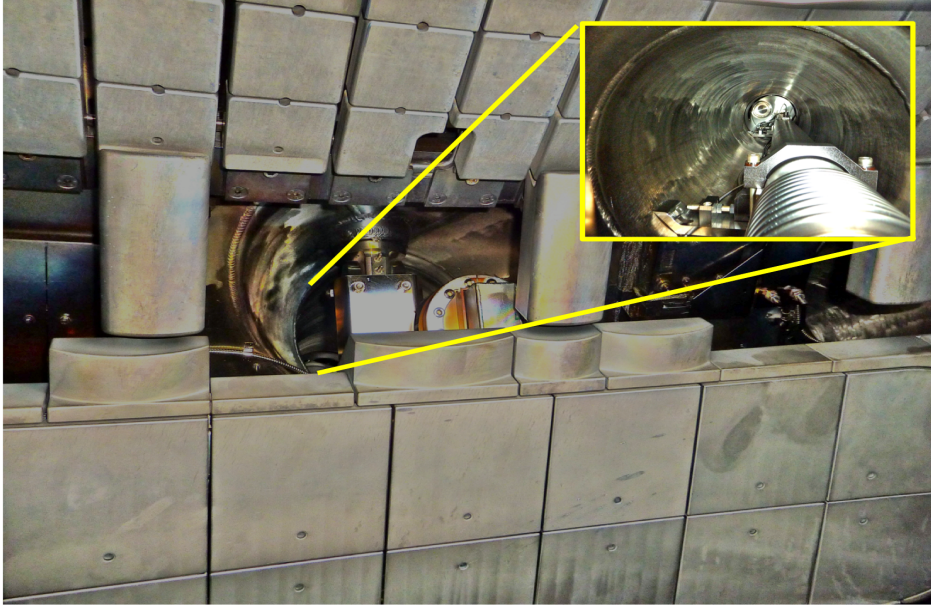


Figure 3.28: The line of sight seen from inside of the tokamak vessel. It was noted that some metallic structure obscures the right part of the circular port. But since our line of sight lies in the left upper half part of the port (yellow box), it is least affected.

In the tokamak geometry, the electron density (n_e), ion density (n_i), and electron temperature (T_e) varies as a function of normalized plasma radius (ρ) (refer to Section 1.3.1 for tokamak geometry). Since the plasma is assumed to be quasi-neutral, the ion density closely follows the electron density, so we only need to know the electron density profile.

Using Equation 1.30, the module `genModel` estimates the plasma emissivity over space and energy via the equation $M(\rho, E)$

$$M(\rho, E) \equiv M(n_e(\rho), T_e(\rho), E) \quad (3.2)$$

At ASDEX Upgrade, the $n_e(\rho)$ and $T_e(\rho)$ profiles are available through an Integrated Data Analysis (IDA) code. IDA incorporates data from various diagnostics to construct more reliable and constrained profiles of n_e and T_e . The `genModel` allows the standard IDA ($n_e(\rho), T_e(\rho)$) profiles as the input arguments.

The emission into the detector from the specific line of sight is then calculated by performing a line integration over the model emissivity. The line integrated emission is called as *chord brightness* ($\text{W} \cdot \text{cm}^{-2} \cdot \text{eV}^{-1}$)

3.7 Forward modeling technique for HXR: Block diagram

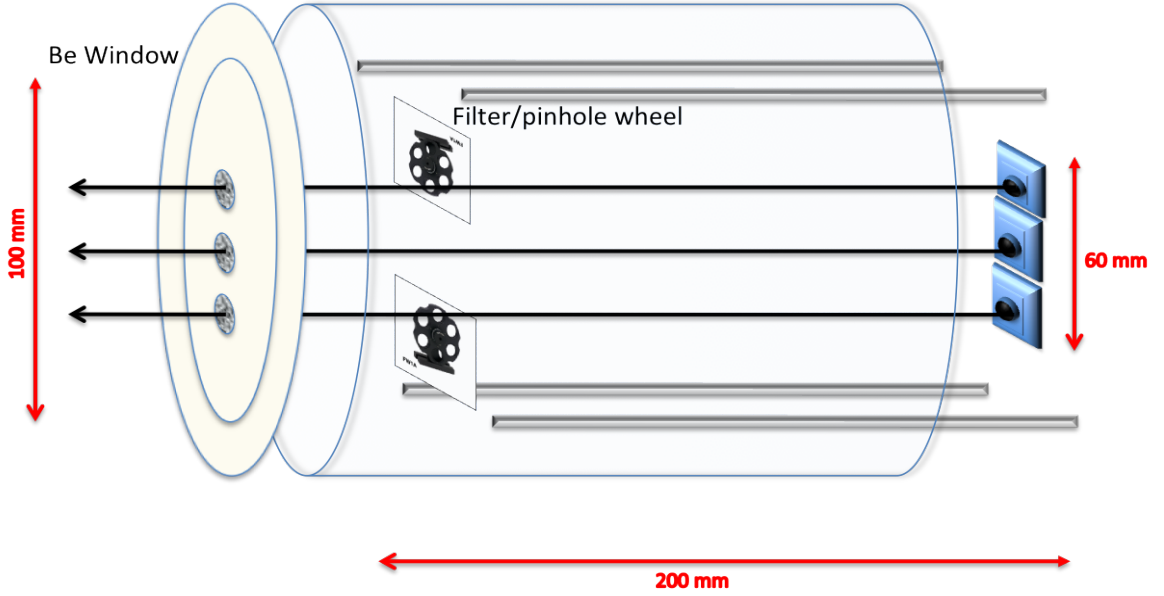


Figure 3.29: The cartoon of the three-detector setup, combining all the SX, HX and neutron effect monitoring in a single diagnostics.

$$B(E) = \int_{\rho_{min}}^{\rho_{max}} M(\rho, E) d\rho \quad (3.3)$$

The power incident on the detector, through the defined viewing geometry is represented by the chord brightness $B(E)$.

To benchmark the estimates by genModel, the thermal plasma emission is simulated for the following specifications, assuming Gaussian profiles for the electron temperature and electron and ion densities. The parameters are listed in Table 3.7

Table 3.7: Plasma parameters

	Peak	sigma
$T_e(\rho)$	30 keV	0.3
$n_e(\rho)$	$1 \times 10^{13} \text{ cm}^{-3}$	0.1
$n_i(\rho)$	$1 \times 10^{13} \text{ cm}^{-3}$	0.7

The plasma chord brightness is then estimated between 1-50 keV energy.

Similar estimates were made by another independent code IONEQ, originally developed for soft X-ray study at Wendelstein-7s, by Dr. A. Weller (Max-Planck-Institute

3. SETTING UP THE SX AND HX DIAGNOSTICS

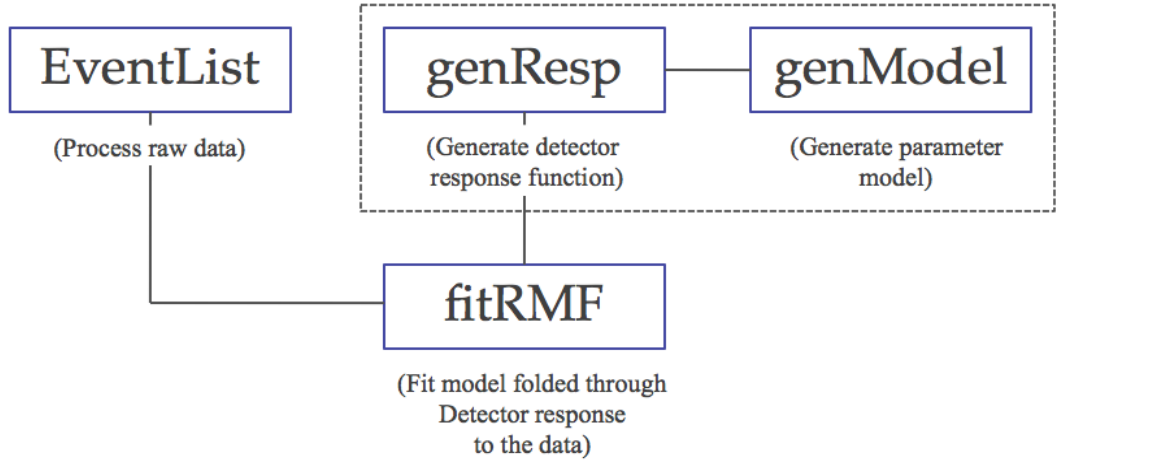


Figure 3.30: The blocks for the HXR spectral analysis forward modeling technique.

for Plasma Physics, Garching) [51]. The estimation from `genModel` is compared with the IONEQ calculations. For comparison, refer to Figure 3.32 (IONEQ) and 3.33 (`genModel`). The black dotted-line marks the peak position from IONEQ in both figures. Both the estimations are found close to each other, $\sim 0.4 \times 10^{-7} \text{ (W} \cdot \text{cm}^{-2} \cdot \text{eV}^{-1})$.

The code IONEQ is, in principle more thorough and tested, incorporating the ionic equilibrium and recombination radiation, mainly in the soft X-rays up to 50 keV. Whereas, the module `genModel` is written, mainly for free-free radiation processes over several keV energy based on the bremsstrahlung cross-section provided by G. Rybicki [42], see Section 1.6. Even though both the modules estimate free-free emission based on the same physical equation, the basic difference resides in the value of Gaunt factor, which is different for higher energies.

After having this essential confirmation, we proceed further by combining the chord brightness with the detector response.

3.7.4 Module `fitRMF`

The module `fitRMF` (stands for *fitting data with the model convoluted through the RMF*) combines the measured spectrum with the model spectrum through the detector response. The module `fitRMF`, as shown in the block diagram Figure 3.30,

3.7 Forward modeling technique for HXR: Block diagram

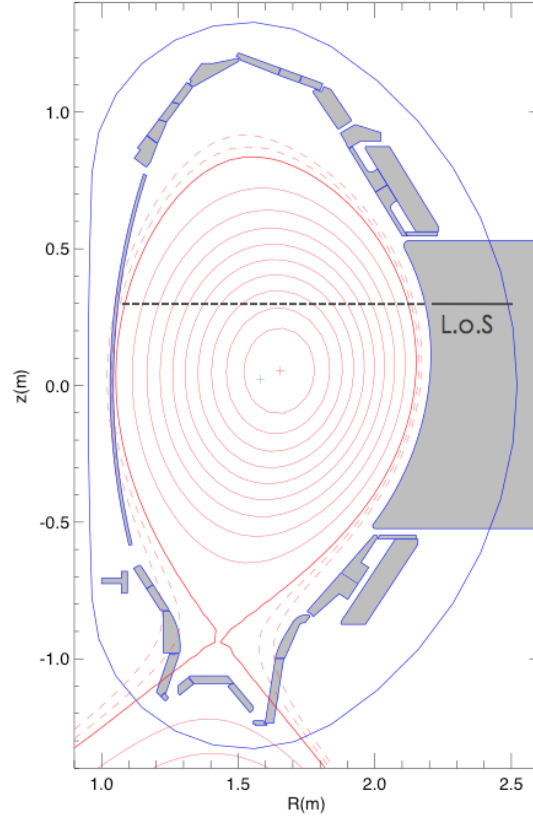


Figure 3.31: The plasma emissivity is estimated over the equilibrium flux surfaces shown in red. The HXR line of sight is shown in black.

takes as input three quantities, (a) the measured spectrum, (b) the model spectrum, and (c) the detector response matrix. The fitRMF converts the measured spectrum ($\text{counts} \cdot \text{sec}^{-1} \cdot \text{keV}^{-1}$) into the measured power ($\text{W} \cdot \text{cm}^{-2} \cdot \text{eV}^{-1}$) by dividing by the correct etendue factor.

The model chord brightness (Equation 3.3) is convolved with the detector response (plus the transmission filter function $\eta(E)$) and the spectrum as observed through the detector $D(E)$ ($\text{W} \cdot \text{cm}^{-2} \cdot \text{eV}^{-1}$) is estimated

$$D(E_j) = \int_{E_{i,\min}}^{E_{i,\max}} B(E_i) \cdot \eta(E_i) \cdot R(E_i, E_j) \cdot dE_i. \quad (3.4)$$

The estimated spectrum $D(E)$ (suffix ‘ j ’ dropped for convenience), is then compared with the measured spectrum $C(E)$.

For our reference, we once again list all the terms defined in the analysis.

3. SETTING UP THE SX AND HX DIAGNOSTICS

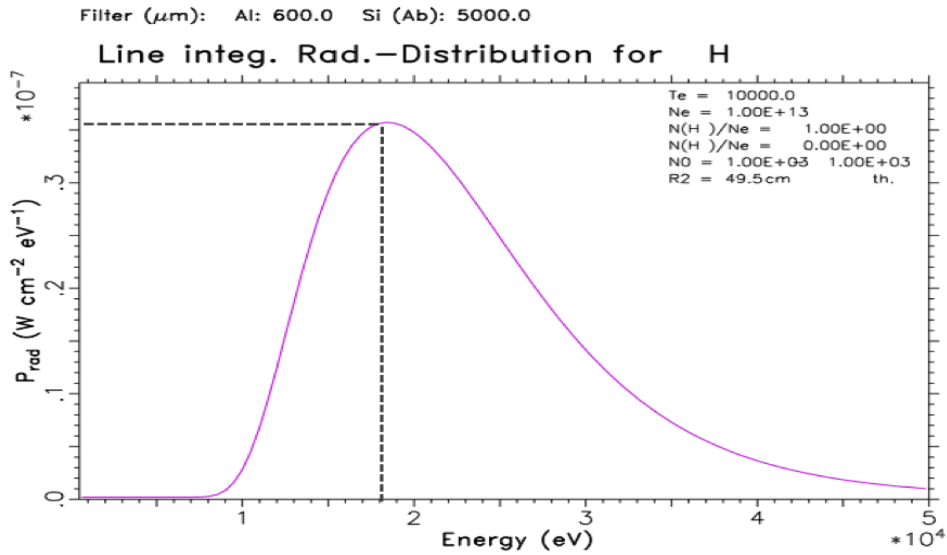


Figure 3.32: The chord brightness estimated using code IONEQ.

- $\epsilon(E)$ The thermal bremsstrahlung emissivity
- $M(\rho, E)$ Dependence of bremsstrahlung emissivity on plasma equilibrium flux surface (normalized radius) and energy.
- $B(E)$ The chord brightness; integrated over the detector line of sight
- $C(E)$ The measured spectrum
- $D(E)$ The model observed spectrum

3.7 Forward modeling technique for HXR: Block diagram

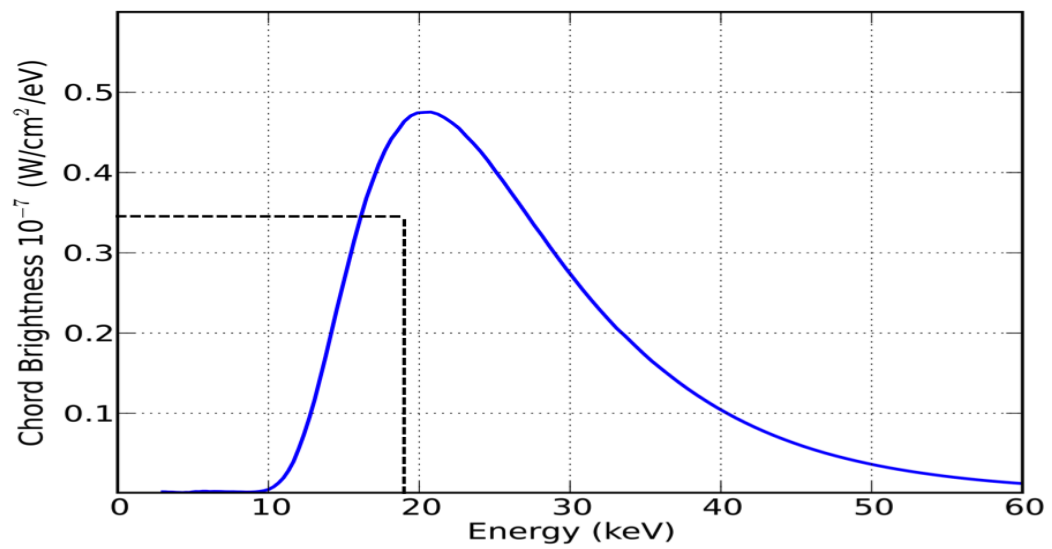


Figure 3.33: The chord brightness estimated using module genModel.

3. SETTING UP THE SX AND HX DIAGNOSTICS

“In theory, there is no difference between theory and practice. But, in practice, there is. ”

- Jan L. A. van de Snepscheut

4

Construction of the Detector Response Matrix

4.1 Introduction

In the hard X-ray spectral analysis, it is necessary but not sufficient to have the Energy-Channel and Energy-Width relations. It is also necessary to know how the incident photon interacts with the detector. Especially at higher photon energies the photon may deposit only a fraction of energy and escape the medium. That means the deposited energy can take any value between 0 to E_{max} , and make the response complicated.

In this chapter we estimate the total efficiency of the detector and how the detector responses over a range of photon energies. Before introducing the laboratory experiment set for verifying the estimated detector response, we introduce and briefly discuss the simulation tool Geant4, modified for our purposes.

4.2 Geant4 simulation package

To know the response of the detector to the X-rays incident, first we need to calculate which fraction of the energy is deposited in the scintillator. The interaction processes such as photo-absorption, Compton scattering, pair production etc. (already discussed in the previous section), have an energy dependent cross-section. A powerful simulation package *Geant4* (GEometry ANd Tracking) offers a unique platform to test and simulate various physics processes involved in the detector [97] [98]. It offers the simulation of the passage of different types of particles (as well as electromagnetic waves) through matter using Monte Carlo methods. It is developed by CERN under the C++ object oriented programming. The Geant4 has already found and well tested applications in various fields including, accelerator, high energy physics, medical, nuclear physics, and space physics.

Some of the capabilities the Geant4 package provides are,

- Geometry : Defining the bounding volume of different materials, detector, absorbers, etc. and how it will affect the passage of the particle under study.
- Tracking : Passage of the particle through matter by considering various interaction and decay processes.
- Run management and visualization : Creating and recording the information of every event and offering possible visualization.

4.2.1 Implementation

The Geant4 allows to precisely define the geometry and composition of the detector material and its surrounding. An interacting particle can be chosen i.e. a photon, proton, neutron, electron, etc. For our study purpose, we concentrate only on electromagnetic waves and interaction with matter. The initial detector specific python based environment was created by B. Huber (Max Planck Institute for Plasma Physics, Garching), and was later modified as per the aim.

The approximate geometry of the CsI(Tl) scintillator and surrounding material was defined. An incident photon spectrum, over the energy range 3 keV to 3000 keV, is simulated, see Figure 4.1. The energy range is divided into 1064 bins, with the bin width increasing as \sqrt{E} . For every incident energy E_i (here subscript i refers to

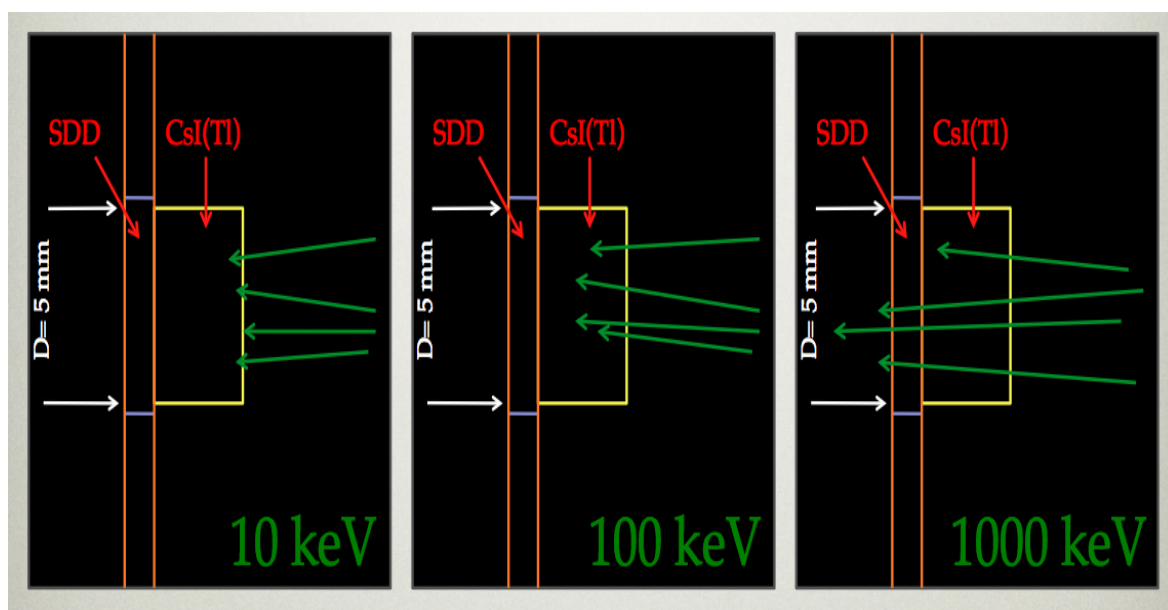


Figure 4.1: Geant4 simulation visualization

incident energy), different physical processes (e.g., Compton scattered and photo-ionization) are calculated within our uniquely defined geometry and composition of the detector. For every incident energy E_i , the amount of energy deposited over all the 1064 bins E_j (here subscript j refers to recorded energy), is recorded.

4.3 Efficiency

The fraction of the photon energy deposited in the scintillator as a function of the energy translates into the efficiency of the detector. Figure 4.2 shows the simulated fraction of energy deposited via photo-absorption and Compton scattering. The pair production process does not play a role, since it is beyond the energy interval of interest. The total efficiency (blue curve in Figure 4.2) is the sum of the two processes. The low energy cut off appears due to the absorption by the 0.6 mm thick Al-filter, included in the efficiency calculation.

Note that the scintillator generates a spectrum of visible light, which is then received by the SDD with the corresponding efficiency. This process is not included in the simulation. It also means, the simulation does not give any information about the resolution of the detector. The optimum matching of the efficiency of the SDD and the scintillator light spectrum is demonstrated in [85]. Moreover the scintillator

4. CONSTRUCTION OF THE DETECTOR RESPONSE MATRIX

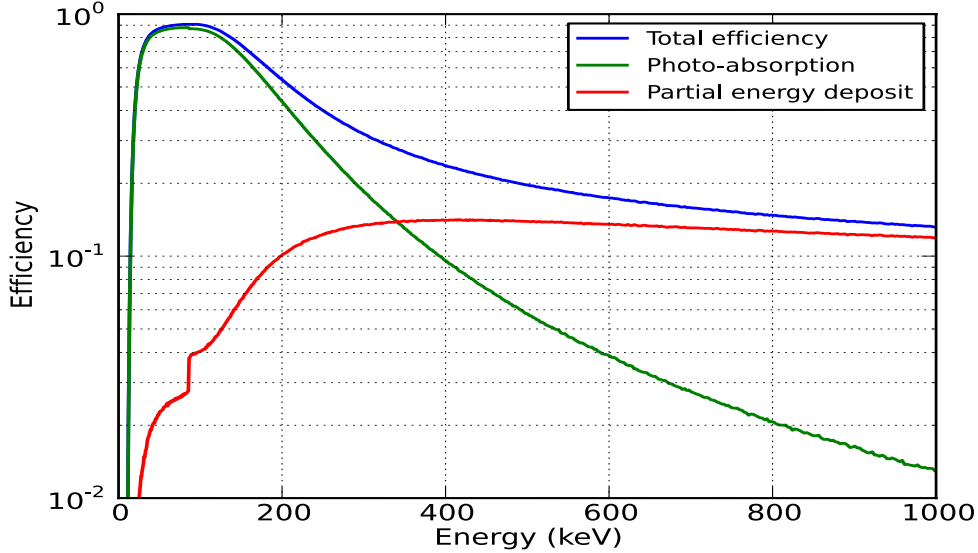


Figure 4.2: The photon energy is absorbed dominantly by photo-absorption process at lower energies, whereas at higher energies the dominant process is Compton scattering. The low energy cut off is due to Al-filter absorption.

light *spectrum* is independent of the incident X-ray energy. The simulation shows that the detector gives close to 100% efficiency up to 100 keV and then it starts falling down to 10% at 1MeV.

4.4 Detector response function

For the spectral analysis, it is necessary but not sufficient to have only Energy-Channel and Energy-Width relations. More important is to know, what is the probability that the incident photon of energy E_i , is recorded in the detector within a finite energy bin dE at an energy E_j .

In other words, for every fixed incident energy (E_i), we will have a probability distribution function $p_i(E_i, E_j)$, defined over the discrete variable E_j . The probability distribution functions p_i are constructed by simulating the interaction processes of 1 million photons at each energy value E_i . The set of all normalized probability functions p_i , forms an Interaction Probability Matrix, $T[i, j]$.

The probability distribution functions p_i are not corrected for the resolution of the detector. The resolution also varies as a function of energy, i.e., $\sigma(E_i)$. Using the

width-energy calibration relation, a resolution matrix $W[i, j]$, is constructed.

$$W[i, j] = \frac{1}{2} \left[\operatorname{erf} \left(\frac{E_j - E_{c,i}}{\sqrt{2}\sigma_j} \right) - \operatorname{erf} \left(\frac{E_{j-1} - E_{c,i}}{\sqrt{2}\sigma_j} \right) \right] \quad (4.1)$$

Where, erf is the error function. $E_{c,i}$ is the central energy of the i^{th} bin. σ_j is the resolution at j^{th} energy value.

The interaction probability matrix ($T[i, j]$) or rather each probability value under $p_i(E_i, E_j)$ is then redistributed by convolving with the resolution matrix

$$R[i, j] = T[i, j] \otimes W[i, j]. \quad (4.2)$$

Such a matrix $R[i, j]$ is then called as *Redistribution Matrix* or *Response Matrix Function* (RMF), $R[i, j]$. The RMF is the matrix used for all later processes. It tells what is the probability that the incident photon of energy E_i , is recorded in the detector within a finite energy bin dE at an energy E_j . The code, called as *genResp*, is developed to carry out the task of obtaining RMF from the interaction probability matrix $T[i, j]$ convolving with the resolution matrix $W[i, j]$.

To visualize the response matrix, in Figure 4.3 few rows are plotted. For example, the curve shaded in blue corresponds to an incident energy of 500 keV.

The discrete matrix $R[i, j]$ is 2-dimensional spline smooth function $R[E_i, E_j]$, still called as the response matrix function. A source spectrum $S(E_i)$ incident on the detector is observed through the response matrix

$$f(E_j) = \int_0^{E_{max}} S(E_i) R[E_i, E_j] dE_i. \quad (4.3)$$

It is this quantity $f(E_j)$, the detector measures. If we want to comment on the incident spectrum $S(E_i)$, ideally it should be obtained by inverting the integral. But this is not always easy and may lead to a non-unique solution and very sensitive to even small variations in the initial conditions.

4.4.1 Test of eigenvalue ratio

Under two conditions, it is possible to invert the integral Equation 4.3. First, if the inverse of the matrix $R[i, j]$ exists and second, if the ratio of the extreme eigenvalues of the matrix satisfy the following condition [99]

4. CONSTRUCTION OF THE DETECTOR RESPONSE MATRIX

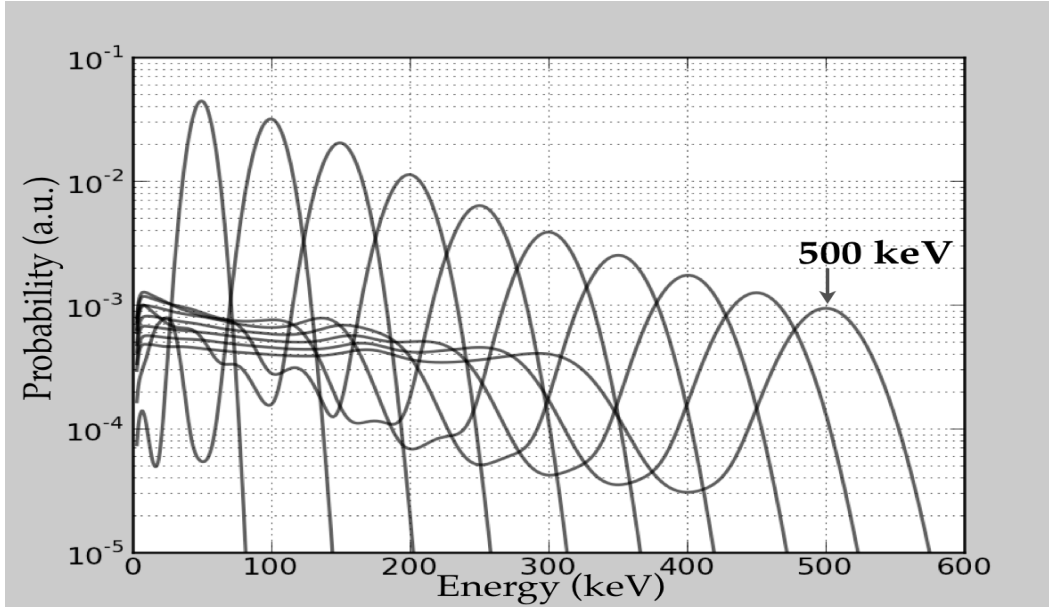


Figure 4.3: Different rows from the response matrix function are plotted to visualize the matrix.

$$\frac{\lambda_{max}}{\lambda_{min}} \leq 10. \quad (4.4)$$

The ratio was obtained to be much higher than 10. So inverting the integral was not possible for this problem. Instead, for all the later purposes we assume a model function to represent the incident spectrum and estimate observed spectrum and then compare it with the spectrum actually recorded, as discussed in Section 3.7.

4.5 Experiment at PIXE/PIGE

An experiment was designed to test the simulated response matrix. In the Section 3.6.2, we already discussed the setup for the experiment at the PIGE/PIXE facility at IPP, Garching. For this experiment four metallic targets were chosen, which emit γ -rays over the range 0 to 500 keV, listed in Table 4.1.

The proton beam was operated at energy 2.3 MeV. The typical spectra measured with the four targets are shown in Figure 4.4. Each of the recorded spectra are roughly accumulated over 20 min to 30 min. Noise was monitored by recording the signal with and without the proton beam.

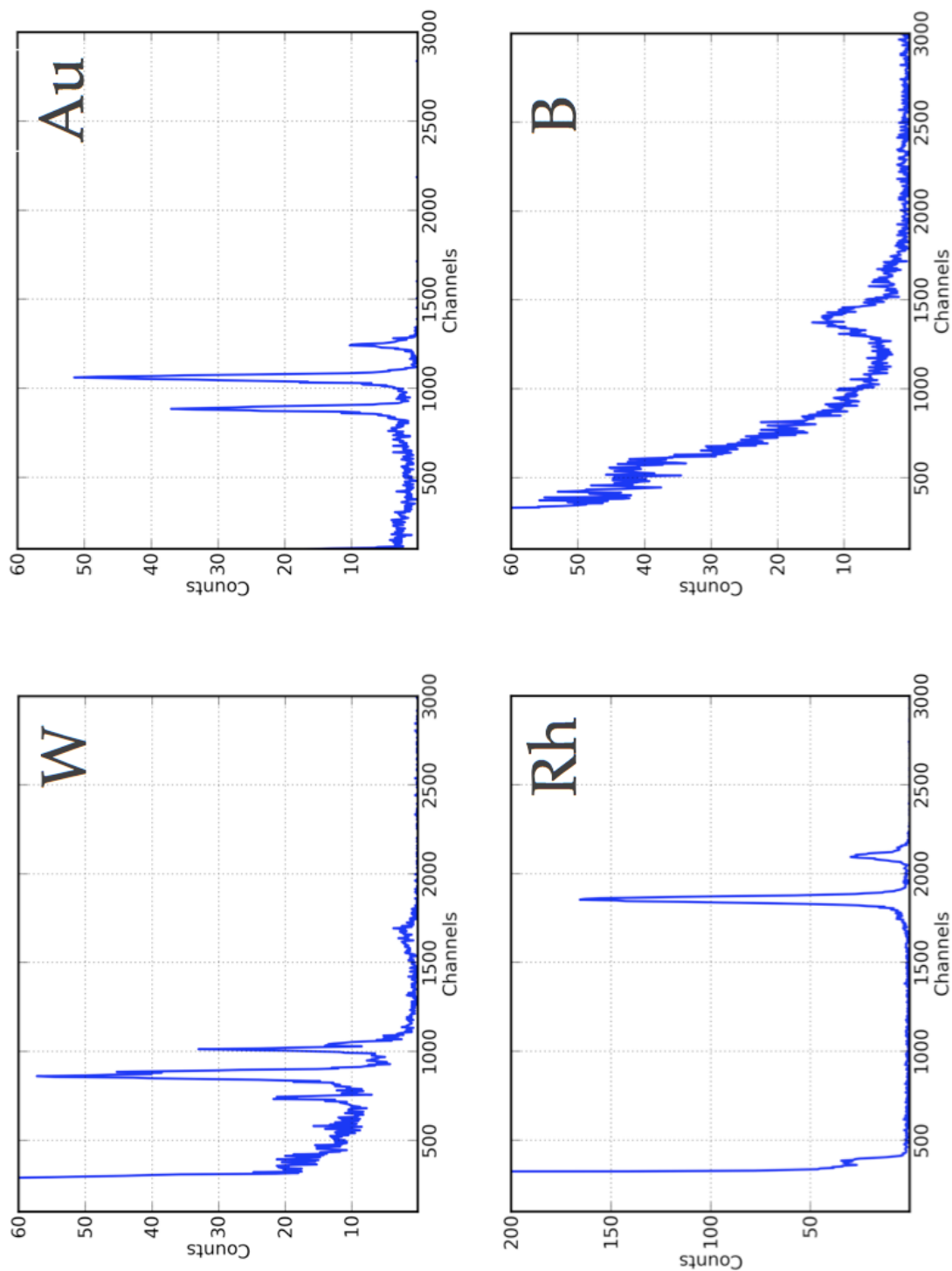


Figure 4.4: The uncalibrated spectra of the four different targets chosen.

4. CONSTRUCTION OF THE DETECTOR RESPONSE MATRIX

Table 4.1: Prominent lines emitted by the selected targets at PIGE. Also the prominent characteristic X-ray lines are listed [94; 95].

Element	Gamma rays (keV)	X-rays (keV)
Au	279	K _{α1} –69 K _{α2} –67 K _{β1} –78
W	100 111 123 292	K _{α1} –59.3 K _{α2} –58 K _{β1} –78 –
Rh	295 357	K _{α1} –20.2 K _{α2} –22.7
B (Boron Carbide)	429 718	– –

In addition to the PIGE emission, three reliable reference points were obtained by in situ measurements with the radioactive Cs-137 source and a very weak Ba-133 source. The expected γ -line energies were plotted against the measured channel positions. It was noted that there exists a systematic mismatch between the channel and the line energies, as seen in Figure 4.5a. The γ -lines from targets Au, W and Rh appeared much below the expected channel-energy relation. The same is true for the width-energy relation as well, see Figure 4.6. Only the target element B (Boron Carbide) exhibits both the line energy and width nicely over the expected relation within the error.

It was then suspected that there might be very prominent excitation of the characteristic X-ray lines rather than the γ -lines, and the signal is due to these X-ray lines (see Table 4.1). When the measured channel positions were plotted against the prominent X-ray lines (see Figure 4.5b), two (Au, W) out of three sources showed different but consistent channel-energy and width-energy relations. The target Rh, one of the strongest sources, appeared to be neither following expected gamma-line relation nor the X-ray line relation.

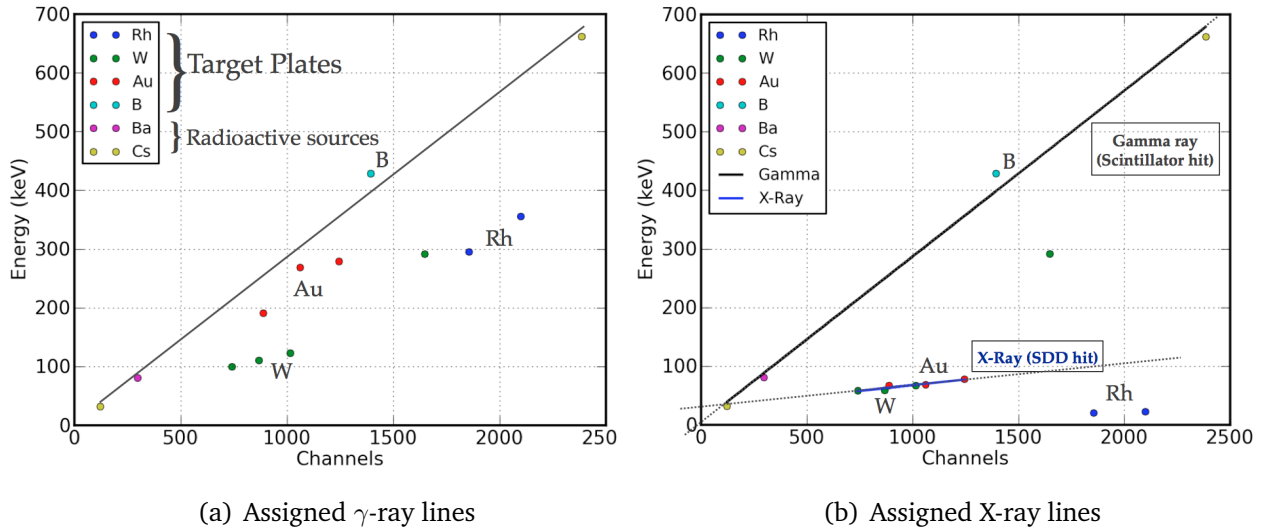


Figure 4.5: The channel-energy relation obtained from the line emission from photon beam induced reactions and radioactive sources.

The observations were soon realized to be quite unexpected. Since, prior to our experiment under this facility, there was no attempt made to measure the γ -rays emission from the targets requested, we did not have any direct cross check with our measurements.

During further investigations, some of the points were speculated which might be responsible for our experimental findings.

(a) There was no induced γ emission at all or very insignificant emission. However, it could be only partially true, since Boron Carbide (B) target showed a very weak expected γ -line.

(b) The directionality of the induced γ emission is unknown, and there could be only low emission in the direction of the detector.

(c) There could be only strong X-ray fluorescence, which was hitting directly the SDD from the peripheral side. (The scintillator diameter is 5 mm, exposing the outer 1 mm SDD area).

Due to the limited time at the PIGE/PIXE facility it was not possible to investigate each speculation in further details, which would have also diverted our initial goal of the experiment. Nevertheless, the experiment created a lot of issues and scope for the future experimentation with the HXR and SXR detector at PIGE/PIXE.

4. CONSTRUCTION OF THE DETECTOR RESPONSE MATRIX

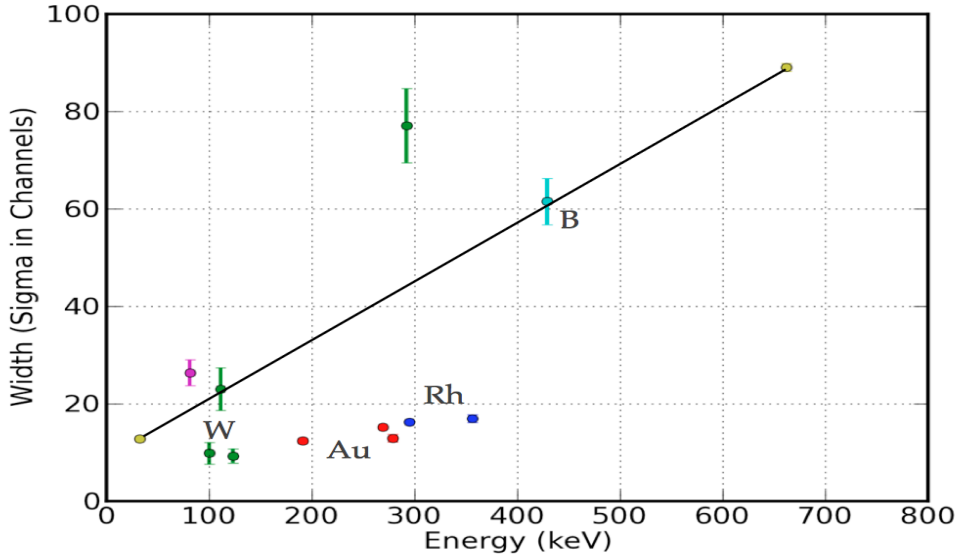


Figure 4.6: The width-energy relation obtained from the line emission from photon beam induced reactions and radioactive sources.

4.6 Test measurements for the response matrix

To validate the simulated response matrix, ideally one should have many mono-energetic, collimated gamma ray sources, i.e. $S(E_i) = A \cdot \delta(E - E_i)$ where, the right hand side is a Kronecker delta function with amplitude A . We used a radioactive source Cs-137, which emits a single gamma line at energy 662 keV. Although the line energy is beyond our range of interest and in spite of the fact that the Peak-to-Compton ratio is too poor, it provides a very good test to accurately simulate the observed spectrum. The typical spectrum of the Cs-137 radio-active source is shown in Figure 4.9 (by solid blue dots).

For 662 keV line radiation, it was not expected to record any events beyond 662 keV, but in contrast a prominent tail up to 2000 keV was measured, see Figure 4.9. This unexpected tail was initially suspected to be from the cosmic background. In another experiment in monitoring the cosmic background, we observed that it is three orders of magnitude below the measured level. The huge difference between the measured spectrum of the source and the spectrum of the cosmic background, suggested that probably the source was not a pure 662 keV γ -ray emitter, but also emits β -particles. Actually, it is well known that Cs-137 emits two β -particles (~ 0.5 and 1 MeV). However, it is not known how β -particles would interact within our detector

4.6 Test measurements for the response matrix

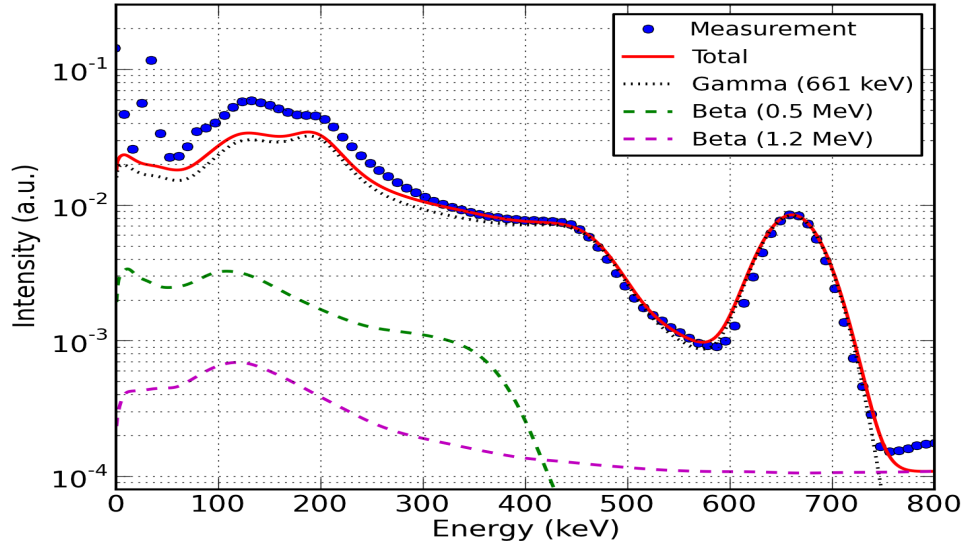


Figure 4.7: The simulated total response curve (red) for the 662 keV (Cs-137) line compared with the measured spectrum (solid blue dots).

volume. The source was kept 10 cm away from the detector and it was suspected that the electrons would get lost as they traverse through a mild vacuum medium (~ 1 mbar) and if so, then how prominently would they affect our measurements? For this purpose we modified the simulations to incorporate the β -particles as well.

The experiment with the radioactive source introduces some more complications as,

(a) the radioactive source is not collimated and emits radiation in all the directions,

(b) the components surrounding the detector (more importantly, the steel flange and the vessel) can scatter off the radiation toward the scintillator,

(c) The interaction of the two beta-particles (0.5 and 1.2 MeV) within the scintillator and the bremsstrahlung emission from surrounding metal components.

We not only simulated the detector response to the 662 keV line energy but also the effect of the surrounding material and beta-particle interaction with a reasonable accuracy. Figure 4.7 shows the comparison between the observed spectrum and the simulated detector response. By incorporating the β -particles in the simulations, we could also reproduce the observed extended tail. This laboratory test provided us with an increased confidence in our Response Matrix Function constructed with

4. CONSTRUCTION OF THE DETECTOR RESPONSE MATRIX

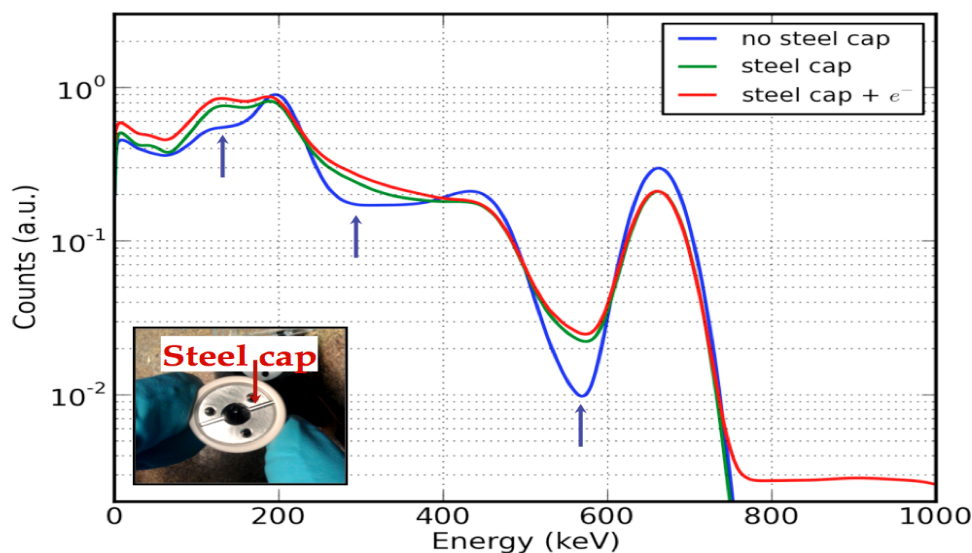


Figure 4.8: It was estimated that the steel cap holding the scintillator is causing some fraction of the Compton scattered photons to enter the detector volume. The effect of steel cap and the β -particle is included in the simulations (red curve).

Geant4, to be used in further spectral analysis purposes. Moreover, further information was obtained on the optimization of our detector assembly.

Going one step further, we performed the simulations with and without the steel cap holder for the scintillator. It was noticed that the steel material present in the very vicinity of the scintillator, was causing some of the Compton scattered lower energy photons to enter the scintillator and deposit energy, affecting the width of the photo-peak and the Compton continuum shape, (marked by blue arrows in Figure 4.8). Based on these studies we later replaced the steel cap with a ceramic one.

In case of the laboratory measurements with the radioactive sources, there is major effect of all the metallic components surrounding the detector and source, since the radioactive source emits in all direction. If the radiation incident is mostly in a forward direction then the effect of surrounding material would be least, except the steel flange at the backside of the detector.

4.6 Test measurements for the response matrix

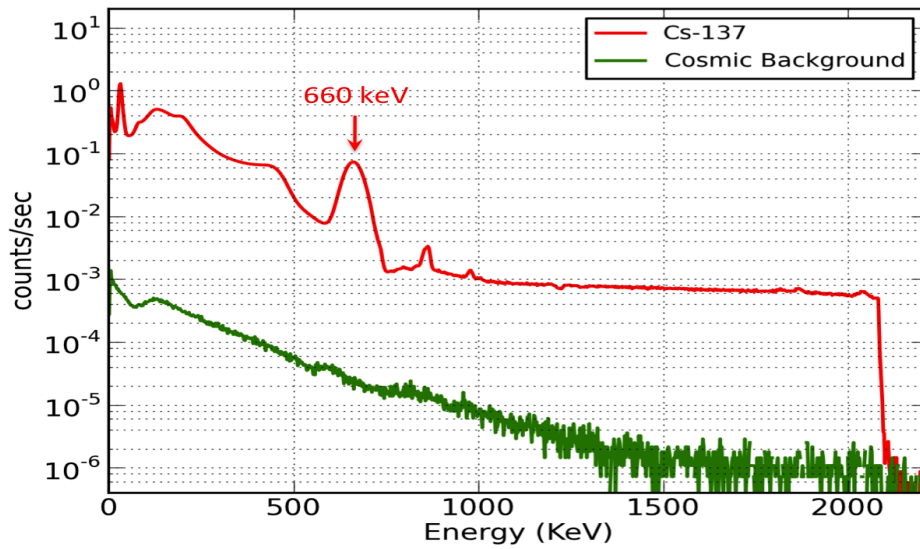


Figure 4.9: The Cs-137 (red) and the cosmic background (green) spectrum, both accumulated over 4-5 days period.

4. CONSTRUCTION OF THE DETECTOR RESPONSE MATRIX

“If mathematically you end up with the incorrect answer, try multiplying by the page number”

Murphy’s law

5

Measurements of superthermal electrons

5.1 Introduction

In this chapter we will describe the measurements and properties of the superthermal electrons. Since our primary goal was to explore more the plasma scenarios with dominant ECRH, first I will concentrate on the measurements in hard X-rays performed at ASDEX Upgrade.

5.2 Initial validation experiments

The HXR detector was installed at port 16Bo at ASDEX Upgrade. Before the actual plasma observations, it is essential to examine the noise performance of the detector under the tokamak environment. Usually any detector system is susceptible to the electric or magnetic oscillations in the tokamak hall. These electric or magnetic fields arise because of the numerous other active devices - power supplies, vacuum pumps, switches, current coils, etc. in the tokamak hall. A bad grounding scheme might as well result in unwanted noise in the detector assembly.

5. MEASUREMENTS OF SUPERTHERMAL ELECTRONS

Based on the experience prior to the 2012-campaign, the detector assembly was upgraded to eliminate maximum possible sources of noise (as described in Chapter 3). Initial test experiments were performed in order to see the influenced of various electromagnetically active components in the tokamak hall.

A good opportunity to test the detector performance is during the magnetic field coil test (probe test) shots. During the test shots the machine is fully operational except there is no plasma. Figure 5.1 shows the detector behavior during such a test probe shot (# 27456) from 10-18 sec. Each red-dot (in Figure 5.1) is a photon event in a particular channel (equivalent to energy) in the detector. The average rate of photons is (at quiescent times ¹) ~ 0.5 count/sec. The rate ~ 0.5 count/sec of these random photon events is close to the background (quiescent radioactivity) γ -ray flux on the detector. In Figure 5.1 we compare three time intervals - before the shot (0-10 sec), during the shot (10-18 sec), and after the shot (18-100 sec). The background activity remains unchanged over the shot period. This shows that there is absolutely no influence of the noise indicating the detector insulation scheme working properly.

Two examples of typical noise from the 2011-campaign are shown in Figure 5.2. Both blue and green curves show the spectral measurements of the background radioactivity in the tokamak hall, recorded over the night. The blue curve shows an expected broad spectral line appearing at channel ~ 450 plus a continuum between channel 100-750. The green curve shows a spectrum similar to the blue curve and in addition to it there is a narrower line feature appearing at channel ~ 500 . The narrow spike is identified as a strong radio frequency noise suddenly picked up by the detector assembly. Moreover, both the curves show enhanced counts in the channels below channel 100. This is because of the low amplitude fluctuations mimicking real photon events.

Although it is impossible to eliminate the noise completely, we have achieved the noise level suppressed much below the detection threshold.

5.2.1 Neutron signal

Deuterium plasmas in AUG heated by Neutral Beam Injection (NBI) emit relatively high neutron fluxes of up to about a few 10^{15} neutrons/sec. The main contribution is due to D-D fusion reactions between thermal D-ions and fast injected D-ions which

¹Quiescent time is when the tokamak hall is not heavily radioactive.

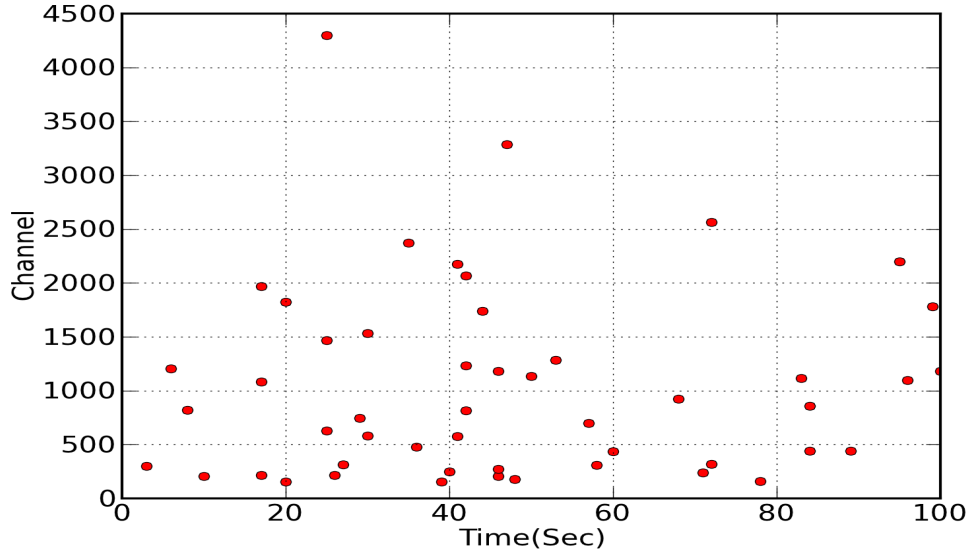


Figure 5.1: Shot #27456. Time trace of 100 seconds, with the shot executed between 10-18 sec. The appearance of photon-events (red dots) at different channels (or energy) has no correlation with the shot time (10-18 sec), showing the total suppression of the noise in the detector assembly.

are slowed down by collisions with the thermal plasma. The neutrons are born with 2.5 MeV energy.

The neutrons induce signals in the detector similar to that of the photons, except that the neutrons produce broad-peaked (slow) pulses (see Figure 5.3). The neutron flux is unavoidable, but its possible to account for it because of its characteristic features. Figure 5.4 shows the typical neutron induced spectrum recorded with our new HX diagnostic, showing a peak around 150 keV and an extended tail over several keVs. The neutrons, due to inelastic scattering with the surrounding materials, thermalize to form almost a continuum energy spectrum. When a neutron is incident on the detector, only a small fraction of its energy is deposited in the detector. From the measured spectrum alone it is difficult to comment on the underlying energy spectrum of incident neutrons. However, it is possible in the near future to simulate the detector response function for the neutrons to obtain the underlying incident neutron energy spectrum.

In most of the hard X-ray detectors, it is impossible to separate out the neutron signals from γ -ray signals. In order to do that we need to have a *Pulse Shape Discriminator (PSD)* [100]. It also means, we need to have a two-channel data acquisition

5. MEASUREMENTS OF SUPERTHERMAL ELECTRONS

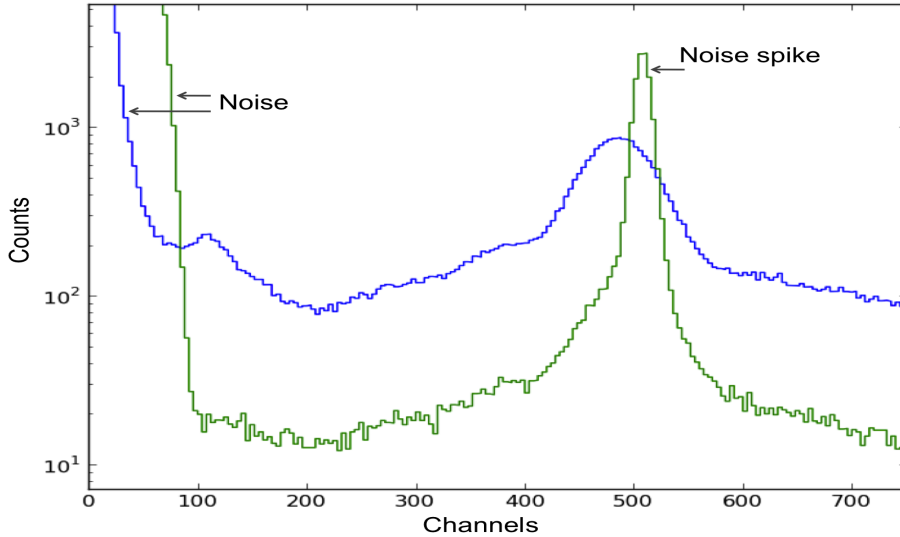


Figure 5.2: Typical spectral recording of the background radioactivity at two time intervals (blue and green curve) during the 2011-campaign. The noise usually appears in two forms, noise in the lower channels, and a spike due to radio interference.

system. Due to limited resources it was not feasible to implement a PSD, more time and man power investment is needed.

5.2.2 Count rate limit

The neutrons, being charge-less are difficult to stop. High energy neutrons, due to their low cross-section, can even pass through few centimeters of steel material without interacting. We saw in the previous section that the neutrons do affect the HX measurements, but only when the neutron flux is above a certain limit, there is a finite probability of considerable neutron interactions within the detector volume of just $\sim 100 \text{ mm}^3$.

During most of the high power NBI discharges, the neutron flux is much too high ($\sim 10^{15}$ neutrons/sec), which forces the detector to keep scintillating all the time (saturation). A distinct spectral feature is noticed when the detector reaches this saturation limit (shown by grey region in Figure 5.5).

The reason found for such a feature is that, when the detector is flooded with charges all the time and the detector preamplifier undergoes frequent resets, the baseline is drawn down during the reset and the reset pulse itself falls below the

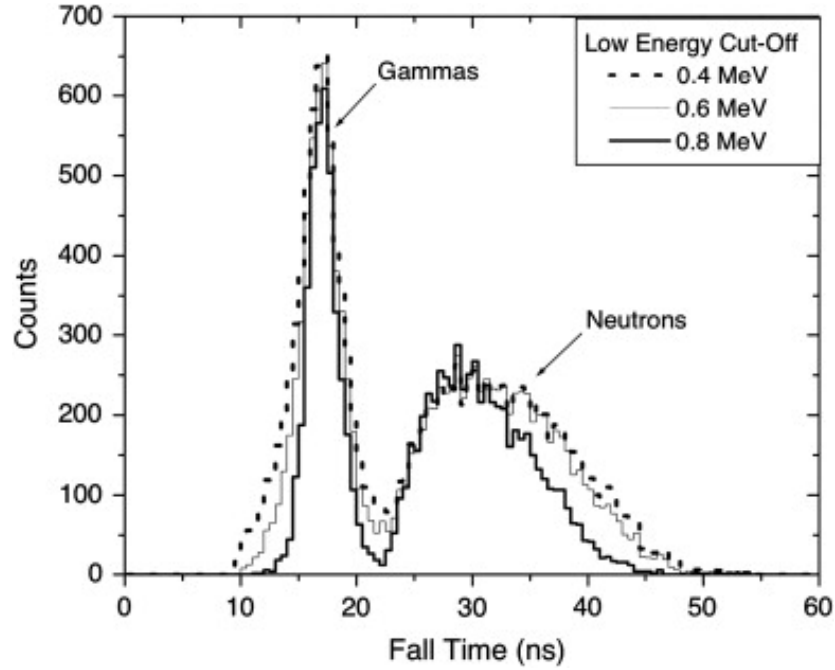


Figure 5.3: The γ -rays produce narrow pulses distinctly different than the neutrons (broad pulses) [100].

upper level threshold and thus is counted as an event. Since the reset pulse amplitude is close to the upper threshold, it appears into the spectrum at higher channels. Since the base-line voltage keeps fluctuating the reset pulse causes a smooth bumpy feature.

During discharges #27465, 27491, 27467, we observed that the detector tends to saturate when the total neutron flux is $\gtrsim 1.5 \times 10^{14}$ neutrons/sec. The neutron flux is obtained from the standard neutron diagnostics. The count rate limit for our HX detector is then estimated to be 40-45 kcounts/sec.

As in this work, we conduct our studies in pure ECRH plasma scenarios in which the neutron flux is zero or almost negligible, there is essentially only X-ray emission. In order to avoid reaching the count rate limit, the soft X-ray flux in the energy region 0-15 keV was cut down by implementing a set of Al-filters and lead-pinholes, as discussed in the Section 3.2.2. The pure hard X-ray flux of 40 kcounts/sec on the detector, already corresponds to a too hot plasma which we never practically reached.

5. MEASUREMENTS OF SUPERTHERMAL ELECTRONS

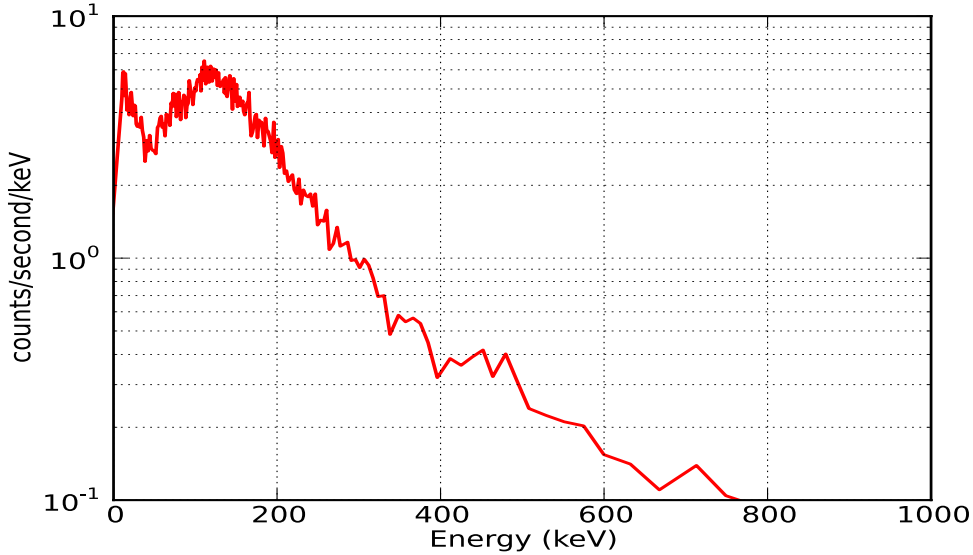


Figure 5.4: A typical neutron induced spectrum (Shot #27453) shows a peak around 150 keV and an extended tail up to 800 keV.

5.2.3 Background measurements

The emission of neutrons from D-D fusion reactions can lead to a significant activation of material in the torus hall by neutron capture reactions. However, most of the activated elements are of a very short half-life (few minutes to few hours). The associated γ radiation is constantly monitored by standard γ -ray counters in the torus hall for the safety norms.

With our new HX diagnostic, it is now possible to perform the spectroscopic measurements of the background activity in the torus hall. For this purpose, the spectra were recorded sequentially every 15 or 30 min over night for up to four days, during which there were no plasma experiments conducted. The total accumulated spectrum is shown in Figure 5.6. Surprisingly, we recorded a strong line feature at 128 keV. In later investigations we noticed that the line decays exponentially, indicating an activation line of some material in the torus hall. Figure 5.7 shows the exponential decay of the 128 keV line intensity. The half-life calculated from the measurements is equal to 2.92 hours. The subplot inside the Figure 5.7 shows the Gaussian shaped line under study.

The line persisted with the same intensity even when the detector vessel was shielded with lead bricks and paraffin wax bricks. This suggested that the origin of

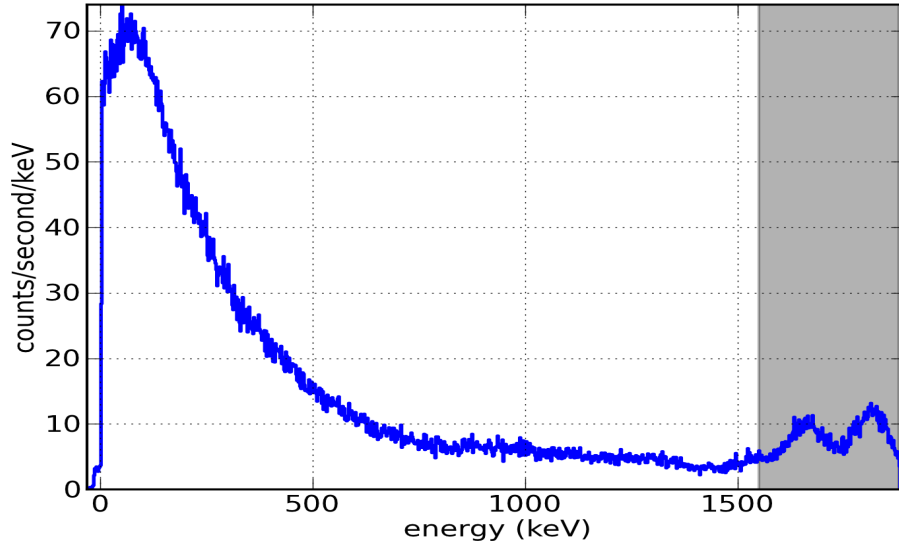


Figure 5.5: The typical spectrum during high count rate. The frequent reset of the preamplifier brings down the baseline level, causing the reset pulse itself to be counted as an amplitude event, which creates a bumpy feature as shown in the shaded region. (shot#27465).

the line has to be in the vicinity of the detector. Since, for a 128 keV photon, before it reaches the detector from outside, it has to traverse through a several centimeters thick metallic shield. After investigating the radiation catalog for every possible element in the vicinity of the detector, we found that the scintillator (Cs) itself was the origin of the line. The stable caesium (Cs-133) nucleus captures a neutron and forms an unstable nucleus (Cs-134m) [101]. Cs-134m decays into Cs-134 by emitting two γ -rays, 128 and 11 keV. The Cs-134m is a short-lived (2.9 hours) isotope [102] as compared to the unstable isotope Cs-134 (2 years) [103].

The 128 keV activation line is found to be in a way helpful rather than a problem, as it can act as an in-situ calibration source. The calibration tests were usually being done over night to collect enough photons. However, if the activation is strong enough then it may interfere with our plasma measurements. During the plasma measurements we estimated the emission rate to be 1-3 counts/sec. Hence it is of no concern for our measurements of a few seconds long. By making use of the 128 keV line, we estimated the detector resolution to be 13% (at 128 keV). We made use of this line radiation in further tightening the energy-width relation.

In addition to the clear peak at 128 keV, Figure 5.6 also shows the presence of

5. MEASUREMENTS OF SUPERTHERMAL ELECTRONS

two minor peaks at about 450 and 740 keV, respectively. At the moment we do not know the origin of these lines, they are under investigation.

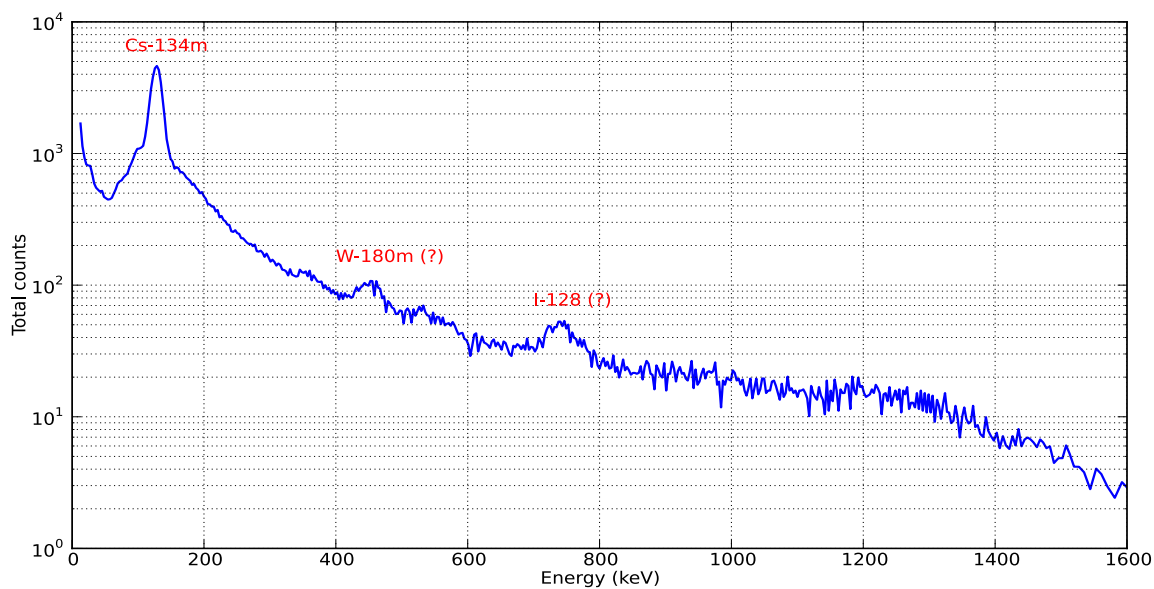


Figure 5.6: The background activity in the torus hall, recorded over night, shows some identified and some unidentified line features.

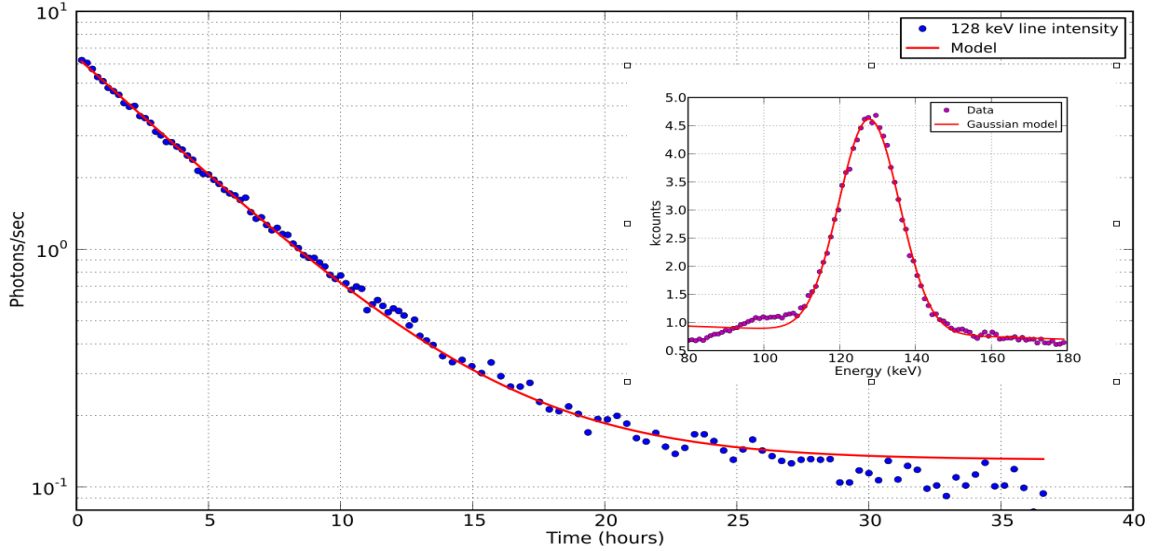


Figure 5.7: The prominent line feature at 128 keV, is later used for calibration.

5.3 Measurements of superthermal electrons

When electron cyclotron resonance waves are launched into the plasma, the waves are damped in the resonance layer heating up the electrons, specifically increasing their velocity in the direction perpendicular to the equilibrium magnetic field (B_{eqm}), as shown by the resonance condition in Equations 1.13 and 1.14. The isotropic Maxwellian velocity distribution shape is modified and a tail of weakly collisional fast electrons is formed in the direction perpendicular to the equilibrium magnetic field B_{eqm} . The accelerated electrons lose their energy and initial direction through radiation or to the other plasma species through collisions. The energetic electrons radiate energy (mostly in X-rays) as a result of passage through the external Coulomb field of the ions. The HXR measurements give the information about the build up of the electron distribution function leading to the insight on the wave absorption.

Significant effects, such as an increase in power absorption and EC current drive, are expected when the absorbed power density exceeds the limit of $\eta = [P_{abs}(\text{MW} \cdot \text{m}^{-3})]/[n_e(10^{19} \cdot \text{m}^{-3})]^2 \gtrsim 0.5$ [21; 104]. This condition is easily satisfied at sufficient low densities and high ECRH power.

As seen in Section 1.4.3, it is only a small part of the distribution function which takes part in the resonance. If there is no excess drag on the electrons, the maximum electron energy obtained by EC absorption is limited by the relativistic mass

5. MEASUREMENTS OF SUPERTHERMAL ELECTRONS

increase which eventually causes the heated electrons to fall out of the cyclotron resonance condition (see Equation 1.16). These resonance electrons slide away from the thermal population to higher energies.

At plasma temperatures of tens of million kelvins, the thermal electrons emit radiation in the soft X-ray range, whereas the non-thermal tail electrons emit radiation even at higher energies, in the hard X-ray range. Measurements of X-ray spectra in the transition range from soft to hard X-rays provide a promising tool for diagnosing the formation and evolution of non-thermal tails induced by ECRH/ECCD.

Furthermore, the hard X-ray measurements provide necessary inputs to the kinetic modeling of the ECRH and ECCD power deposition with combined Ray-tracing and Fokker-Planck codes. It is an important tool in understanding the underlying physics and to make predictions of the heating and current drive efficiency of future ITER- or reactor-like plasmas [105; 106; 107].

The plasma heating and current drive efficiency theory is well tested and supported by extensive experimental investigations [108; 109; 110]. However, there exist some missing parts of the ECCD theory to be investigated in more details, especially the effects related to the superthermal electrons [111].

The superthermal electrons are observed to have strong influence on the efficiency of the EC current drive, as it is demonstrated by various experiments till now [112]. The stability effects on the MHD modes as well as the confinement properties of the plasma are also shown to be influenced by the presence of superthermal electrons in recent experiments [113; 114; 115; 116]. For these reasons the characterization of the superthermal electrons is necessary especially in the ECRH and ECCD experiments.

5.3.1 Plasma discharges at ASDEX Upgrade

For the first time the 10-500 keV hard X-ray spectroscopic measurements were possible at ASDEX Upgrade, opening a spotlight on the energetic electrons. During the high NBI power discharges, the ion temperature is high enough to give rise to a high neutron fluxes (see Section 5.2.1). Noting the influence of high neutron fluxes on the HX detector, the experiments were required to be conducted without NBI, in order to avoid deterioration of the measured X-ray spectra by neutrons and neutron induced gamma events in the detector. For this reason, special ECRH plasma discharges were

5.3 Measurements of superthermal electrons

proposed to be conducted at ASDEX Upgrade. Along with the proposed shots, measurements were also performed during several ‘piggyback¹’ plasma discharges. A list of selected discharges spanning over a range of ECRH powers and densities are classified accordingly, as shown in Table 5.1. In the subsequent sections, we describe the properties of the non-thermal electrons during these selected discharges.

Table 5.1: List of selected discharges at ASDEX Upgrade, spanning over different ECRH powers and electron densities.

$P/(\langle n_e \rangle / [\times 10^{13}])$ (MW · cm ⁻³)	shot no.	$\langle n_e \rangle (\times 10^{13})$ (cm ⁻³)	P (MW)	I_p (MA)	B_t (T) (T)
2.113	27761	1.31	2.769	1.002	-2.519
1.278	27698	1.69	2.161	1.001	-2.613
1.268	27763	2.22	2.816	1.001	-2.520
0.601	27771	4.27	2.567	1.003	-2.535
0.438	27694	1.42	0.622	1	-2.520
0.420	27764	1.6	0.673	1	-2.619
0.420	27766	1.6	0.672	1	-2.519
0.379	27695	1.65	0.626	1	-2.515
0.295	27681	2.22	0.656	1	-2.518
0.291	27682	2.21	0.645	1	-2.518
0.282	27680	2.23	0.627	1	-2.518
0.162	27683	3.99	0.647	1	-2.518

¹Piggyback experiments are the ones which are proposed by somebody else and on which second parties are allowed to passively perform measurements.

5.4 Evolution of the non-thermal distribution function

At the resonance layer the thermal electrons with velocities satisfying the mildly relativistic resonance condition, are constantly pushed to higher energies. The collisional drag on these fast electrons becomes insignificant. The tail of the non-thermal electrons starts evolving as more power is constantly pumped into the plasma. This is observed prominently in the two selected discharges #27698 and #27761.

One of the measurements with a distinct non-thermal tail formation during the discharge #27698 is shown in Figure 5.8. The full power of ECRH (2.1 MW) was maintained constantly from 1-4 sec, referred as the flat-top region. The power was injected at a small toroidal angle $\theta_{tor} = +5$ deg. Figure 5.8 shows the variation in spectral slope, where the spectrum is averaged over one second intervals after heating starts at $t = 1$ s. The spectral tail extends up to 120 keV, i.e., $10 \times$ the thermal electron temperature (T_{th}). The spectrum marked (in black) recorded in the 5-5.1 sec interval is when the heating is switched off, and shows the fast loss of the non-thermal electrons within 100 msec.

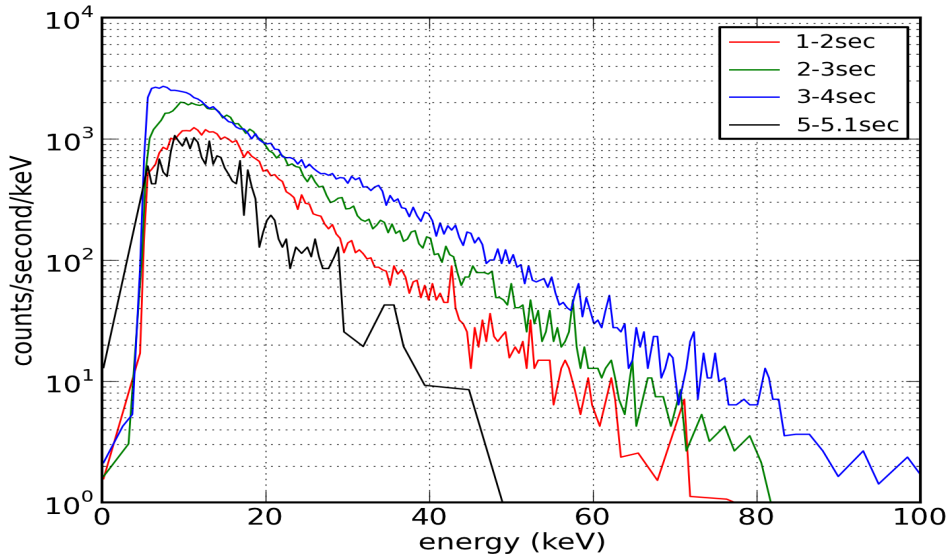


Figure 5.8: Shot#27698: The hard X-ray spectral evolution with time. The ECRH power of 2.1 MW is maintained between 1-5 sec, at a constant electron density of $1.6 \times 10^{13} \text{ cm}^{-3}$.

At lower densities, less particles share the input power, in turn the spectrum extends to higher energies. The quantity $P / \langle n_e \rangle$, roughly telling the power available

5.4 Evolution of the non-thermal distribution function

per particle, is quoted in Table 5.1. During the equilibrium the lose of energy is balanced with the high energy electrons freshly pumped in. At this moment the tail remains roughly at the same slope.

In the discharge #27761, the ECRH power is increased in four steps each of 0.6 MW every half a second. The density is slightly lower than in #27698, and the tail is accordingly observed to be extended even further up to 140 keV. The spectral tail evolution observed during #27761 is shown in Figure 5.9.

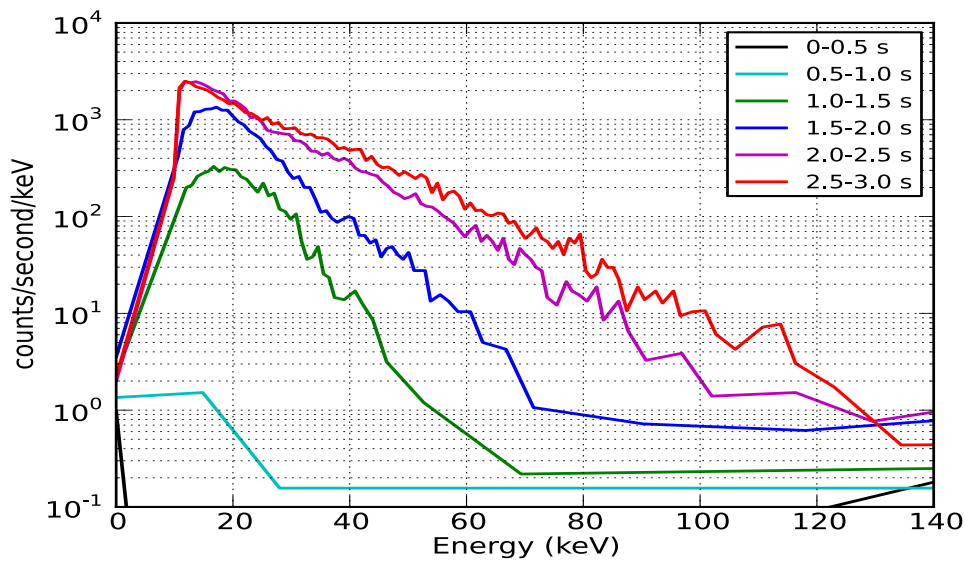


Figure 5.9: Shot#27761: The hard X-ray spectral evolution with time. The ECRH power increases in steps of 0.6 MW every half a second between 1-3 sec, at a constant electron density of $1.3 \times 10^{13} \text{ cm}^{-3}$.

In order to characterize the spectra, a simple model is constructed as described in the following section.

5.5 Spectral modeling and fraction of superthermal electrons

Three distinct methods are used in order to analyze the observed spectra. First, a direct Fokker-Planck modeling for the given discharge is performed (Section 5.5.1). Second, the IDA¹-profiles based thermal bremsstrahlung model was applied to the thermal emission (Section 3.7.3). Third, a simple bi-Maxwellian model (Section 5.5.2) was developed which consists of two components: the thermal part which is the same as in the previous IDA-profile based model, and a non-thermal part which is assumed to be of a Maxwellian shape with higher temperature.

The first method, the Fokker-Planck numerical model is the closest representation of the plasma processes and hence gives a better insight of what is happening inside the plasma. However it is not always possible to perform the Fokker-Planck calculations for the various different plasma scenarios. In such cases the observed hard X-ray spectra are characterized by a model which assumes a certain shape of the underlying non-thermal electron distribution function. In Section 5.5.1 below, the Fokker-Planck code based model is described and in the following Section 5.5.2 the bi-Maxwellian approach in modeling the spectra is described.

5.5.1 Fokker-Planck code estimates

For a given set of plasma discharge parameters, first the power deposition is calculated by the ray tracing code TORBEAM. The effects of the power deposition on the electron distribution functions are calculated with the Fokker-Planck code (for details refer to Section 1.5). The numerical electron distribution functions corresponding to the selected plasma scenarios were provided by O. Maj (Max Planck Institute for Plasma Physics, Garching). The numerical electron distribution function as a function of (ψ, p, θ) , is described in Equation 1.19

$$f_e \equiv f_e(\psi, p, \theta), \quad (5.1)$$

where, ψ labels the normalized magnetic flux surface, p is the normalized electron momentum, and θ is the pitch angle (angle between \mathbf{p} and \mathbf{B}_{eqm}).

¹Integrated Data Analysis code

5.5 Spectral modeling and fraction of superthermal electrons

A Python based post processing module called *PhotonSpec* is developed to translate the numerical electron distribution function (EDF) into the hard X-ray photon emission spectrum.

Since our single line of sight detector cannot differentiate between the electrons with parallel and perpendicular momentum, we obtain the EDF by integrating over the pitch angle

$$f_e(\psi, p) = \int_0^\pi f_e(\psi, p, \theta) d\theta. \quad (5.2)$$

The single speed bremsstrahlung emission formula derived in Equation 1.25 is rewritten below with the substitution $v = p'/m$ and $E = \hbar\omega$ as

$$\frac{dW(p, E)}{dV dt dE} = \frac{16e^6}{3c^3 m} \frac{1}{p'} n_e n_i Z^2 g_{ff}(p, E) \frac{10^{-7} \cdot 1.6 \times 10^{-19}}{\hbar} \quad (5.3)$$

in units (J/s/cm³/eV).

In order to obtain the power radiated from the non-thermal electrons, the distribution function in Equation 5.2 is integrated over the single momentum bremsstrahlung emission in Equation 5.3, and using the normalized momentum $p = p'/mc$

$$S(\psi, E) = \frac{dW(\psi, E)}{dV dt dE} = \frac{\int_{p_{min}}^\infty \frac{dW(p, E)}{dV dt dE} f_e(\psi, p) p^2 dp}{\int_0^\infty f_e(\psi, p) p^2 dp} \quad (5.4)$$

in the units of (J/s/cm³/eV), where the lower limit $p_{min} = \sqrt{2mE}/mc$ obtains the energy dependence of the photon spectrum.

Using the relation $\rho = \sqrt{\psi}$, and substituting $Rd\rho = \frac{Rd\psi}{2\sqrt{\psi}}$, where R is the semi-minor horizontal radius (50 cm) for ASDEX Upgrade, the simulated spectrum $S(\psi, E)$ is then integrated over the line of sight

$$S(E) = \int_{\psi_{min}}^{\psi_{max}} S(\psi, E) d\psi \quad (5.5)$$

The simulated spectrum $S(E)$ is then convolved with the detector response matrix to estimate the spectrum as received by the detector (similar to Equation 3.4)

$$D(E_j) = \int_{E_{i,min}}^{E_{i,max}} S(E_i) \eta(E_i) R(E_i, E_j) dE_i, \quad (5.6)$$

where, $\eta(E_i)$ is the absorption-filter function and $R(E_i, E_j)$ is the detector response matrix, and E_i is the energy of the photon incident and the E_j is that of recorded in the detector.

5. MEASUREMENTS OF SUPERTHERMAL ELECTRONS

The estimated spectrum $D(E)$ (the suffix ‘j’ is dropped for convenience) is then compared with the measured spectrum $C(E)$.

The fraction of non-thermal electrons (δ_{FP}) is calculated from the Fokker-Planck simulated electron distribution function by integrating the distribution function over the electron energies 15 keV and above.

The dynamics of the non-thermal electrons are closely predicted by the Fokker-Planck simulations using the parameters of given plasma discharges. Due to some limitations in the code, it cannot be applied properly in the cases of complex the ECRH launching geometries. Currently, it was possible to reconstruct only some selected plasma discharges.

5.5.2 Bi-Maxwellian model

In order to understand the dynamics of the non-thermal electrons in many of the diverse plasma scenarios, the plasma emission is represented by a bi-Maxwellian model.

The thermal bulk of the plasma is well represented by a Maxwellian distribution. The shape of the Maxwellian distribution towards higher energies is an exponential decay (see Equation 1.27) and in a logarithmic scale the exponential tail becomes a straight line and is characterized by its slope (which represents the bulk temperature). The thermal electrons slide away from the Maxwellian tail to form a non-thermal tail, so that in this process the initial relatively steeper slope is modified to become flatter. These non-thermal electrons can be characterized by another slope (which represents the tail temperature). The non-thermal hard X-ray tail is always observed to have an exponential-decay form, with the slope different from that of the thermal electrons. The bi-Maxwellian model, as described below, is realized to be not too far from the real distribution function.

The thermal bulk plasma emission is well modeled by the IDA ($n_{e,b}, T_b$) radial profiles, as described in Sections 3.7.3 and 3.7.4. The thermal emission model integrated over the line of sight and convolved with the detector response function, as shown in Equation 3.4 is re-written

$$F_b(E_j) = \int_{E_{i,min}}^{E_{i,max}} B(E_i)\eta(E_i)R(E_i, E_j)dE_i, \quad (5.7)$$

5.5 Spectral modeling and fraction of superthermal electrons

where, $\eta(E_i)$ is the absorption-filter function and $R(E_i, E_j)$ is the detector response matrix, and E_i is the energy of the photon incident and the E_j is that of recorded in the detector.

For the non-thermal electrons, the $(n_{e,s}, T_s)$ radial profiles are unknown, and the emission is obtained by the thermal bremsstrahlung Equation 1.30 integrated over the line of sight (or projected emission), approximately given as

$$B_s(E) = 4.8 \times 10^{-34} Z^2 \cdot [n_{e,s}]_L \cdot n_i \frac{e^{-E/T_s}}{\sqrt{T_s}} \bar{g}_{ff} \quad (5.8)$$

where, $[n_{e,s}]_L$ is the line integrated non-thermal electron density, and T_s is the non-thermal electron tail temperature. The line averaged non-thermal electron density is obtained as $\langle n_{e,s} \rangle = [n_{e,s}]_L / L$, where L is the length of line of sight.

The model B_s is then convolved with the detector response function to obtain F_s in a similar manner as given in Equation 5.7, where suffix ‘b’ stands from thermal bulk electrons and ‘s’ stands for superthermal tail electrons.

A bi-Maxwellian function is obtained as the addition of both Maxwellian shaped thermal and non-thermal models

$$D(E) = F_b + F_s. \quad (5.9)$$

The model $D(E)$ is fitted to the observed data with two free parameters, $\langle n_{e,s} \rangle$ and T_s . The fraction of non-thermal electrons is obtained as $\delta_{bm} = \langle n_{e,s} \rangle / (\langle n_{e,b} \rangle + \langle n_{e,s} \rangle)$.

The quantity T_b is essentially a first-moment of the thermal distribution function and hence represents the bulk temperature. However, the temperature T_s is not truly the moment of the non-thermal distribution function and in that sense not a temperature, but it does scale to the average energy of the underlying true non-thermal distribution function.

The modeled (δ_{bm}) fraction of non-thermal electrons is compared with the simulated value (δ_{FP}) for a few selected cases (see Section 5.5.5).

In Section 5.5.3, we demonstrate the Fokker-Planck modeling of the non-thermal electron distribution function for one of the plasma discharges with low heating power. In Section 5.5.4, we demonstrate a qualitative prediction of the Fokker-Planck calculated non-thermal electron distribution function at high ECRH powers and compare it with the HXR spectrum.

5. MEASUREMENTS OF SUPERTHERMAL ELECTRONS

5.5.3 Modeling non-thermal emission at low ECRH power

The discharge #27764 is at low power (~ 0.6 MW) and a very low electron density, as listed in the Table 5.1. The discharge #27764 provides a simple scenario in order to test the Fokker-Planck estimations.

Figure 5.10 shows the time traces of the main plasma parameters of shot #27764, in which flat-top operation region between 2-4 s is to be noted. The 0.6 MW ECRH power is applied over 1.5-4 s period, and during this period the bulk plasma electron temperature just reaches 3 keV and the electron density remains constant at roughly $1.6 \times 10^{13} \text{ cm}^{-3}$.

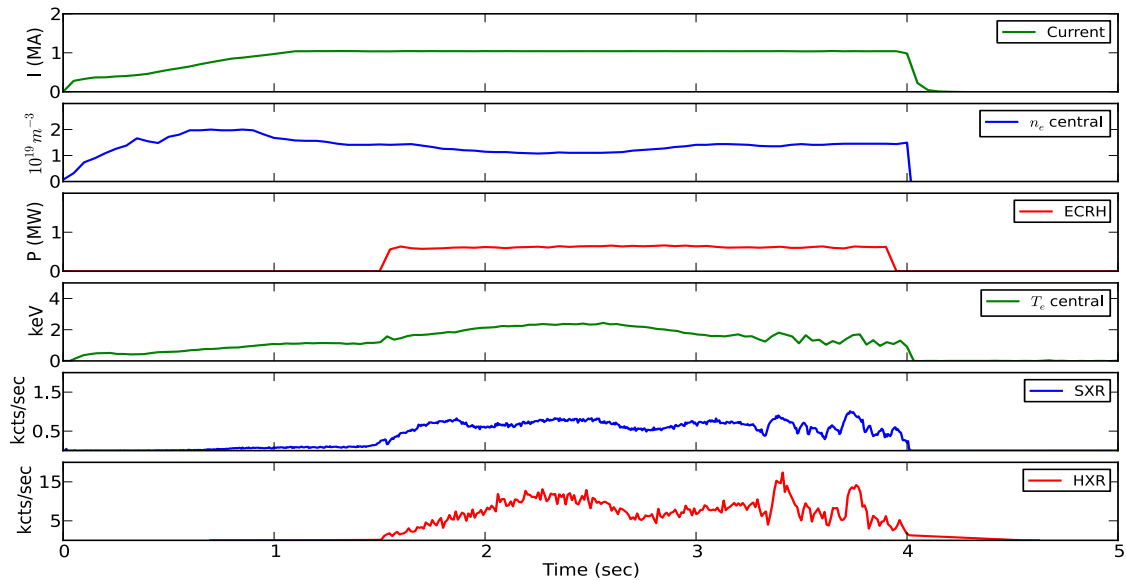


Figure 5.10: Shot #27764. The time traces of the key plasma parameters are shown. The last row shows the time trace of the HXR signal integrated over all photon energies.

The electron distribution function (EDF) is estimated for plasma equilibrium at $t = 3$ s using the Fokker-Planck code. The EDF resolved into the parallel momentum ($p_{\parallel} = p \cos \theta$) and perpendicular momentum ($p_{\perp} = p \sin \theta$) components, and evaluated at fixed ψ , $f_e(p_{\parallel}, p_{\perp})$, is shown in Figure 5.11. Note the deformation in the contours in the anti-parallel direction and in the perpendicular direction. Due to the parallel electric field (E_{\parallel}), the electrons are accelerated in the direction anti-parallel to the plasma current. The deformation in the perpendicular direction is mainly due to the EC waves heating the electrons, forming a non-thermal tail in the perpendicular velocity direction.

5.5 Spectral modeling and fraction of superthermal electrons

It is evident from the Fokker-Planck estimates that the formation of a non-thermal tail is dominantly caused by the E_{\parallel} rather than the ECRH.

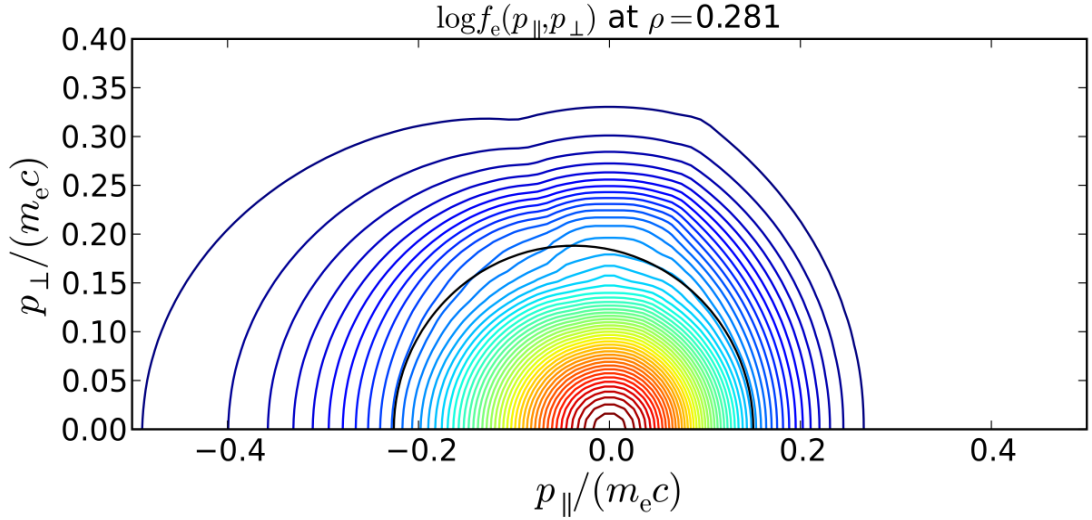


Figure 5.11: Shot #27764. The electron distribution function (equi-momentum contours) as a function of parallel and perpendicular electron momentum, estimated by the Fokker-Planck code. The black curve represents the resonance curve.

The bulk plasma temperature obtained by the IDA profile is $T_{e,b} = 3$ keV at $t = 3$ s. For better statistics on the photon counts, the hard X-ray spectrum is averaged over 2-4 sec. Figure 5.12 shows the comparison between the hard X-ray spectrum measured and the estimated spectrum based on the Fokker-Planck calculated distribution function (FP-model); the spectrum is fitted with a bi-Maxwellian model (red curve) with a tail temperature of 6 keV. It can be seen that at the high energy end, the spectrum deviates from the Bi-Maxwellian model (as formulated in Section 5.5.2), indicating a constantly changing tail temperature.

The FP-model represents the observed spectrum within a factor 2 at the lower energy end. The effect of plasma impurities were not included in the bi-Maxwellian model (Equation 5.8), which may lead to an increase in the model intensity.

The fractions of the non-thermal electrons calculated from both the bi-Maxwellian model, $\delta_{bm} = 2.9$ % (of the electron bulk density), as well as from the FP-model, $\delta_{FP} = 2.7$ %, show a good agreement with each other. The total plasma current contributed by the non-thermal tail as estimated from the Fokker-Planck calculations

5. MEASUREMENTS OF SUPERTHERMAL ELECTRONS

is ~ 12 kA. The magnitude of the current is minute as compared to the inductive plasma current (1 MA), but it is strong enough to locally modify the magnetic field geometry and affect the local MHD activity. At high EC resonance heating powers, the non-thermal tail is even more prominent and can cause even stronger influence on the local MHD activity.

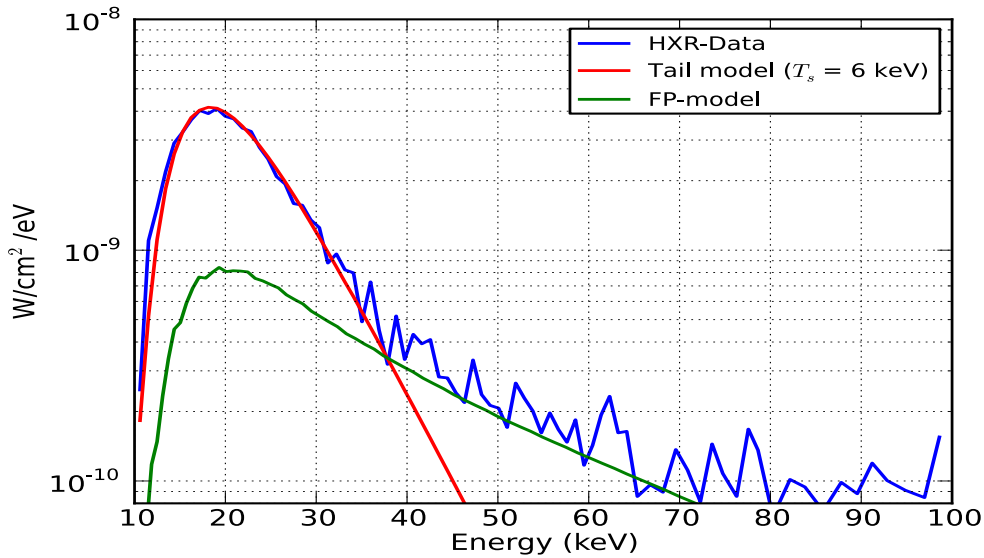


Figure 5.12: Shot #27764. Comparison between the bi-Maxwellian (red) model (with tail temperature of 6 keV) and the Fokker-Planck estimation (green).

The Fokker-Planck calculated non-thermal electron distribution function in the low-power low-density regime is proven to be matching with the observations and supports the current understanding of the formation of non-thermals.

5.5.4 Modeling non-thermal emission at high ECRH power

Two high power discharges (#27761 and #27698) were executed in order to investigate the nature of the non-thermal electrons, see Table 5.1 for the plasma parameters. During the shot #27761 the ECRH heating power is increased in steps of 0.6 MW every half a second. As an effect, the spectral hardening is seen in Figure 5.9.

The Fokker-Planck calculations were performed for the shot #27761 in order to test the non-thermal dynamics at high ECRH powers.

At present TORBEAM code is not capable of incorporating more than one gyrotron sources, since it requires taking into account the beam geometries of different

5.5 Spectral modeling and fraction of superthermal electrons

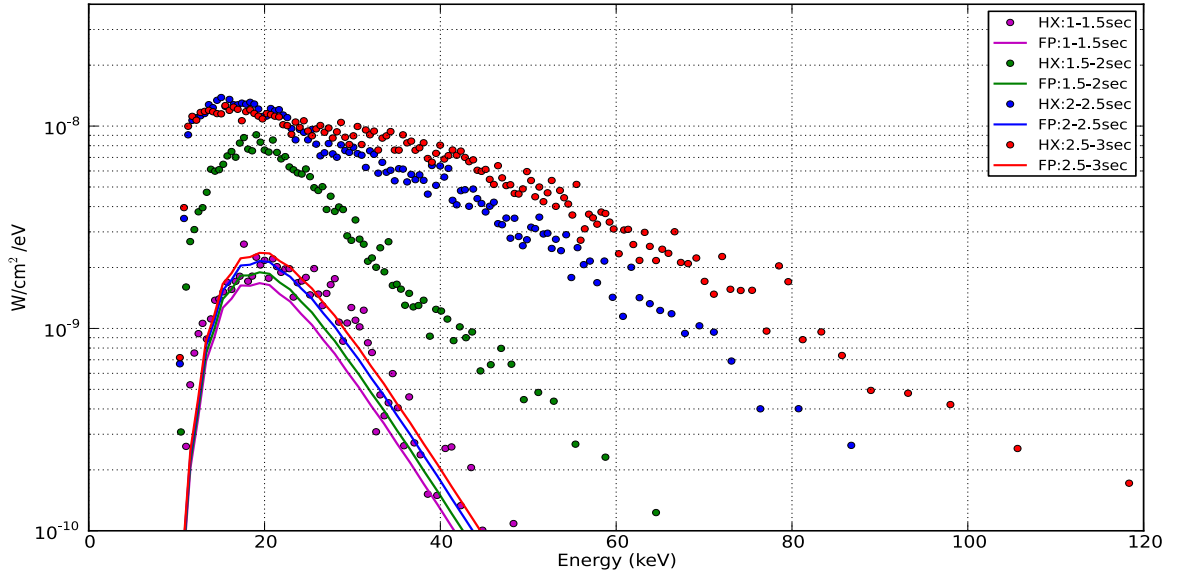


Figure 5.13: Shot #27761. HX spectrum compared with the spectrum calculated by the Fokker-Planck code without parallel electric field.

gyrotron sources, depositing energy at more than one equilibrium surfaces. This will be resolved in the near future. At present the calculation of the electron distribution function is realistic only for those plasma discharges which have one gyrotron heating, as in the case #27764 (Section 5.5.3). This limits us to treat only the low power discharges, but for most of the non-thermal physics it is the high power plasma scenarios which are of more interest.

To have at least an qualitative understanding of the high power discharges, the Fokker-Planck calculations are performed by assuming that the total power of several gyrotrons is launched by a single gyrotron at a single resonance surface. Although this assumption would overestimate the plasma heating at one equilibrium surface and underestimate it at the other equilibrium surfaces, and will not depict a realistic plasma scenario, it still provides an important input on the dynamics of the non-thermal electrons at high ECRH powers.

The measured spectrum is compared with the Fokker-Planck estimated spectrum at each power step, without and with including the inductive E_{\parallel} field in the calculations in Figure 5.13 and 5.14 respectively.

Figure 5.13 shows the FP-model (smooth lines) corresponding to the increase in pure ECRH power, without the effect of the inductive parallel electric field E_{\parallel} . It can

5. MEASUREMENTS OF SUPERTHERMAL ELECTRONS

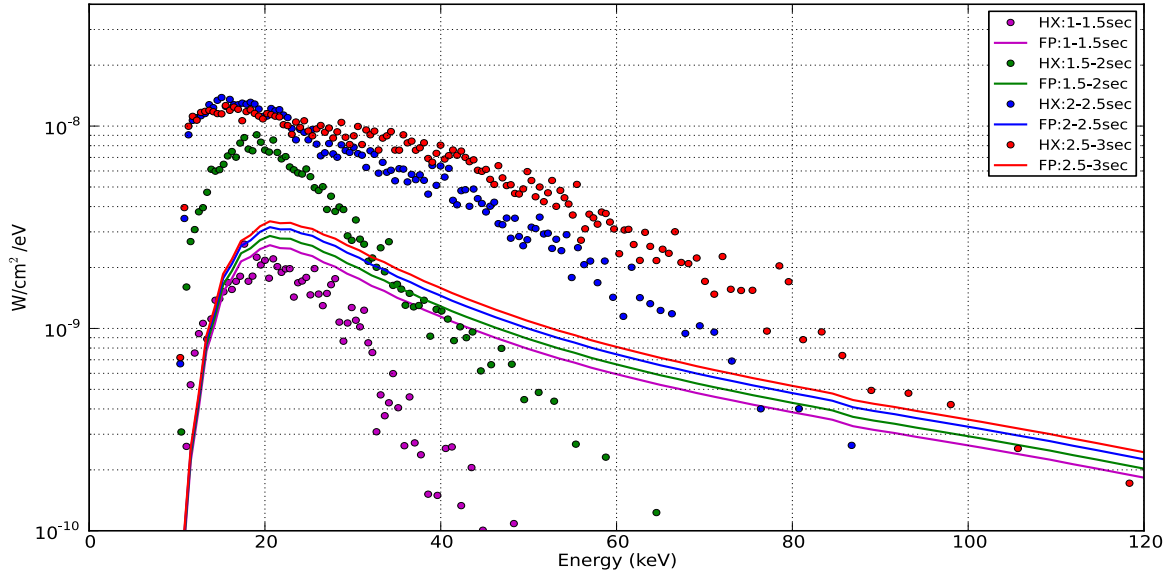


Figure 5.14: Shot #27761. HX spectrum compared with the spectrum calculated by the Fokker-Planck code with parallel electric field 0.09 V/m.

be seen that the Fokker-Planck calculations does not predict an extended non-thermal tail as an effect of pure ECRH.

The formation of the extended tail is evident as an effect of E_{\parallel} as shown in Figure 5.14. However none of the simulations explain the hardening of the spectral slope as well as the order of magnitude enhancement in the total emitted power. As already mentioned, the Fokker-Planck calculations does not depict the true plasma scenario, but it does represent the measurements qualitatively. Also, it should be noted again that particularly at high ECRH powers, impurity effects can decrease the discrepancy between the measured intensities and the predicted models.

In order to quantify the measurements during this high power ECRH scenario, the hard X-ray spectrum is characterized with a bi-Maxwellian model, shown in Figure 5.15. The underlying electron-tail temperature (T_s) increases from 5 keV to 23 keV with the increment in the heating power from 0.6 to 2.8 MW. The bulk thermal temperature (T_b), obtained by the IDA profiles, increases from 2.5 to 10 keV. The non-thermal tail is observed to be extended upto $10 \times T_b$. The fraction of non-thermal electrons estimated from both the Fokker-Planck calculations and the bi-Maxwellian model are close to the value of $\sim 2\%$ of the bulk electron density (see Section 5.5.5).

The measurements show that the pronounced non-thermal tail generated is may

5.5 Spectral modeling and fraction of superthermal electrons

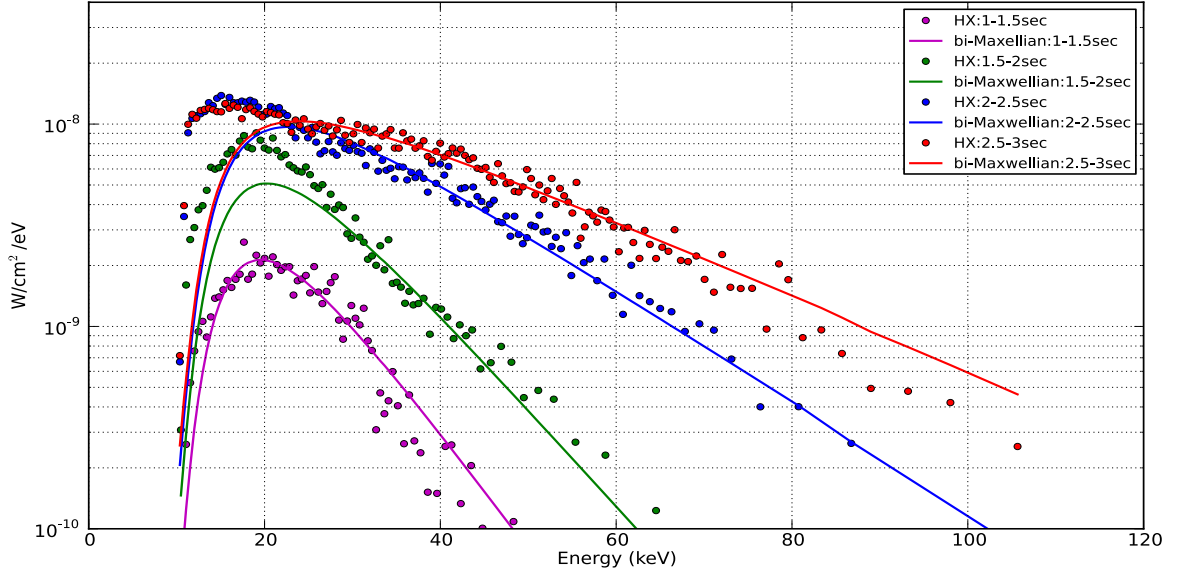


Figure 5.15: Shot #27761. HX spectrum fitted with the bi-Maxwellian model. The tail temperature is varying from 5 keV to 23 keV.

be due to both, the strong ECRH causing the perpendicular non-thermal tail as well as the E_{\parallel} causing the parallel non-thermal tail. As this non-thermal electron population is less collisional with the bulk ion population, it creates an asymmetric resistivity in the parallel direction, leading to a net parallel current density J [32]. It is important to note that the current density J is proportional to the *total* velocity of the electrons and not just the parallel velocity. Hence, such an enhanced perpendicular non-thermal tail can contribute significantly to the total non-thermal plasma current. More efforts are needed to simulate the exact energetic of the EC wave interaction with the particles which lead to such an extended observed tail. It will remain as a future scope.

5.5.5 Density and power dependence

The focused EC beam deposits its energy in a very narrow resonance region, leading to a very high power density P_{abs} ($\text{MW} \cdot \text{cm}^{-3}$). The local electron distribution function is strongly affected by the higher power densities. The power density P_{abs} is estimated by the ray-tracing code TORBEAM. Instead, the ratio of total power to the bulk electron density, $P/\langle n_{e,b} \rangle$, is estimated which gives an average energy available per electron in a unit volume.

5. MEASUREMENTS OF SUPERHERMAL ELECTRONS

The plasma discharges were selected such that they span over the range of values of $P/\langle n_{e,b} \rangle$. The selected discharges are - #27761, #27698, #27764, #27771, #27694, #27695, and #27683 (see the Table 5.1 for more details). Due to the limited experimental time at ADSDEX Upgrade, only a few high power discharges were feasible. Each of the listed discharges were analyzed by fitting the bi-Maxwellian model (see Appendix C). The fraction of non-thermal electrons and the tail temperature are calculated from the model.

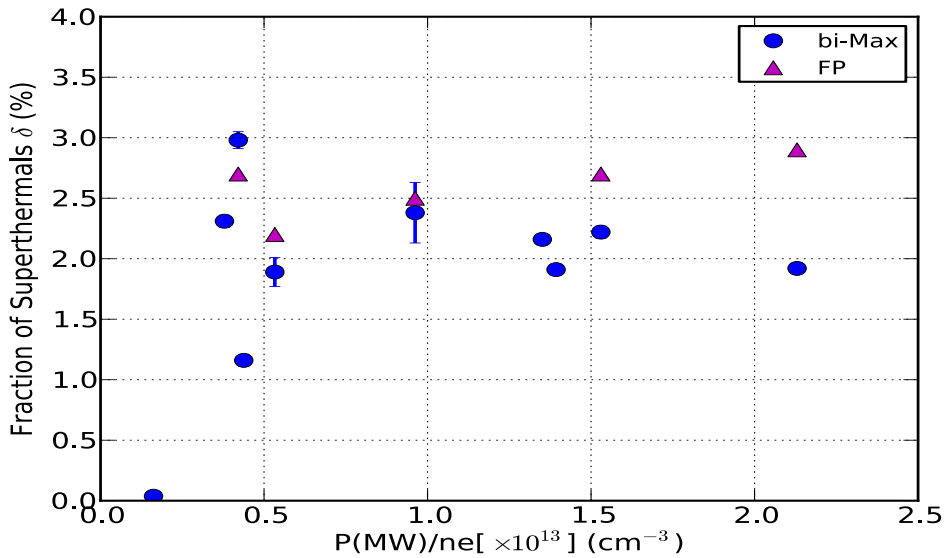


Figure 5.16: The fraction of non-thermal electrons as a function of $P/\langle n_e \rangle$ (See text for more details).

Figure 5.16 compares the calculated fraction of non-thermal electrons from both the bi-Maxwellian (blue circles) and the Fokker-Planck (magenta triangles) models plotted against the $P/\langle n_{e,b} \rangle$. Interestingly, the fraction of non-thermals is observed to be constant around 2 % of the bulk electron density. However, Figure 5.17 shows the average energy of the non-thermals (i.e. the tail temperature, in red circles) increases significantly with the $P/\langle n_{e,b} \rangle$ in contrast to the bulk electron temperature (green triangles). Note that the tail temperature T_s is the characteristic of the electron distribution function and *not* just the slope of the photon spectrum. Hence a population of ~ 2 % of the bulk electrons with higher average energy explains the enhanced X-ray emission.

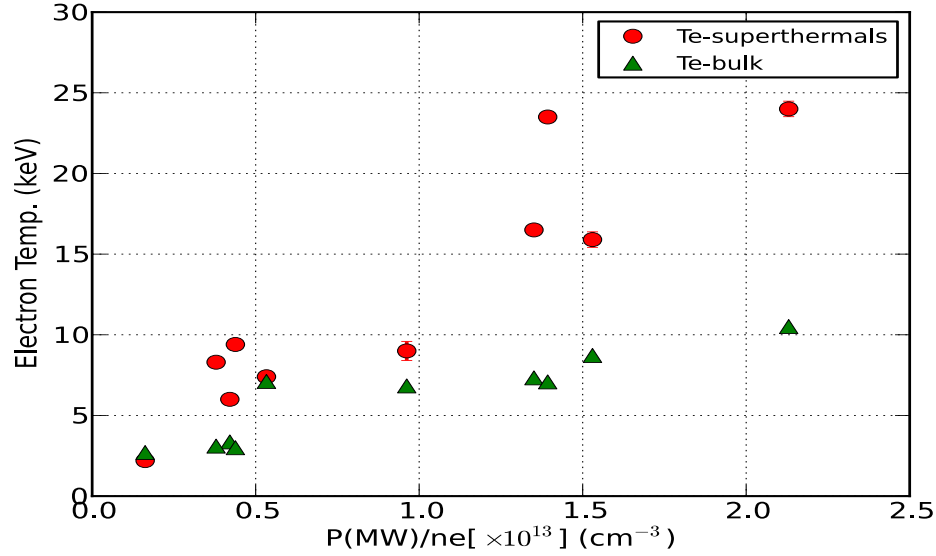


Figure 5.17: The non-thermal electron temperature obtained by the bi-Maxwellian model and the peak bulk electron temperature are plotted against $P/\langle n_e \rangle$ (See text for more details).

The question that arises further is: why does the non-thermal population not increase? It can be qualitatively understood as following; firstly, it is only a small fraction of thermal electrons which satisfy the perpendicular resonance condition (Equation 1.16) and secondly, they fall out of the resonance condition once they have gained sufficient energy. Therefore, eventually a saturation-plateau in the electron distribution function is created because of the depletion of resonant bulk electrons. The amount of energy absorbed by the initial resonant electrons depends on the power available per particle ($P/\langle n_{e,b} \rangle$) and that explains the spectral hardening as a function of $P/\langle n_{e,b} \rangle$.

5.6 Other important observations

5.6.1 Extreme hard X-ray emission and runaway electrons

In the previous section we already saw the non-thermal tail extending up to 100 keV, i.e., 10 to 20 times the thermal electron temperature. In some of the plasma scenarios we record the hard X-rays as high as 500 times the thermal electron temperature. The radiation is recorded in the range 100 to 500 keV, referred to as *extreme* hard X-rays.

5. MEASUREMENTS OF SUPERTHERMAL ELECTRONS

- At high ECRH powers

Figure 5.18 shows the typical spectral shape of the extreme hard X-rays recorded. The spectra are plotted for the three different discharges #27761, #27698, and #27771 with the ECRH powers 2.7, 2.1, and 1.8 MW respectively. The intensity of the extreme-HX is one to two orders of magnitude weaker but significantly higher than the background level. Due to a very few counts in total, we carry out only a qualitative analysis.

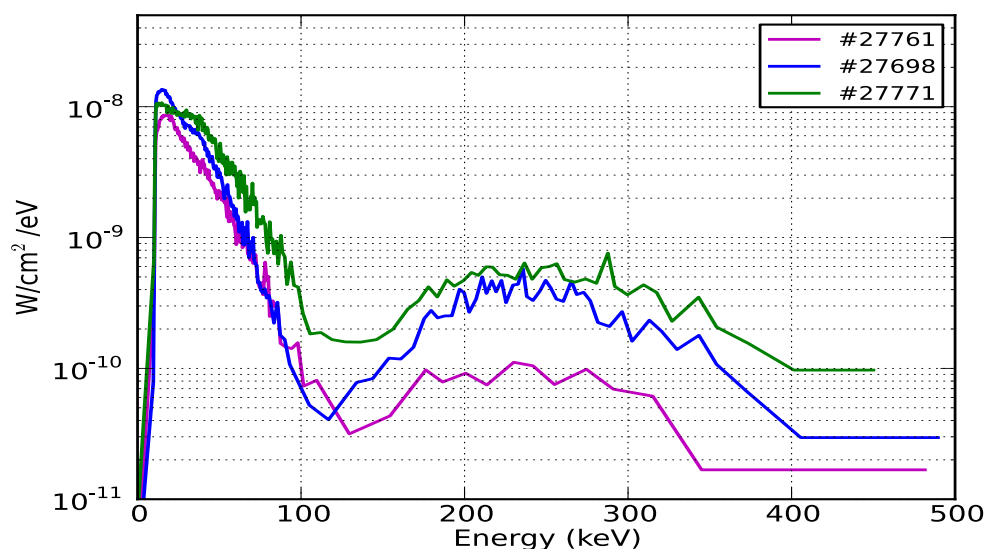


Figure 5.18: Extreme hard X-ray emission measured between 100 - 500 keV.

It is suspected that at such high powers and low densities, the ECRH provides a synergetic effect by the formation of non-thermal tails which ease the formation of slideaway or runaway electrons by the E_{\parallel} [114; 117; 118] (see Section 1.4.1). The runaway electrons carry energy from several keVs to a few tens of MeVs. These electrons can radiate energy as high as their kinetic energy. Hence the hard X-ray radiation might be the signature of the runaway electrons.

- At low ECRH powers

The extreme-HX emission is, however, not a feature observed only during high power discharges. In the two cases discussed below, shots #27766 and #27695 with the ECRH power as low as 0.6 MW, a prominent extreme-HX emission is still observed.

5.6 Other important observations

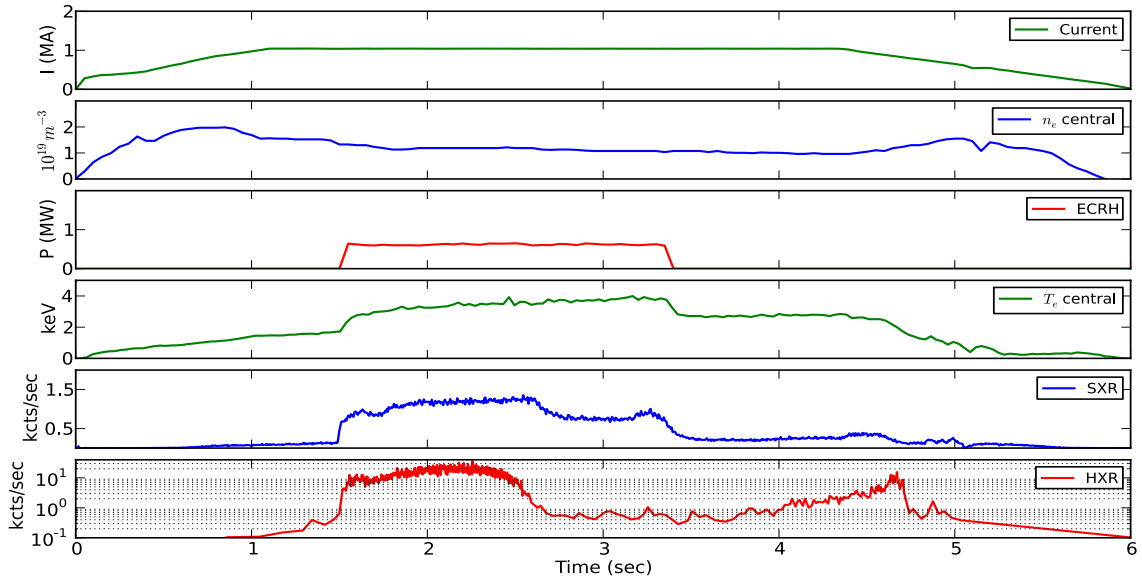


Figure 5.19: Shot #27766. Time traces of important plasma parameters. The last row shows the total HX count rate.

In an interesting first case, discharge #27766, a pure extreme-HX emission is recorded. Figure 5.19 shows the time traces of important plasma parameters. The ECRH heating is turned on between 1.5-3.4 s (3^{rd} row). The thermal bulk temperature is below 4 keV. After the ECRH is turned off, the total HX count rate (last row) shows a steady enhancement up to 4.7 sec and a sudden fall.

In Figure 5.20 the total HX count rate is decomposed into HX (blue) and extreme-HX (red) energies and plotted against time. After the ECRH heating is stopped at 3.4 s, the emission between 0-50 keV completely disappears, whereas that between 50-500 keV enhances significantly. The process is also evident from the energy spectra of the total counts integrated over 1 sec time bins, plotted in Figure 5.21. The spectra in Figure 5.21 are plotted in log-log scale to point out the shape of both the HX and extreme-HX spectra.

The origin of the hard X-rays is clearly due to the non-thermal electrons (since the thermal electron temperature is under 4 keV during 1-5 sec).

It is suspected that the origin of the extreme-HX emission is due to the runaway electrons. After the ECRH is turned off, the bulk electron temperature falls (seen in 3^{rd} row Figure 5.19). As a result the plasma resistivity increases,

5. MEASUREMENTS OF SUPERTHERMAL ELECTRONS

subsequently causing an increase in the loop voltage. The non-thermal electrons already generated during the ECRH phase act as a population seed population, which in response to the increased loop voltage accelerate further to even higher energies until they are lost [117; 118].

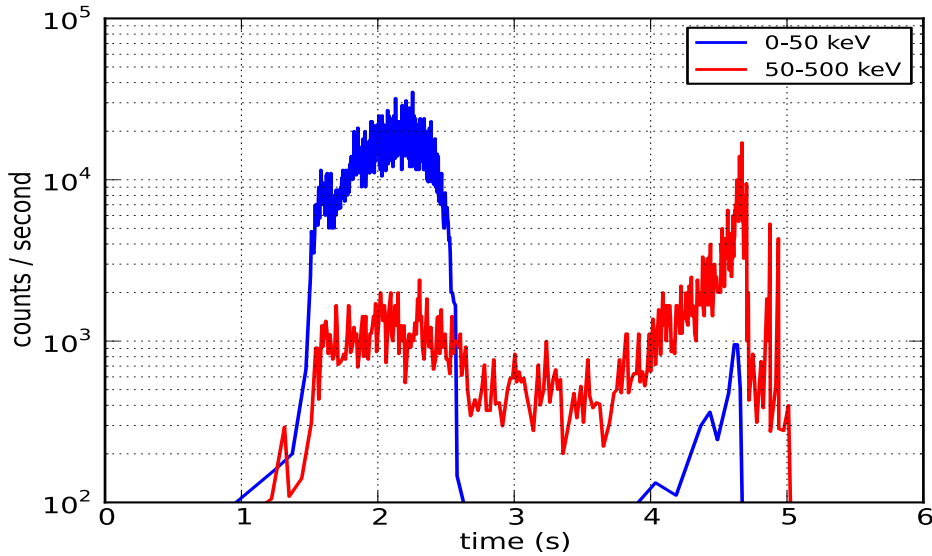


Figure 5.20: Shot #27766. Time traces of the X-ray emission decomposed into 0-50 keV and 50-500 keV energy ranges.

Although the ASDEX Upgrade shots are not exactly reproducible, an extreme hard X-ray enhancement is recorded also during a similar shot #27695. Figures 5.22 and 5.23 show the corresponding time traces and the spectra.

All of these discharges were the part of piggyback experiments and were not intended to study such an effect. Nevertheless, a further investigation is needed, and is extremely important, to understand clearly the cause and loss of the runaway electrons in similar cases. It will remain as a part of the future work.

5.6.2 The saw-tooth like oscillations in the hard X-rays

In various tokamak plasma operational conditions, in the center of the hot plasma, it is well known that the core plasma constantly undergoes reorganization in a periodic manner. During this process the core slowly heats up until it becomes unstable, causing the loss of heat from the center to the surrounding surfaces as a heat pulse.

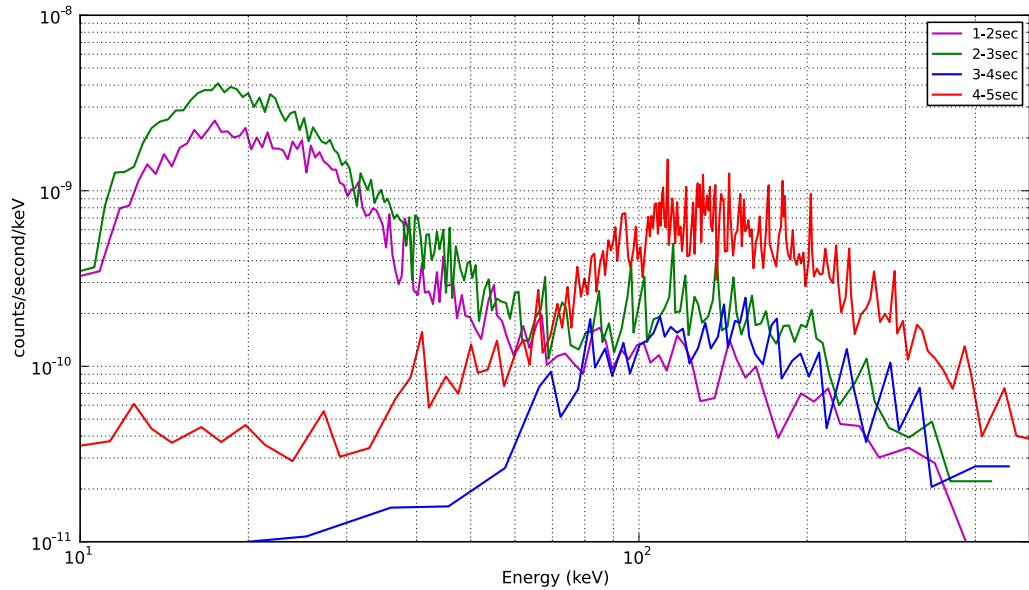


Figure 5.21: Shot #27766. The hard X-ray spectral evolution. The enhanced extreme hard X-ray emission before (magenta and green) and after (blue and red) the plasma heating turned off.

This causes a sawtooth like shape in the soft X-ray emission from the center and inverted shape from the surrounding surfaces. It is now known that the underlying process of this sawtooth instability is a so-called internal kink mode driven by the plasma current by which the magnetic surfaces inside the $q = 1$ surface are displaced causing a magnetic re-connection process [5].

During the magnetic re-connection process the energy stored in the magnetic field is suddenly released in the form of kinetic energy to the plasma particles. This process is believed to give rise to non-thermal electrons with energies in the order of 100-500 keV [119]. The magnetic re-connection and generation of non-thermal particles is observed in many astrophysical situations such as the earth's magnetosphere, solar coronal mass ejections, and γ -ray bursts [120]. The generation of non-thermal electrons in connection with the sawtooth oscillations has been observed in many tokamak experiments [121; 122; 123; 124].

In the discharges #27761, one of the most exciting feature was observed. After eliminating the photons between 0-30 keV (thermal range) energy, the hard X-ray signal is observed to be correlating with the sawtooth oscillation period. Figure 5.24, top curve shows the soft X-ray (1-10 keV) signal from one of the standard bolometric type SXR camera. The detector J-047 is chosen as its line of sight is close to that

5. MEASUREMENTS OF SUPERTHERMAL ELECTRONS

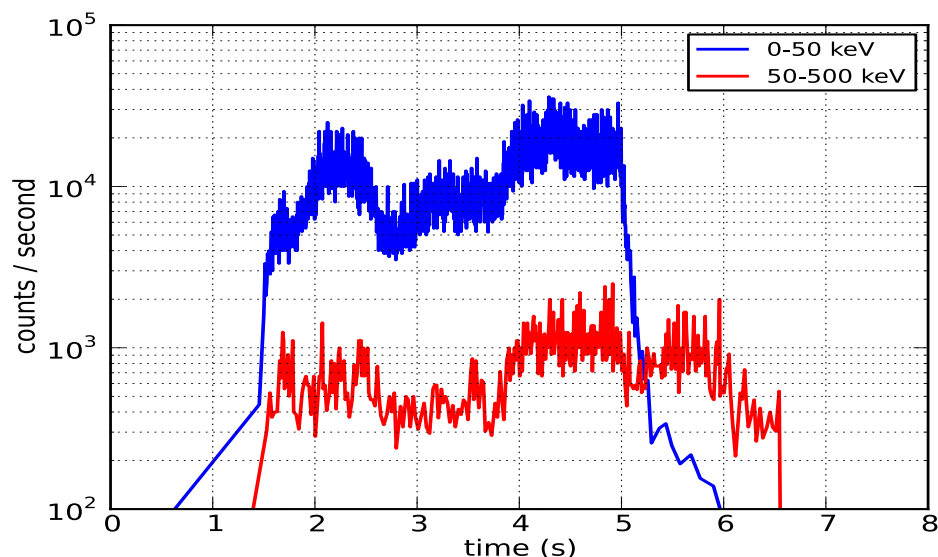


Figure 5.22: Shot #27695. Time traces of the X-ray emission decomposed into 0-50 keV and 50-500 keV energy ranges.

of our HX detector. Figure 5.24, bottom curve shows the count rate of hard X-rays integrated over 30-100 keV. Although, the temporal resolution of the HX signal is not as good as in the SX signal, one can clearly see that during each sawtooth crash (with period ~ 90 ms) the HX count rate spikes up, showing the generation of non-thermal electrons with energies 30 keV and higher. We observe that the intensity of the sawtooth crash generated non-thermal electrons is considerably weak (up to 25% enhancement) and it needs a controlled experimental investigation.

5.6 Other important observations

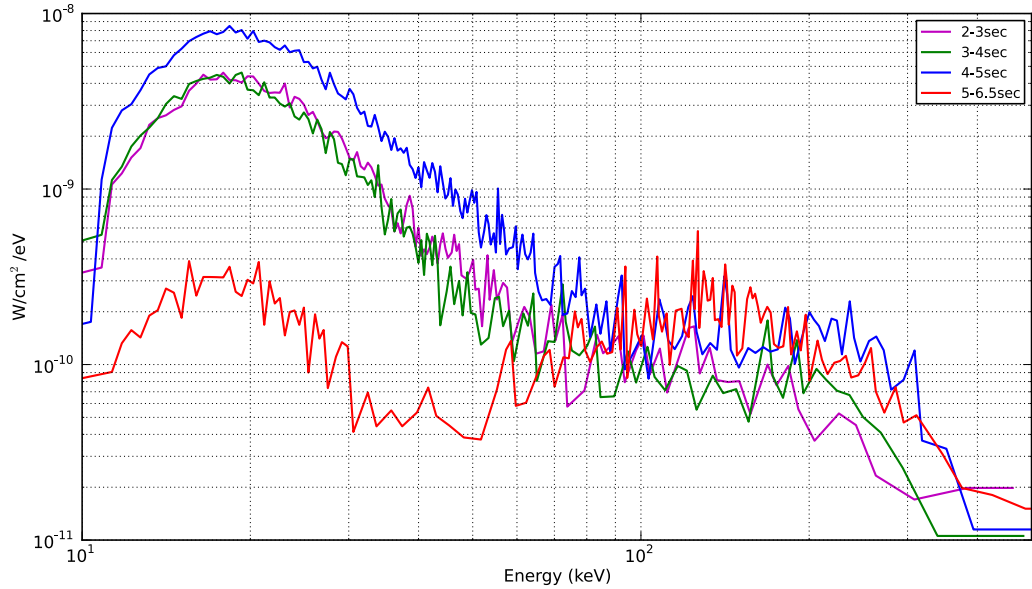


Figure 5.23: Shot #27695. The hard X-ray spectral evolution. The enhanced extreme hard X-ray emission during the plasma turning off.

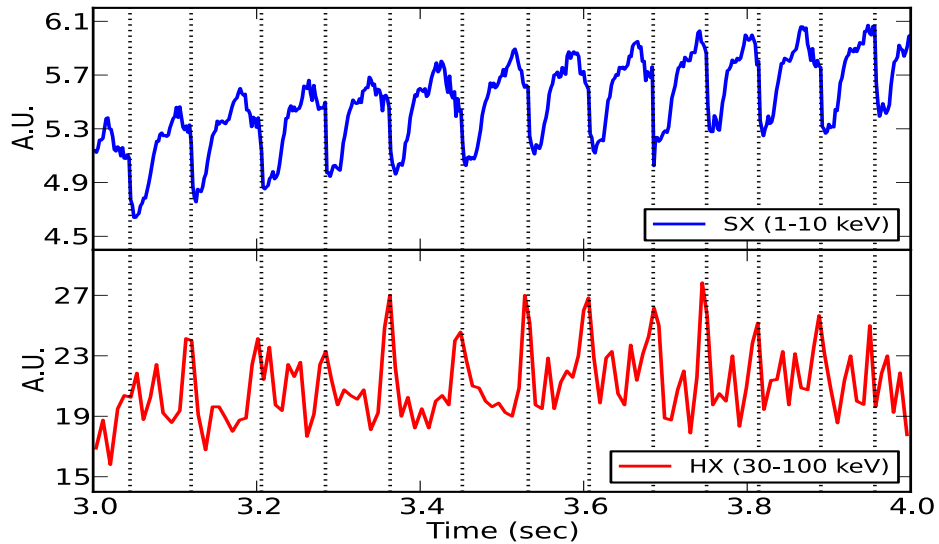


Figure 5.24: Shot #27761. The saw-tooth like feature observed in the hard X-ray range 30 -100 keV, compared with the soft X-ray signal from the camera J-047 which has the closest line-of-sight to our HX detector.

5. MEASUREMENTS OF SUPERTHERMAL ELECTRONS

“If physics was a religion, we’d have a much easier time raising money”

Leon M. Lederman

6

Summary and outlook

This thesis work has brought a spotlight on the high energy part of the X-ray spectrum providing a clear view of the associated electron distribution functions of superthermal electrons, especially generated during the strong ECRH and ECCD plasmas. It was foreseen that the hard X-ray detector at ASDEX Upgrade will fill up the observational gap between the research on the thermal processes (soft X-ray regime) and the nuclear processes (γ -ray regime). It was the major purpose of bringing the advanced detector technology from the astronomical space borne research to the field of energetic processes in tokamak research. The Silicon Drift Detector (SDD) in combination with the CsI(Tl) scintillator has been introduced and proven to be successful for its capabilities and suitability in the fusion research.

Numerous technical issues were faced with the detector setup, since the conditions in the torus hall are much different than those in the laboratory. Nevertheless a proper pulse height analysis based hard X-ray (PHX) diagnostic has been developed and eventually installed at ASDEX Upgrade.

The SDD has been characterized with and without the CsI(Tl) scintillator. The SDD alone, with its efficiency spanning over the soft X-ray range 1-20 keV, shows a capability of handling up to 300k photons/sec with ~ 140 eV resolution at 5.9 keV.

6. SUMMARY AND OUTLOOK

The SDD+CsI(Tl), with its increases efficiency over the hard X-ray range 10-500 keV, shows a capability of handling up to 45k photons/sec with ~ 6 keV resolution at 128 keV.

One of the problems tackled is the construction of the complex response function of the SDD+CsI(Tl) detector. The detailed laboratory tests of the simulated response function further added to our confidence on the detector characteristics. With the help of the detector response function, the forward modeling methodology is developed (through several numerical tools developed as Python modules). After establishing these tools, the proper measurement and analysis of the plasma was feasible.

For the first time the 10-500 keV hard X-ray spectroscopic measurements are carried out at ASDEX Upgrade. The profound evidence of the formation and evolution of the superthermal electrons is now clear in various ECRH plasma scenarios. The numerical electron distribution functions were obtained by Fokker-Planck simulations performed by O. Maj and E. Poli (Max Planck Institute for Plasma Physics, Garching). At a low ECRH power, it is found that the numerical electron distribution function obtained by the Fokker-Planck simulation is in close agreement with the measurements.

At ECRH powers greater than 1 MW (more than one gyrotron), the Fokker-Planck simulations were performed only with a simplistic approach, and the numerical electron distribution functions show only a qualitative match with the measurements. The Fokker-Planck simulations also predict that the superthermal tail is generated dominantly by the parallel electric field E_{\parallel} rather than the ECRH. However, the measurements show that the superthermal tail progressively extends with increasing ECRH power at constant density. This clear effect could not be reproduced well in the numerical simulations and needs further studies.

A bi-Maxwellian model is constructed and observed to be close to the real distribution of the superthermal electrons. The fraction of the superthermal population measured at different densities and ECRH powers, is seen to be roughly constant at 2%, but the total energy carried by them is seen to be increasing with the power available per electron $P/\langle n_{e,b} \rangle$.

In the selected plasma discharges at low as well as high ECRH powers, we measure in addition the signature of the runaway electrons through the extreme hard X-ray emission (100-500 keV). It is also noticed that the initial superthermal population can act as a seed population for the slide-away or runaway electrons. The

generation of the runaway electrons in the low power discharges is rather important due to its serious consequences, and still needs further investigations.

One of the interesting measurements concern the generation of superthermal electrons during magnetic re-connection events underlying the sawtooth crashes.

In future experiments, modification in the current setup is planned in order to improve the count rate limit and the timing accuracy, such that it achieves better sensitivity to the saw-tooth crashes, and similar fast processes.

The HX detector is currently incapable of distinguishing the photon events from the neutron events. This problem will be solved in the future by implementing a pulse shape discriminator (PSD) with the help of the new Data Acquisition System developed at Max Planck Institute for Plasma Physics, Garching. The detector response for the neutrons will be simulated using the Geant4 package, which can then enable to obtain the underlying neutron energy spectrum. In this way, eliminating the neutron signals from detected signals will improve the scope of the superthermal tail measurements in the plasma scenarios beyond those with just pure EC resonance heating. So far in this thesis, the novel hard X-ray diagnostic has been proven to be a key tool in probing the interesting physics related to ECRH and energetic electrons.

The necessary changes in the ray-tracing code TORBEAM are already ongoing, and it is then expected to avail a more realistic electron distribution function corresponding to the high power scenarios in the near future. There still exist some gaps between the theory and experiment, involving the role of the superthermal electrons and the efficiency of the current drive by the perpendicular heating of the electron cyclotron waves. Although a full clarification of these issues could not be achieved in the scope of this thesis, the experimental data are considered to provide important information for further benchmarks with theory.

6. SUMMARY AND OUTLOOK



Multi-channel Analyser (MCA)

The MCA board used for this purpose is manufactured by Fast compTec (model MCA-3 series P7882) [81]. The MCA board (see Figure A.1) was connected to the PC. The MCA was controlled by the software ‘MCDwin’, see Figure A.2. The MCA was operated with a total of 8192 channels (or channel gain). The MCA board offers a capacity of handling maximum pulse rate of 10^6 events per second (for sufficiently short shaping times). The MCDwin software provides primary tools such as, data visualization, fitting gaussian functions to the spectral lines, to apply the energy calibration, etc.

The analog signal from the shaper is fed to the MCA board through the ‘Analog in’ pin. The detector reset pulse (dead period) is gated with the help of gate-circuit. The gate signal is fed to the MCA through ‘gate-in’ pin. During every plasma discharge, the MCA is turned on and off automatically by an external trigger signal provided by ASDEX Upgrade standard diagnostics trigger, which is fed to the board through ‘TRG-in’ pin. The MCA and the PC is remotely controlled via the VNCviewer software.

A. MULTI-CHANNEL ANALYSER (MCA)

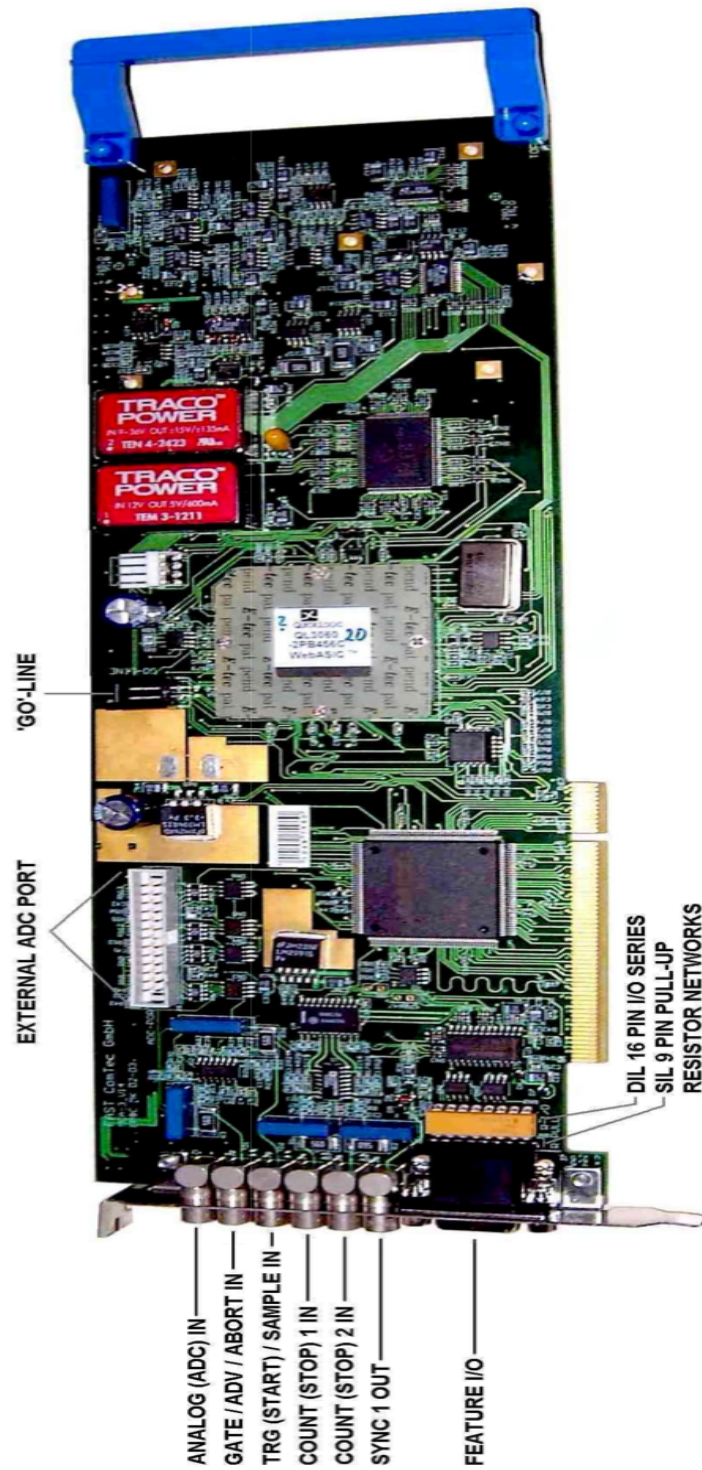


Figure A.1: The multi-channel analyzer PCI card installed in a PC. [81]

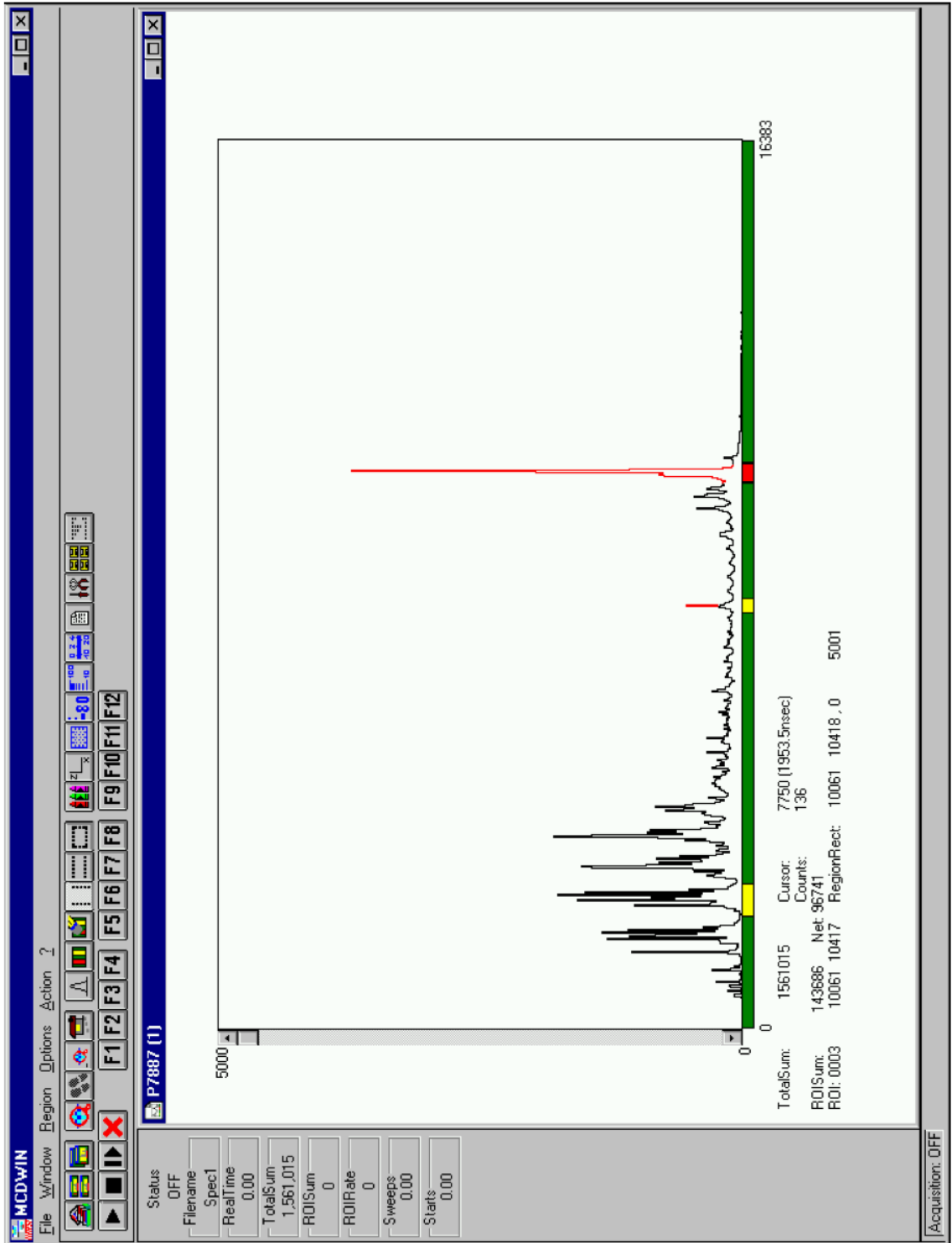


Figure A.2: The windows based software MCDwin to operate the MCA board.[81]

A. MULTI-CHANNEL ANALYSER (MCA)

B

Graphical User Interface: Elist

A Python based graphical user interface (GUI), called as EList, is designed in this thesis work, mainly to control the module EventList in a user friendly way. The GUI - EList allows quick analysis and handling of the hard X-ray data. The GUI - EList opens a main control panel and a separate ‘input/output error’ window, see an example in Figure B.1. It opens a data visualization window separately for each plasma discharge, and allows handling of multiple spectra at the same time.

The control panel (shown on the left) allows the user to read a particular discharge data and perform tasks such as rebin the data in time and energy both, correct for time offset, set time/energy range, and plot a (time-energy) 2-dimensional histogram.

The right side colored plot is a typical visualization of the spectral data in 2-dimensions, energy on x-axis and time on y-axis. It is an interactive plot. Drawing a rectangle on it with the left-click on the mouse, updates the corresponding time and energy sliced 2D plot. The two subplots at the left and bottom of the 2D plot, are projected time-trace and energy spectrum respectively.

B. GRAPHICAL USER INTERFACE: ELIST

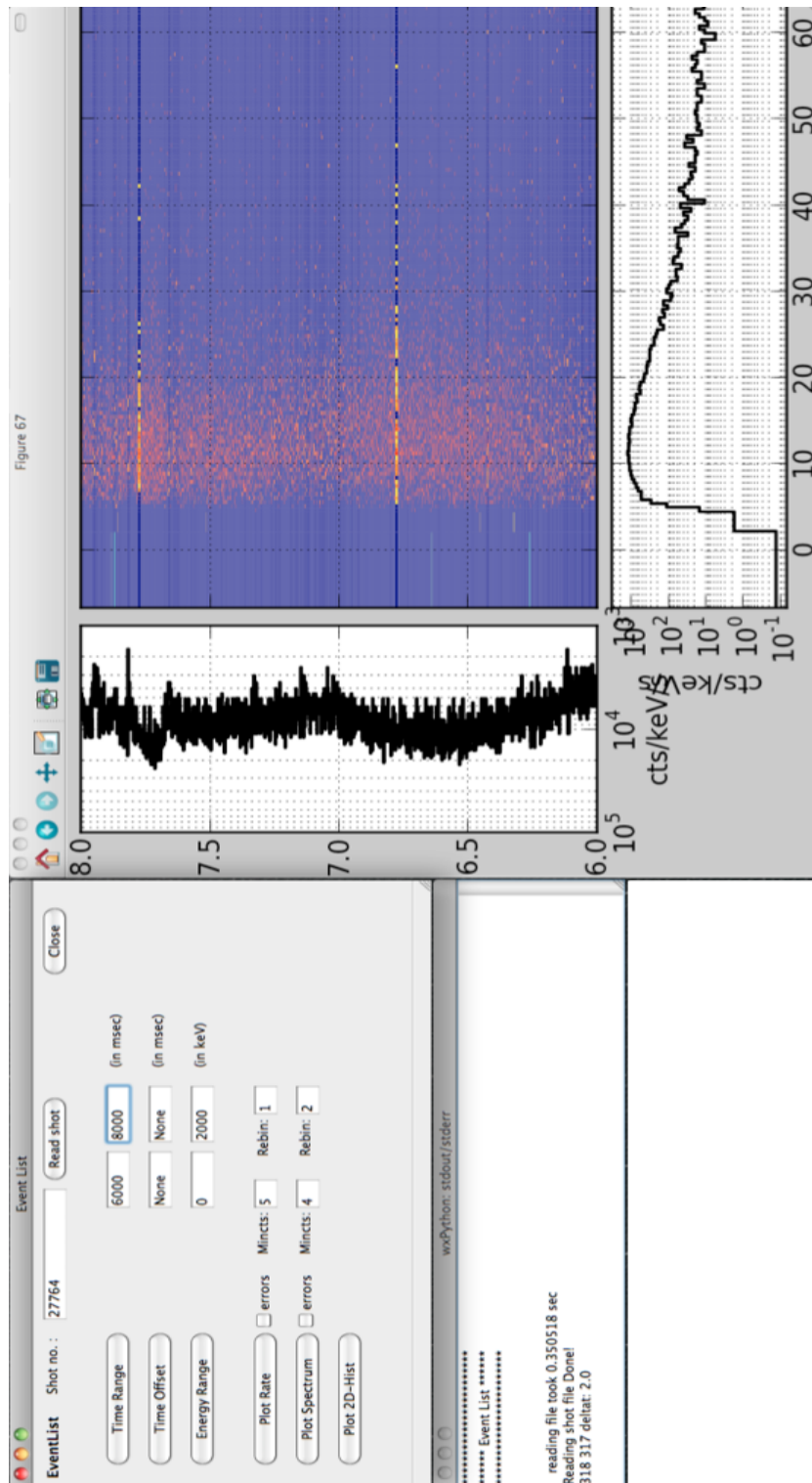


Figure B.1: The Graphical User Interface developed for the hard X-ray data handling, manipulation and visualization.

C

Spectral analysis of selected shots

The following figures illustrate the spectral analysis of many of the piggy-back discharges, spanning over range of densities and powers, as listed in Table 5.1. The bi-Maxwellian model is fitted to the measured spectra using the least square algorithm in Python, providing the tail temperature and the fractional density of the superthermal electrons, and are plotted in Figure 5.16 and 5.17 respectively in the Section 5.5.5. The Table C.1 lists the model fit parameters.

The two-temperature bi-Maxwellian model is fitted to the measured data. In the discharges #27761 (Figure C.1) and #27698 (Figure C.2) the superthermal tail is fitted well with the tail temperature. However, in the discharges #27694 (Figure C.3), #27695 (Figure C.4) and #27683 (Figure C.5) the superthermal tails gradually change their slope as a function of energy, and the simple two-temperature model starts deviating from the measured tail.

C. SPECTRAL ANALYSIS OF SELECTED SHOTS

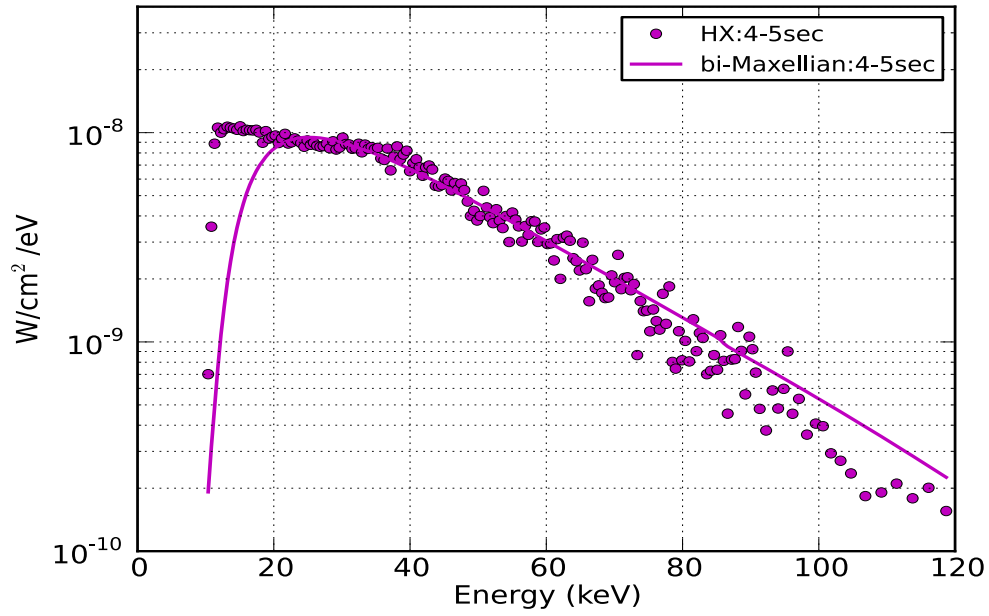


Figure C.1: Shot #27761.

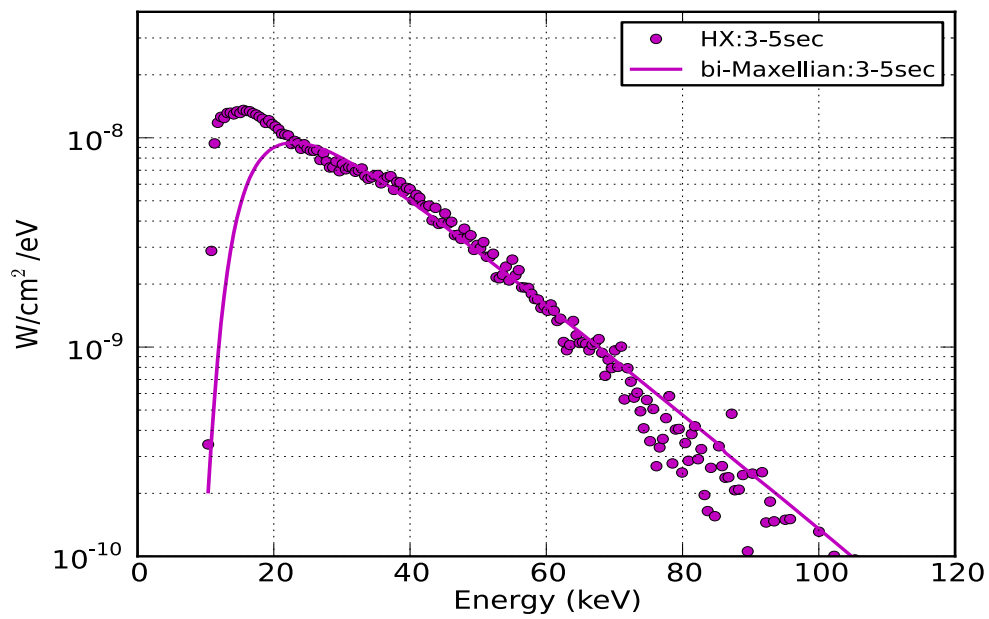


Figure C.2: Shot #27698.

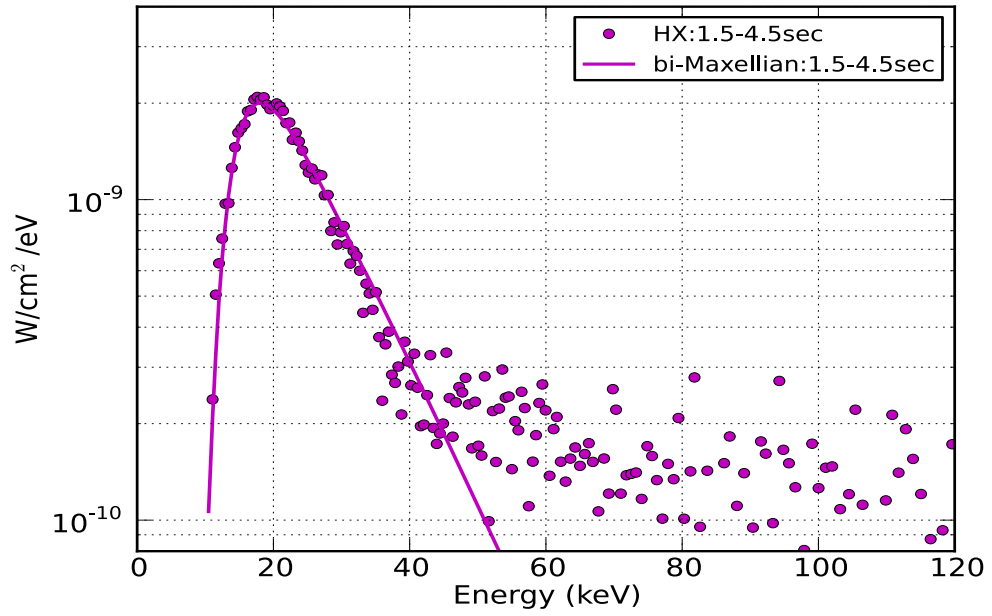


Figure C.3: Shot #27694.

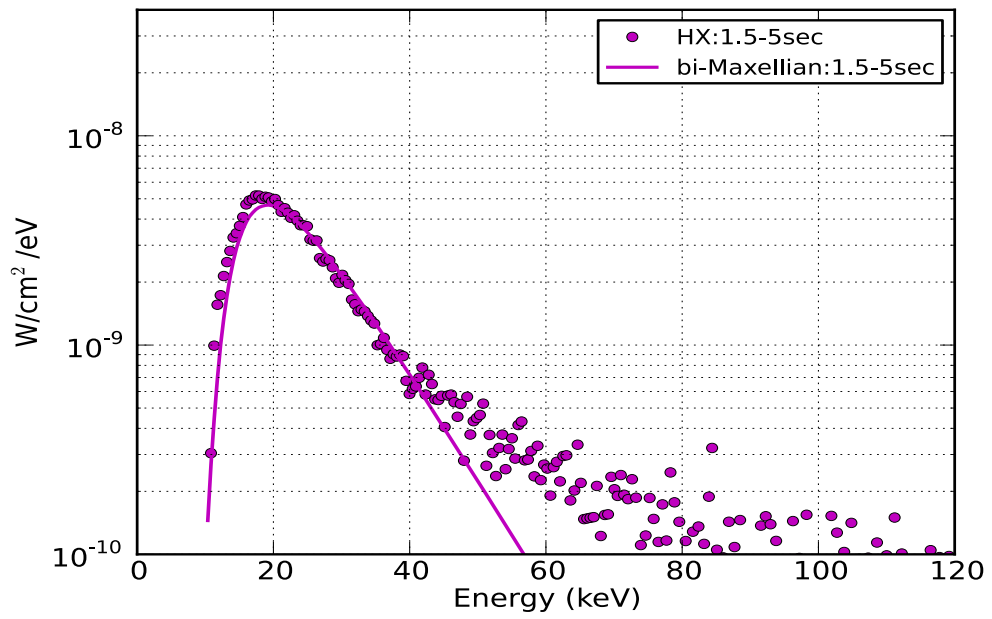


Figure C.4: Shot #27695.

C. SPECTRAL ANALYSIS OF SELECTED SHOTS

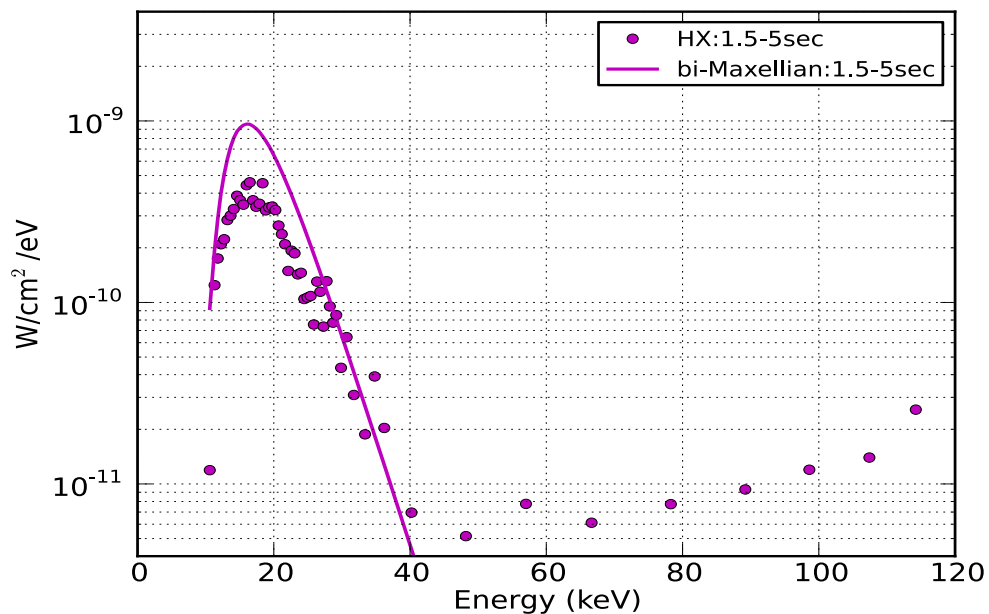


Figure C.5: Shot #27683.

Table C.1: The bi-Maxwellian model analysis of the selected piggy-back experiments, the corresponding model fit parameters are listed below.

$P/(\langle n_e \rangle / [\times 10^{13}])$ ($MW \cdot cm^{-3}$)	shot no.	Bulk electron Temp. (keV)	Bi-Max. tail Temp. (keV)	Fractional density (%)
2.113	27761	10.5	24 ± 0.5	1.92 ± 0.02
1.278	27698	7.3	16.5 ± 0.2	2.16 ± 0.02
0.438	27694	3	9.4 ± 0.3	1.16 ± 0.05
0.379	27695	3.1	8.2 ± 0.2	2.31 ± 0.05
0.162	27683	2.7	$2.2 \pm -$	0.037 ± 0.0001

References

- [1] H. A. BETHE. **Energy Production in Stars.** *Phys. Rev.*, **55**:103–103, Jan 1939. 1, 4
- [2] L. SPITZER, JR. **The Stellarator Concept.** *Physics of Fluids*, **1**:253–264, July 1958. 1
- [3] N. TANAKA. **World Energy Outlook - 2009.** Technical report, International Energy Agency, 2009. 2
- [4] R.J. HAWRYLUK, D.J. CAMPBELL, G. JANESCHITZ, ET AL. **Principal physics developments evaluated in the ITER design review.** *Nuclear Fusion*, **49**(6):065012, 2009. 3, 4
- [5] JOHN WESSON. *Tokamaks; 4th ed.* International series of monographs on physics. Oxford Univ. Press, Oxford, 2011. 4, 5, 11, 129, 161
- [6] H.-S. BOSCH AND G.M. HALE. **Improved formulas for fusion cross-sections and thermal reactivities.** *Nuclear Fusion*, **32**(4):611, 1992. 5, 6
- [7] A. K. SURI, N. KRISHNAMURTHY, AND I. S. BATRA. **Materials issues in fusion reactors.** *Journal of Physics Conference Series*, **208**(1):012001, February 2010. 5
- [8] R.F. POST. **The magnetic mirror approach to fusion.** *Nuclear Fusion*, **27**(10):1579, 1987. 6
- [9] J F LYON. **Review of recent stellarator results in the USA, the USSR and Japan.** *Plasma Physics and Controlled Fusion*, **32**(11):1041, 1990. 6

REFERENCES

- [10] M. WANNER AND W7-X TEAM. **Design goals and status of the WENDELSTEIN 7-X project.** *Plasma Physics and Controlled Fusion*, **42**:1179–1186, November 2000. 6
- [11] M. WANNER, V. ERCKMANN, J.-H. FEIST, ET AL. **Status of WENDELSTEIN 7-X construction.** *Nuclear Fusion*, **43**(6):416, 2003. 6
- [12] V.P. SMIRNOV. **Tokamak foundation in USSR/Russia 1950–1990.** *Nuclear Fusion*, **50**(1):014003, 2010. 6
- [13] A. HERRMANN AND O. GRUBER. **ASDEX Upgrade - Introduction and Overview.** *Fusion Science and Technology*, **44**(3):569, November 2003. 8, 74
- [14] MITSURU KIKUCHI. **A Review of Fusion and Tokamak Research Towards Steady-State Operation: A JAEA Contribution.** *Energies*, **3**(11):1741–1789, 2010. 8
- [15] B. STREIBL, P. T. LANG, F. LEUTERER, J. NOTERDAEME, AND ET AL. **Machine Design, Fueling, and Heating in ASDEX Upgrade.** *Fusion Science and Technology*, **44**(3):578, November 2003. 9, 11, 74, 75, 169
- [16] F.F. CHEN. *Introduction to Plasma Physics and Controlled Fusion*. Number v. 1 in Introduction to Plasma Physics and Controlled Fusion. 1984. 11
- [17] T. H. STIX. *The Theory of Plasma Waves*, New York: McGraw-Hill, 1962. 1962. 12
- [18] R. A. CAIRNS AND C. N. LASHMORE-DAVIES. **A unified theory of a class of mode conversion problems.** *Physics of Fluids*, **26**:1268–1274, May 1983. 12
- [19] E. WESTERHOF. **Wave propagation through an electron cyclotron resonance layer.** *Plasma Phys. Contr. Fusion*, **39**:1015–1029, June 1997. 12
- [20] V. ERCKMANN AND U. GASPARINO. **Electron cyclotron resonance heating and current drive in toroidal fusion plasmas.** *Plasma Phys. Contr. Fusion*, **36**:1869–1962, 1994. 12, 14
- [21] E. WESTERHOF. **Electron cyclotron waves.** *Transactions of Fusion Science and Technology*, **49**:195, February 2006. 12, 109

-
- [22] N. J. FISCH. **Theory of current drive in plasmas.** *Reviews of Modern Physics*, **59**:175–234, January 1987. 13
- [23] O. SAUTER, M. A. HENDERSON, F. HOFMANN, ET AL. **Steady-State Fully Non-inductive Current Driven by Electron Cyclotron Waves in a Magnetically Confined Plasma.** *Physical Review Letters*, **84**:3322–3325, April 2000. 14
- [24] X. LITAUDON, F. CRISANTI, B. ALPER, ET AL. **Towards fully non-inductive current drive operation in JET.** *Plasma Physics and Controlled Fusion*, **44**(7):1057, 2002. 14
- [25] M. MURAKAMI, M. R. WADE, C. M. GREENFIELD, ET AL. **Modification of the Current Profile in High-Performance Plasmas using Off-Axis Electron-Cyclotron-Current Drive in DIII-D.** *Physical Review Letters*, **90**(25):255001, June 2003. 14
- [26] G. GANTENBEIN, H. ZOHRM, G. GIRUZZI, ET AL. **Complete Suppression of Neoclassical Tearing Modes with Current Drive at the Electron-Cyclotron-Resonance Frequency in ASDEX Upgrade Tokamak.** *Physical Review Letters*, **85**:1242–1245, August 2000. 14
- [27] J. I. PALEY, F. FELICI, S. CODA, ET AL. **Real time control of the sawtooth period using EC launchers.** *Plasma Physics and Controlled Fusion*, **51**(5):055010, 2009. 14
- [28] H. ZOHRM. **Stabilization of neoclassical tearing modes by electron cyclotron current drive.** *Physics of Plasmas*, **4**:3433–3435, September 1997. 14
- [29] H. ZOHRM, G. GANTENBEIN, G. GIRUZZI, ET AL. **Experiments on neoclassical tearing mode stabilization by ECCD in ASDEX Upgrade.** *Nuclear Fusion*, **39**(5):577, 1999. 14
- [30] N. BERTELLI, D. DE LAZZARI, AND E. WESTERHOF. **Requirements on localized current drive for the suppression of neoclassical tearing modes.** *Nuclear Fusion*, **51**(10):103007, October 2011. 14

REFERENCES

- [31] Y. R. LIN-LIU. **Localized Electron Cyclotron Current Drive in DIII-D: Experiment and Theory.** In *APS Meeting Abstracts*, page I1003, October 2000. 14
- [32] N. J. FISCH AND A. H. BOOZER. **Creating an Asymmetric Plasma Resistivity with Waves.** *Phys. Rev. Lett.*, **45**:720–722, Sep 1980. 14, 123
- [33] E. LAZZARO, G. RAMPONI, AND A. FIGUEIREDO. **Calculation of electron cyclotron current drive consistent with tokamak transport.** *Nuclear Fusion*, **36**:689–706, June 1996. 14
- [34] J. DECKER. **ECCD for Advanced Tokamak Operations Fisch-Boozer versus Ohkawa Methods.** In C. B. FOREST, editor, *Radio Frequency Power in Plasmas*, **694** of *American Institute of Physics Conference Series*, pages 447–454, December 2003. 14
- [35] B. BAZYLEV, G. ARNOUX, W. FUNDAMENSKI, AND JET EFDA CONTRIBUTORS. **Modeling of runaway electron beams for JET and ITER.** *Journal of Nuclear Materials*, **415**:841, August 2011. 15
- [36] A. H. BOOZER. **Theory of tokamak disruptions.** *Physics of Plasmas*, **19**(5):058101, May 2012. 15
- [37] E. WESTERHOF, A. G. PEETERS, AND W. L. SCHIPPERS. **RELAX, a computer code for the study of collisional and wave driven relaxation of the electron distribution function in toroidal geometry.** Technical Report Rijnhuizen Report No. RR 92-211 CA, FOM-Institute for Plasma Physics, 1992. 15, 16
- [38] E. POLI, A. G. PEETERS, AND G. V. PEREVERZEV. **TORBEAM, a beam tracing code for electron-cyclotron waves in tokamak plasmas.** *Computer Physics Communications*, **136**:90–104, May 2001. 15, 16, 22
- [39] N. MARUSHCHENKO, U. GASPARINO, H. MAASSBERG, AND M. ROMÉ. **Bounce-averaged Fokker-Planck code for the description of ECRH in a periodic magnetic field.** *Computer Physics Communications*, **103**:145–156, July 1997. 15

-
- [40] H. NUGA AND A. FUKUYAMA. **Kinetic Integrated Modeling of Plasma Heating in Tokamaks.** *progress in Nuclear Science and Technology*, **2**:78, 2011. 15
- [41] O. MAJ, E. POLI, AND E. WESTERHOF. **Coupling the beam tracing code TORBEAM and the Fokker-Planck solver RELAX for fast electrons.** *Journal of Physics Conference Series*, **401**(1):012013, December 2012. 16, 17
- [42] G. B. RYBICKI AND A. P. LIGHTMAN. *Radiative processes in astrophysics.* 1979. 17, 18, 19, 25, 82
- [43] S. CODA, T. P. GOODMAN, M. A. HENDERSON, ET AL. **High-power ECH and fully non-inductive operation with ECCD in the TCV tokamak.** *Plasma Physics and Controlled Fusion*, **42**:B311–B321, December 2000. 20
- [44] A. POLEVOI, A. ZVONKOV, T. OIKAWA, ET AL. **Assessment of current drive efficiency and the synergetic effect for ECCD and LHCD and the possibility of long pulse operation in ITER.** *Nuclear Fusion*, **48**(1):015002, January 2008. 20
- [45] H. ZOHRM, G. GANTENBEIN, F. LEUTERER, ET AL. **Control of NTMs by ECCD on ASDEX Upgrade in view of ITER application.** *Plasma Physics and Controlled Fusion*, **49**:341, December 2007. 20
- [46] M BESSENRODT-WEBERPALS, H J DE BLANK, M MARASCHEK, ET AL. **MHD activity as seen in soft x-ray radiation.** *Plasma Physics and Controlled Fusion*, **38**(9):1543, 1996. 21
- [47] V. IGOCHINE, A. GUDE, M. MARASCHEK, AND ASDEX UPGRADE TEAM. **Hotlink based Soft X-ray Diagnostic on ASDEX Upgrade.** IPP Reports 1/338, May 2010. 21
- [48] A. WELLER, B. HUBER, J. BELAPURE, ET AL. **X-Ray Pulse Height Analysis on ASDEX Upgrade.** In *Proceedings of the 38th EPS Conference on Plasma Physics, Strasbourg, France*, pages P5.054, Vol. 35G, 27 June – 1 July 2011. 21
- [49] G. TARDINI, A. ZIMBAL, B. ESPOSITO, ET AL. **First neutron spectrometry measurements in the ASDEX Upgrade tokamak.** *Journal of Instrumentation*, **7**:C3004, March 2012. 21

REFERENCES

- [50] L. GIACOMELLI, A. ZIMBAL, K. TITTELMEIER, ET AL. **The compact neutron spectrometer at ASDEX Upgrade.** *Review of Scientific Instruments*, **82**(12):123504, December 2011. 21
- [51] A. WELLER, S. MOHR, AND C. JUNGHANS. **Concepts of x-ray diagnostics for WENDELSTEIN 7-X.** *Review of Scientific Instruments*, **75**:3962–3965, October 2004. 21, 82
- [52] B.A. CARRERAS, G. GRIEGER, J.H. HARRIS, ET AL. **Progress in stellarator/heliotron research: 1981–1986.** *Nuclear Fusion*, **28**(9):1613, 1988. 21
- [53] G.F. KNOLL. "Radiation Detection and Measurement". John Wiley & Sons, 3 edition, 1999. 22, 25, 40, 42, 44, 169
- [54] IAN H HUTCHINSON. *Principles of plasma diagnostics; 2nd ed.* Cambridge Univ. Press, Cambridge, 2002. 22
- [55] F. MEDINA, L. RODRÍGUEZ-RODRIGO, M. A. OCHANDO, AND F. CASTEJÓN. **Superthermal electrons in the TJ-IU torsatron.** *Plasma Physics and Controlled Fusion*, **40**:1897–1905, November 1998. 22
- [56] Z. Y. CHEN, B. N. WAN, S. Y. LIN, ET AL. **Measurement of the non-thermal bremsstrahlung emission between 20 and 7000 keV in the HT-7 Tokamak.** *Nuclear Instruments and Methods in Physics Research A*, **560**:558–563, May 2006. 22
- [57] S. MUTO, S. MORITA, S. KUBO, ET AL. **First measurement of hard x-ray spectrum emitted from high-energy electrons in electron cyclotron heated plasma of LHD.** *Review of Scientific Instruments*, **74**(3):1993–1996, 2003. 22
- [58] S. SAJJAD, X. GAO, B. LING, S. H. BHATTI, AND T. ANG. **Effect of gas puffing on current ramp-down ohmic discharges in HT-7 tokamak.** *Physics Letters A*, **373**:1133–1139, March 2009. 22
- [59] R.J. ZHOU, L.Q. HU, S.Y. LIN, ET AL. **Experimental observation of interaction of runaway electrons with lower hybrid waves in slide-away regime in the HT-7 tokamak.** *Physics Letters A*, **376**(16):1360 – 1365, 2012. 22

-
- [60] M. MARISALDI, C. FIORINI, C. LABANTI, ET AL. **Silicon drift detectors coupled to CsI(Tl) scintillators for spaceborne gamma-ray detectors.** *Nuclear Physics B Proceedings Supplements*, **150**:190–193, January 2006. 24, 42
- [61] M. J. FREYBERG, U. G. BRIEL, K. DENNERL, ET AL. **EPIC pn-CCD detector aboard XMM-Newton: status of the background calibration.** In K. A. FLANAGAN AND O. H. W. SIEGMUND, editors, *Society of Photo-Optical Instrumentation Engineers (SPIE) Conference Series*, **5165** of *Society of Photo-Optical Instrumentation Engineers (SPIE) Conference Series*, pages 112–122, February 2004. 24
- [62] N. MEIDINGER, R. ANDRITSCHKE, S. EBERMAYER, ET AL. **CCD detectors for spectroscopy and imaging of x-rays with the eROSITA space telescope.** In *Society of Photo-Optical Instrumentation Engineers (SPIE) Conference Series*, **7435** of *Society of Photo-Optical Instrumentation Engineers (SPIE) Conference Series*, August 2009. 24
- [63] R. STAUBERT, E. KENDZIORRA, D. BARRET, ET AL. **Proposal to do fast x-ray timing with XEUS.** In J. E. TRUEMPER AND H. D. TANANBAUM, editors, *Society of Photo-Optical Instrumentation Engineers (SPIE) Conference Series*, **4851** of *Society of Photo-Optical Instrumentation Engineers (SPIE) Conference Series*, pages 414–420, March 2003. 24
- [64] G. R. GILMORE. *Practical Gamma-ray Spectrometry, 2nd Edition.* Wiley-VCH Verlag, 2008. 25, 42, 44, 65, 169
- [65] F. BIGGS AND R. LIGHTHILL. **Photo-electric absorption cross-section.** ?, 1990. 25
- [66] M.J. BERGER, J.H. HUBBELL, S.M. SELTZER, ET AL. **XCOM: Photon Cross Sections Database.** NIST Standard Reference Database 8 (XGAM) NBSIR 87-3597, National Institute of Standards and Technology (NIST), PML, Radiation and Biomolecular Physics Division, March 1998. 27, 58, 161
- [67] DAVID J. GRIFFITHS. *Introduction to Electrodynamics (3rd Edition).* Benjamin Cummings, 1998. 27

REFERENCES

- [68] F. J. RAMÍREZ-JIMÉNEZ. **X-Ray Spectroscopy with PIN diodes**. In A. BASHIR, V. VILLANUEVA, AND L. VILLASEQOR, editors, *Particles and Fields: X Mexican Workshop*, **857** of *American Institute of Physics Conference Series*, pages 121–133, September 2006. 28
- [69] E. GATTI AND P. REHAK. **Semiconductor drift chamber - An application of a novel charge transport scheme**. *Nuclear Instruments and Methods in Physics Research*, **225**:608–614, September 1984. 28
- [70] P. REHAK, E. GATTI, A. LONGONI, ET AL. **Semiconductor drift chambers for position and energy measurements**. *Nuclear Instruments and Methods in Physics Research A*, **235**:224–234, April 1985. 28
- [71] G. A. CARINI, W. CHEN, G. DE GERONIMO, ET AL. **Performance of a Thin-Window Silicon Drift Detector X-Ray Fluorescence Spectrometer**. *IEEE Transactions on Nuclear Science*, **56**:2843–2849, October 2009. 28
- [72] E. GATTI AND P. REHAK. **Review of semiconductor drift detectors**. *Nuclear Instruments and Methods in Physics Research A*, **541**:47–60, April 2005. 28
- [73] P. LECHNER, S. ECKBAUER, R. HARTMANN, ET AL. **Silicon drift detectors for high resolution room temperature X-ray spectroscopy**. *Nuclear Instruments and Methods in Physics Research A*, **377**:346–351, February 1996. 28
- [74] C. FIORINI, J. KEMMER, P. LECHNER, ET AL. **A new detection system for x-ray microanalysis based on a silicon drift detector with Peltier cooling**. *Review of Scientific Instruments*, **68**:2461–2465, June 1997. 28
- [75] L. STRÜDER, U. BRIEL, K. DENNERL, ET AL. **The European Photon Imaging Camera on XMM-Newton: The pn-CCD camera**. *Astronomy and Astrophysics*, **365**:L18–L26, January 2001. 28
- [76] L. STRÜDER, S. BONERZ, H. BRÄUNINGER, G. HASINGER, AND ET. AL. **Imaging Spectrometers for Future X-ray Missions**. In H. INOUE AND H. KUNIEDA, editors, *New Century of X-ray Astronomy*, **251** of *Astronomical Society of the Pacific Conference Series*, page 200, 2001. 28

-
- [77] R. ALBERTI, C. FIORINI, A. LONGONI, AND H. SOLTAU. **High-rate X-ray spectroscopy using a Silicon Drift Detector and a charge preamplifier.** *Nuclear Instruments and Methods in Physics Research A*, **568**:106–111, November 2006. 28
- [78] R. ALBERTI, C. FIORINI, C. GUAZZONI, T. KLATKA, AND A. LONGONI. **Elemental mapping by means of an ultra-fast XRF spectrometer based on a novel high-performance monolithic array of Silicon Drift Detectors.** *Nuclear Instruments and Methods in Physics Research A*, **580**:1004–1007, October 2007. 28
- [79] R. ALBERTI, N. GRASSI, C. GUAZZONI, AND T. KLATKA. **Optimized readout configuration for PIXE spectrometers based on Silicon Drift Detectors: Architecture and performance.** *Nuclear Instruments and Methods in Physics Research A*, **607**:458–462, August 2009. 28
- [80] R. REDUS. *Digital Pulse Processors, Theory of Operation.* Amptek Inc., Nov 2009. 33, 161
- [81] FAST ComTec GmbH, Gruenwalder Weg 28a, D-82041 Oberhaching Germany. *Multichannel Analyzer / Dual Input Multiscaler User Manual*, v3.3 edition, July 2012. 35, 137, 138, 139, 167
- [82] U. FANO. **Ionization Yield of Radiations. II. The Fluctuations of the Number of Ions.** *Physical Review*, **72**:26–29, July 1947. 38
- [83] C. A. KLEIN. **Bandgap Dependence and Related Features of Radiation Ionization Energies in Semiconductors.** *Journal of Applied Physics*, **39**:2029–2038, March 1968. 38
- [84] P. LECHNER, R. HARTMANN, H. SOLTAU, AND L. STRÜDER. **Pair creation energy and Fano factor of silicon in the energy range of soft X-rays.** *Nuclear Instruments and Methods in Physics Research A*, **377**:206–208, February 1996. 38
- [85] D. M. SCHLOSSER, P. LECHNER, G. LUTZ, ET AL. **Expanding the detection efficiency of silicon drift detectors.** *Nuclear Instruments and Methods in Physics Research A*, **624**:270–276, December 2010. 42, 43, 89, 162

REFERENCES

- [86] M. BINDA, D. NATALI, M. SAMPIETRO, T. AGOSTINELLI, AND L. BEVERINA. **Organic based photodetectors: Suitability for X- and γ -rays sensing application.** *Nuclear Instruments and Methods in Physics Research Section A: Accelerators, Spectrometers, Detectors and Associated Equipment*, **624(2)**:443 – 448, 2010. 42
- [87] V. BELLINI. **Radiation Measurement: X and γ ray detection.** In *ICARO-2011, ITA*. Physics and Astronomy Department, University of Catania, Catania, Italy, 2011. 42
- [88] SAINT-GOBAIN CRYSTALS. **Photodiode scintillation detectors.** Technical report, Saint-Gobain Crystals, 2008. 43, 45, 162
- [89] J. D. VALENTINE, W. W. MOSES, S. E. DERENZO, D. K. WEHE, AND G. F. KNOLL. **Temperature dependence of CsI(Tl) gamma-ray excited scintillation characteristics.** *Nuclear Instruments and Methods in Physics Research A*, **325**:147–157, February 1993. 43
- [90] **Science Jokes web**, <http://www.jcdverha.home.xs4all.nl/scijokes>. 47
- [91] R.S. GRANETZ AND P. SMEULDERS. **X-ray tomography on JET.** *Nuclear Fusion*, **28(3)**:457, 1988. 53
- [92] MICHAEL C. KAUFMAN. *Lower hybrid experiments using an interdigital line antenna on the reversed field pinch.* PhD thesis, University of Wisconsin-Madison, 2009. 53
- [93] LEBOW INC. 5960 MANDARIN AVE. GOLETA CA 93117 USA. **Ultrathin foils.** 55
- [94] A. Z. KISS, E. KOLTAY, B. NYAKO, AND ET. AL. **Measurements of Relative Thick Target Yields For PIGE Analysis On Light Elements In The Proton Energy Interval 2.4-4.2 MeV.** *J. of Radioanalytical and Nuclear Chemistry*, **89(1)**:123, 1985. 71, 94, 169
- [95] J. RÄISÄNEN. **Heavy element ($Z > 30$) thick-target gamma-ray yields induced by 1.7 and 2.4 MeV protons.** *Nuclear Instruments and Methods in Physics Research*, **205**:259–268, January 1983. 71, 94, 169

- [96] K. A. ARNAUD. **XSPEC: The First Ten Years**. In G. H. JACOBY AND J. BARNES, editors, *Astronomical Data Analysis Software and Systems V*, **101** of *Astronomical Society of the Pacific Conference Series*, page 17, 1996. 78
- [97] S. AGOSTINELLI, J. ALLISON, K. AMAKO, AND J. APOSTOLAKIS ET. AL. **Geant4 - a simulation toolkit**. *Nuclear Instruments and Methods in Physics Research Section A: Accelerators, Spectrometers, Detectors and Associated Equipment*, **506(3)**:250 – 303, 2003. 88
- [98] J. ALLISON, K. AMAKO, J. APOSTOLAKIS, ET AL. **Geant4 developments and applications**. *Nuclear Science, IEEE Transactions on*, **53(1)**:270 –278, feb. 2006. 88
- [99] UDO VON TOUSSAINT. **Bayesian inference in physics**. *Rev. Mod. Phys.*, **83**:943–999, Sep 2011. 91
- [100] F.J. SAGLIME, Y. DANON, R.C. BLOCK, ET AL. **A system for differential neutron scattering experiments in the energy range from 0.5 to 20MeV**. *Nuclear Instruments and Methods in Physics Research Section A: Accelerators, Spectrometers, Detectors and Associated Equipment*, **620(2)**:401 – 409, 2010. 103, 105, 165
- [101] A. W. SUNYAR, J. W. MIHELICH, AND M. GOLDHABER. **Decay of Cs^{134m} (3.1 hr)**. *Physical Review*, **95**:570–572, July 1954. 107
- [102] R. L. HEATH. **Gamma-ray Spectrum Catalogue, Ge (Li) Spectrometry**. Technical Report USAEC Report ANC-1000, Idaho National Laboratory, 1974. 107
- [103] G. L. KEISTER, E. B. LEE, AND F. H. SCHMIDT. **Radioactive Decay of Cs¹³⁴ and Cs^{134m}**. *Phys. Rev.*, **97**:451–456, Jan 1955. 107
- [104] R. HARVEY, , M. MCCOY, AND KERBEL G. **Power Dependence of Electron-Cyclotron Current Drive for Low- and High-Field Absorption in Tokamaks**. *Physical Review Letters*, **62(3)**:426, 1989. 109
- [105] K. V. CHEREPANOV AND A. B. KUKUSHKIN. **Self-consistent simulation of electron cyclotron radiation transport and suprathermal electron kinetics in tokamak plasmas**. In *APS Meeting Abstracts*, page 2001, November 2004. 110

REFERENCES

- [106] K. V. CHEREPANOV, A. B. KUKUSHKIN, L. K. KUZNETSOVA, AND WESTERHOF E. **EC Radiation Transport in Fusion Reactor-Grade Tokamaks: Parameterization of Power Loss Density Profile, Non-Thermal Profile Effects under ECCD/ECRH conditions.** In *Proceedings of the 21st IAEA Fusion Energy Conference (FEC 2006)*, IAEA-CN-149, Chengdu, China, 2006. 110
- [107] L. K. KUZNETSOVA, K. V. CHEREPANOV, A. B. KUKUSHKIN, AND WESTERHOF E. **Formation of Superthermal Electrons Under Conditions of ECRH and ECCD in ITER-like Tokamak.** In *Proceedings of the 14th Joint Workshop on Electron Cyclotron Emission and Electron Cyclotron Resonance Heating (EC-14)*, Santorini, Greece, 2006. 110
- [108] T. C. LUCE. **Realizing steady-state tokamak operation for fusion energy.** *Physics of Plasmas*, **18**(3):030501, March 2011. 110
- [109] R. PRATER. **Heating and current drive by electron cyclotron waves.** *Physics of Plasmas*, **11**:2349–2376, May 2004. 110
- [110] R.O. DENDY, M.R. O'BRIEN, M. COX, AND D.F.H. START. **Comparison of theory with electron cyclotron current drive experiments on WT-2.** *Nuclear Fusion*, **27**(3):377, 1987. 110
- [111] S. CODA, S. ALBERTI, P. BLANCHARD, ET AL. **Electron cyclotron current drive and suprathermal electron dynamics in the TCV tokamak.** *Nuclear Fusion*, **43**(11):1361, 2003. 110
- [112] P. BLANCHARD, S. ALBERTI, S. CODA, ET AL. **High field side measurements of non-thermal electron cyclotron emission on TCV plasmas with ECH and ECCD.** *Plasma Physics and Controlled Fusion*, **44**(10):2231, 2002. 110
- [113] A. LAZAROS. **Development of a superthermal electron avalanche and tearing mode suppression during electron cyclotron resonant heating.** *Physics of Plasmas*, **8**(4):1263–1266, 2001. 110
- [114] A. LAZAROS. **New experimental evidence for the stabilizing effect of a superthermal electron avalanche during electron cyclotron resonant heating.** *Physics of Plasmas*, **9**(7):3007–3012, 2002. 110, 126

-
- [115] W. CHEN, X.T. DING, YI. LIU, ET AL. **Destabilization of the internal kink mode by energetic electrons on the HL-2A tokamak.** *Nuclear Fusion*, **49**(7):075022, July 2009. 110
- [116] K. WONG, M. CHU, T. LUCE, ET AL. **Internal Kink Instability during Off-Axis Electron Cyclotron Current Drive in the DIII-D Tokamak.** *Physical Review Letters*, **85**(5):996–999, July 2000. 110
- [117] E. M. HOLLMANN, P. B. PARKS, D. A. HUMPHREYS, ET AL. **Effect of applied toroidal electric field on the growth/decay of plateau-phase runaway electron currents in DIII-D.** *Nuclear Fusion*, **51**(10):103026, October 2011. 126, 128
- [118] Z. Y. CHEN, W. C. KIM, A. C. ENGLAND, ET AL. **Investigation of the effect of electron cyclotron heating on runaway generation in the KSTAR tokamak.** *Physics Letters A*, **375**:2569–2572, June 2011. 126, 128
- [119] J. F. DRAKE, M. A. SHAY, W. THONGTHAI, AND M. SWISDAK. **Production of Energetic Electrons during Magnetic Reconnection.** *Phys. Rev. Lett.*, **94**:095001, Mar 2005. 129
- [120] E. G. ZWEIBEL AND M. YAMADA. **Magnetic Reconnection in Astrophysical and Laboratory Plasmas.** *Ann. Rev. of A & A*, **47**:291–332, September 2009. 129
- [121] I. KLIMANOV, A. FASOLI, AND T. P. GOODMAN. **Generation of suprathermal electrons during sawtooth crashes in a tokamak plasma.** *Plasma Physics and Controlled Fusion*, **49**(3):L1–L6, 2007. 129
- [122] I. T. CHAPMAN, R. SCANNELL, W. A. COOPER, ET AL. **Magnetic Reconnection Triggering Magnetohydrodynamic Instabilities during a Sawtooth Crash in a Tokamak Plasma.** *Physical Review Letters*, **105**(25):255002, December 2010. 129
- [123] P. V. SAVRUKHIN. **Generation of Suprathermal Electrons during Magnetic Reconnection at the Sawtooth Crash and Disruption Instability in the T-10 Tokamak.** *Phys. Rev. Lett.*, **86**:3036–3039, Apr 2001. 129

REFERENCES

- [124] M. YAMADA, F. M. LEVINTON, N. POMPHREY, ET AL. **Investigation of magnetic reconnection during a sawtooth crash in a high-temperature tokamak plasma.** *Physics of Plasmas*, 1:3269–3276, October 1994. 129

List of Figures

1.1	Fusion cross sections for three possible reactions. Note the resonance hump for D-T reaction around 100 keV makes the most promising reaction. [5]	5
1.2	Tokamak design cartoon shows the plasma torus at the center and surrounded by the magnetic field coils (<i>image courtesy of ASDEX Upgrade, Garching</i>).	7
2.1	Comparison between radiation-matter interaction cross-sections of photoelectric (green), Compton scattering (blue), and pair production (red) respectively [66].	27
2.2	The Silicon Drift Detector (SDD) manufactured by MPG-HLL in collaboration with PNSensor GmbH.	29
2.3	Schematic of the Silicon Drift Detector. It is a thin silicon wafer of area 30 mm ² and thickness of 0.5 mm. The green rings create a negative voltage gradient, forcing the free electrons to drift towards the center (<i>image courtesy of B. Huber, IPP, Garching</i>).	30
2.4	Two examples of the reset diode output signal, showing a continuous ramp-up. For every photon event a sudden voltage step appears on top of the ramp-up signal. The reset occurs as soon as the threshold is reached.	31
2.5	The preamplifier circuit board, sitting close to the SDD.	32
2.6	Different blocks involved in the X-ray spectroscopy, plus the schematic diagram of the signal processing electronic stages [80]. Four main block are, (i) Detector itself, (2) Preamplifier, (3) Shaper, and (4) MCA.	33

LIST OF FIGURES

2.7	(a) A zoomed in oscilloscope trace during the reset (time step = $2\mu s$). The reset diode signal is shown in yellow, the shaped signal in green, and the gate signal in violet. (b) The shaper (i.e., integro-differentiator) output signal is shown in gray and the base line in green (time step = $5\mu s$). The gaussian-like signals (in gray) are obtained from the unshaped step-like signals.	34
2.8	The scintillator shown in yellow color is kept on top of the SDD (in gray), with a silicon pad in between them.	41
2.9	The gaussian-like optical emission spectrum (blue curve) of CsI(Tl) matches very well with the SDD quantum efficiency (red curve) for the optical light [85].	43
2.10	The CsI(Tl) shows maximum light yield around room temperature. [88]	45
3.1	The schematic of the steel vessel containing the detector. The detector (yellow) looks vertically downward towards the plasma. The flange at the bottom is mounted on the (tokamak) plasma vessel through a shutter in between. The red cylinder at the right is the copper container to shield the preamplifier electronics mounted inside it. The port on the left is for mounting the vacuum pump. Each port - for the electronics, vacuum, plasma side, and the detector flange, is electrically disconnected with each other with the insertion of ceramic disks and washers.	49
3.2	The schematic cross-section of the detector vessel. On the top, the detector (in yellow) mounted on the small heat carrying copper holder (red), sealed on a steel flange. The optical light-proof detector housing is shown in green. The detector view is controlled by the pinholes and filters to be mounted on the downward side of the housing.	50
3.3	The actual photograph of the detector vessel (rotated 180° sideways as compared to the schematic view in Figure 3.1). On the left side is the preamplifier electronics connected via vacuum feed-through cables.	51
3.4	The old concept of housing the detector. The steel pipe act as a collimator as well as a holder for the pinhole and Be-filter. It was also implemented during the initial experiments on WEGA.	52

3.5	The new housing is completely light proof and more robust. It was implemented during the late 2011 and whole 2012 ASDEX Upgrade campaign.	52
3.6	The etendue represents the effective solid angle the detector is looking through (<i>image courtesy of A. Weller, IPP, Garching</i>).	53
3.7	(a) The vacuum window with 3 allowed lines of sight, (b) the customized filter holders.	54
3.8	The noise proof LEMO adapter found to be responsible for picking up noise in tokamak environment.	57
3.9	The oscilloscope trace showing the noise behavior caused by the LEMO adapter. The preamp (unshaped) signal is shown in yellow and the shaper output signal is shown in green. Both yellow and green curve shows the high frequency noise component sitting on top of the signal.	58
3.10	The X-ray absorption efficiency for different Silicon thicknesses. The SDD is 450 μm thick (shown in green).	59
3.11	Transmission curves for different metallic filters	60
3.12	Combined efficiency curves for the SDD with different Al and Be filters.	60
3.13	Photon energy to pulse height amplitude (channel) relation.	61
3.14	Energy resolution of SDD. The two X-ray lines emitted by Fe-55, Mn- K_{α} and Mn- K_{β} , separated by just 0.5 keV are nicely resolved.	63
3.15	The scintillator holder cap. The steel part holds the scintillator crystal. The outer ceramic part holds both the SDD and the steel cap together rigidly.	64
3.16	The channel-energy linear relation for the HXR-PHA setup.	66
3.17	The line width-energy relation for the HXR-PHA setup.	67
3.18	The offset of the shaper was set such that the 0 keV energy (0 volt amplitude) would appear at a positive channel value of the MCA. (a) 0 volt corresponds to positive channel, (b) 0 volt corresponds to negative channel.	68
3.19	The WEGA stellarator type machine for experimental testing purposes, is located in IPP Greifswald.	69
3.20	The SXR detector vessel (yellow color) mounted on one of the ports on WEGA, with the line of sight intersecting the plasma center.	71

LIST OF FIGURES

3.21	(a) Modified design of the detector vessel, shows the 23 cm long collimator with a 5 mm wide pinhole in the end. (b) Detector vessel installed on the horizontal plane of the WEGA stellarator.	72
3.22	The HXR detector (marked by yellow box) placed facing the WEGA plasma vessel. The direction of the plasma vessel is marked by the red curve.	73
3.23	The cartoon of the experimental assembly at PIGE/PIXE facility at IPP. The HXR detector, mounted on one of the ports is directly receiving the X-ray emission.	74
3.24	The SXR detector installed on port 14Eo at ASDEX Upgrade.	76
3.25	The cross-section of the port 16Bo at ASDEX Upgrade, the red line shows the line of sight of the HXR detector.	77
3.26	The HXR detector vessel is properly shielded against the neutrons and stray γ -rays in the ASDEX hall, by the lead bricks (inner-wall) and paraffin wax bricks (outer-wall).	78
3.27	The HXR setup installed at ASDEX Upgrade hall on 16Bo port. Downward is the direction of plasma. The white bricks cover the HXR detector vessel completely.	79
3.28	The line of sight seen from inside of the tokamak vessel. It was noted that some metallic structure obscures the right part of the circular port. But since our line of sight lies in the left upper half part of the port (yellow box), it is least affected.	80
3.29	The cartoon of the three-detector setup, combining all the SX, HX and neutron effect monitoring in a single diagnostics.	81
3.30	The blocks for the HXR spectral analysis forward modeling technique.	82
3.31	The plasma emissivity is estimated over the equilibrium flux surfaces shown in red. The HXR line of sight is shown in black.	83
3.32	The chord brightness estimated using code IONEQ.	84
3.33	The chord brightness estimated using module genModel.	85
4.1	Geant4 simulation visualization	89
4.2	The photon energy is absorbed dominantly by photo-absorption process at lower energies, whereas at higher energies the dominant process is Compton scattering. The low energy cut off is due to Al-filter absorption.	90

4.3	Different rows from the response matrix function are plotted to visualize the matrix.	92
4.4	The uncalibrated spectra of the four different targets chosen.	93
4.5	The channel-energy relation obtained from the line emission from photon beam induced reactions and radioactive sources.	95
4.6	The width-energy relation obtained from the line emission from photon beam induced reactions and radioactive sources.	96
4.7	The simulated total response curve (red) for the 662 keV (Cs-137) line compared with the measured spectrum (solid blue dots).	97
4.8	It was estimated that the steel cap holding the scintillator is causing some fraction of the Compton scattered photons to enter the detector volume. The effect of steel cap and the β -particle is included in the simulations (red curve).	98
4.9	The Cs-137 (red) and the cosmic background (green) spectrum, both accumulated over 4-5 days period.	99
5.1	Shot #27456. Time trace of 100 seconds, with the shot executed between 10-18 sec. The appearance of photon-events (red dots) at different channels (or energy) has no correlation with the shot time (10-18 sec), showing the total suppression of the noise in the detector assembly.	103
5.2	Typical spectral recording of the background radioactivity at two time intervals (blue and green curve) during the 2011-campaign. The noise usually appears in two forms, noise in the lower channels, and a spike due to radio interference.	104
5.3	The γ -rays produce narrow pulses distinctly different than the neutrons (broad pulses) [100].	105
5.4	A typical neutron induced spectrum (Shot #27453) shows a peak around 150 keV and an extended tail up to 800 keV.	106
5.5	The typical spectrum during high count rate. The frequent reset of the preamplifier brings down the baseline level, causing the reset pulse itself to be counted as a amplitude event, which creates bumpy feature as shown in shaded region. (shot#27465).	107
5.6	The background activity in the torus hall, recorded over night, shows some identified and some unidentified line features.	108
5.7	The prominent line feature at 128 keV, is later used for calibration. . .	109

LIST OF FIGURES

5.8	Shot#27698: The hard X-ray spectral evolution with time. The ECRH power of 2.1 MW is maintained between 1-5 sec, at a constant electron density of $1.6 \times 10^{13} \text{ cm}^{-3}$	112
5.9	Shot#27761: The hard X-ray spectral evolution with time. The ECRH power increases in steps of 0.6 MW every half a second between 1-3 sec, at a constant electron density of $1.3 \times 10^{13} \text{ cm}^{-3}$	113
5.10	Shot #27764. The time traces of the key plasma parameters are shown. The last row shows the time trace of the HXR signal integrated over all photon energies.	118
5.11	Shot #27764. The electron distribution function (equi-momentum contours) as a function of parallel and perpendicular electron momentum, estimated by the Fokker-Planck code. The black curve represents the resonance curve.	119
5.12	Shot #27764. Comparison between the bi-Maxwellian (red) model (with tail temperature of 6 keV) and the Fokker-Planck estimation (green).	120
5.13	Shot #27761. HX spectrum compared with the spectrum calculated by the Fokker-Planck code without parallel electric field.	121
5.14	Shot #27761. HX spectrum compared with the spectrum calculated by the Fokker-Planck code with parallel electric field 0.09 V/m.	122
5.15	Shot #27761. HX spectrum fitted with the bi-Maxwellian model. The tail temperature is varying from 5 keV to 23 keV.	123
5.16	The fraction of non-thermal electrons as a function of $P / \langle n_e \rangle$ (See text for more details).	124
5.17	The non-thermal electron temperature obtained by the bi-Maxwellian model and the peak bulk electron temperature are plotted against $P / \langle n_e \rangle$ (See text for more details).	125
5.18	Extreme hard X-ray emission measured between 100 - 500 keV.	126
5.19	Shot #27766. Time traces of important plasma parameters. The last row shows the total HX count rate.	127
5.20	Shot #27766. Time traces of the X-ray emission decomposed into 0-50 keV and 50-500 keV energy ranges.	128
5.21	Shot #27766. The hard X-ray spectral evolution. The enhanced extreme hard X-ray emission before (magenta and green) and after (blue and red) the plasma heating turned off.	129

5.22 Shot #27695. Time traces of the X-ray emission decomposed into 0-50 keV and 50-500 keV energy ranges.	130
5.23 Shot #27695. The hard X-ray spectral evolution. The enhanced extreme hard X-ray emission during the plasma turning off.	131
5.24 Shot #27761. The saw-tooth like feature observed in the hard X-ray range 30 -100 keV, compared with the soft X-ray signal from the camera J-047 which has the closest line-of-sight to our HX detector.	131
A.1 The multi-channel analyzer PCI card installed in a PC. [81]	138
A.2 The windows based software MCDwin to operate the MCA board.[81]	139
B.1 The Graphical User Interface developed for the hard X-ray data handling, manipulation and visualization.	142
C.1 Shot #27761.	144
C.2 Shot #27698.	144
C.3 Shot #27694.	145
C.4 Shot #27695.	145
C.5 Shot #27683.	146

LIST OF FIGURES

List of Tables

2.1	Comparison of the properties of various scintillators [53; 64].	44
3.1	Pinholes and filters obtained for the specific experiments.	54
3.2	SDD operating voltages	55
3.3	Prominent X-ray lines emitted by two radioactive sources Fe-55 and Am-241 used for the energy calibration of the SDD.	62
3.4	Prominent lines emitted by two radioactive sources Cs-137 and Ba-133 used for the energy calibration of the HXR-PHA [64].	65
3.5	WEGA stellarator machine specifications	70
3.6	The main specifications of ASDEX Upgrade tokamak machine [15]. . .	75
3.7	Plasma parameters	81
4.1	Prominent lines emitted by the selected targets at PIGE. Also the prominent characteristic X-ray lines are listed [94; 95].	94
5.1	List of selected discharges at ASDEX Upgrade, spanning over different ECRH powers and electron densities.	111
C.1	The bi-Maxwellian model analysis of the selected piggy-back experiments, the corresponding model fit parameters are listed below.	146

Lebenslauf

Persönlichen Informationen

Name: Jaydeep Sanjay Belapure

Email: jaydeepsb@gmail.com

Geburtsdatum : 17 Dezemeber 1985

Geschlecht: Männlich

Adresse: Chintamani 503, Prassun Dham, Opp. Birla Hospital, Chinchwad, Pune – 411033, India.

Telefone: +91-020-27308166

Zugehörigkeit

Doktoranden am Max-Planck-Institut für Plasmaphysik, Garching und Technische Universität München, Garching, unter der Aufsicht Prof. G. Hasinger. Seit: Sept. 2009

Graduate Student an :

International Helmholtz Research School on PlasmaPhysics, Garching.

International Max Planck Research School, Garching.

Ausbildung

Nr.	Abschluss	Institut	Noten	Jahr
1	M.Sc. Physik, Hauptfach: Astronomie und Astrophysik	University of Pune, Indien	20	2008
2	B.Sc. Physik	University of Pune, Indien	80%	2006
3	H.S.C. (äquivalent zum Abitur)	Maharashtra Board of Education, Indien	71%	2003
4	S.S.C. (sekundärer Schulabschluss)	Maharashtra Board of Education, Indien	76%	2001

Forschungserfahrung

- Photometric Analysis and Study of Cluster Radio Halo 0116+111 [2007-2008]
- Study of Faraday Rotation Effect and its Application in Astrophysics [May-Jul. 2007]
- FM Radio Meteor Observations from Indian Subcontinent [2005-2007]
- CCD and near Infrared Imaging of Galactic Objects using TIFR 14-Inch and 2-m Hi-malayan Chandra Telescope [May-Jul. 2006]
- Soft Gamma Repeaters And Anomalous X-Ray pulsars [May-Jul. 2005]
- Constructed a 6-Inch optical Newtonian telescope [Apr-Jul. 2000]

Akademische Erfahrung

- Lehre Praktika Masters und Bachelors Studenten an der Technischen Universität München, Garching [2011-2012]
- Lehre Praktika Masters und Doktoranden IUCAA-NCRA, Pune [2008-2009]

Ehrungen und Auszeichnungen

- Best Presentation award (shared) at 5th Interdisciplinary Max-Planck PhDnet Meeting, Bonn, Germany [2010]
- Empfänger der prestigeträchtigen “Young Scientist Encouragement Scheme (KVPY) fellowship” bei Department of Science and Technology, Government of India. [2004-2008]

Konferenz publikationen

- A. Weller, B. Huber, J. Belapure, et. al., X-Ray Pulse Height Analysis on ASDEX Upgrade, Proc. of the 38th EPS Conf. on Plasma Physics, ECA, 2011, Vol. 35G
- T. Stange, H. P. Laqua, J. Belapure et. al., Characterization of a highly energetic electron component of electron Bernstein wave heated plasmas in the WEGA stellarator. Proc. of the 38th EPS Conf. on Plasma Physics, ECA, 2011, Vol. 35G.
- M. Otte, J. Belapure, E. Chlechowicz, et. al., Diagnostic Development for Wendelstein 7-X at the WEGA Stellarator, Proc. of the 37th European Physical Society Conference on Plasma Physics. Contributed Papers, European Physical Society, ECA, 2010, Vol 34A.
- R. Dabhade, V. Savant, J. Belapure, Meteor Shower observations from the Indian Sub-Continent (Visual Photographic and Radio), Proc. of Int. Meteor Conf., Armagh, Northern Ireland, Sept., 2010, pp. 22-24.
- J. Bagchi, J. Jacob, G. Krishna, et. al., A diffuse bubble-like radio-halo source MRC0116+111: imprint of AGN feedback in a low-mass cluster of galaxies, MNRAS, 2009, v399-2, pp. 601
- Velapure S., Alekari P., Belapure J., Forward Meteor Scatter Monitoring System, International conference on SSPCIN, IEEE Bombay Section, 2008.
- Belapure J. et al., FM Radio observations of various meteor showers during 2005-2006 from India, 10th Young Astronomers Meet, 2007, India.
- Belapure J. et al., Radio Observations of Leonid 2005 Meteor Shower, XIV National Space Science Symposium, 2006, India.
- Belapure J. et al., FM Radio Observations of Quadrantids 2006 Meteor Shower from India, 11th National Seminar on Physics and Technology of Sensors, 2006, India.
- Belapure J. et al., Meteor Shower Observations from India by FM Radio Method, National Symposium on Instrumentation (NSI-30), 2006, India.